



POLITECNICO DI TORINO
Repository ISTITUZIONALE

Modelling and Simulation of Silicon Nanowire-Based Electron Devices for Computation and Sensing

Original

Modelling and Simulation of Silicon Nanowire-Based Electron Devices for Computation and Sensing / Antidormi, Aleandro. - (2016).

Availability:

This version is available at: 11583/2643159 since: 2016-05-31T12:29:29Z

Publisher:

Politecnico di Torino

Published

DOI:10.6092/polito/porto/2643159

Terms of use:

openAccess

This article is made available under terms and conditions as specified in the corresponding bibliographic description in the repository

Publisher copyright

(Article begins on next page)

POLITECNICO DI TORINO

SCUOLA DI DOTTORATO

Dottorato in Ingegneria Elettronica e delle Comunicazioni – XXVIII
ciclo

Tesi di Dottorato

Modelling and Simulation of Silicon Nanowire-Based Electron Devices for Computation and Sensing



Aleandro Antidormi

Tutore

prof. Gianluca Piccinini
prof. Mariagrazia Graziano
Dr. Luca Boarino (I.N.Ri.M.)

Direttore del corso di dottorato

prof. Ivo Montrosset

Maggio 2016

Summary

Silicon Nanowires (SiNWs) are considered the fundamental component blocks of future nanoelectronics. Many interesting properties have gained them such a prominent position in the investigation in recent decades. Large surface-to-volume ratio, bio-compatibility, band-gap tuning are among the most appealing features of SiNWs. More importantly, in the ongoing process of dimension miniaturization, SiNWs compatibility with the existing and reliable silicon technology stands as a fundamental advantage. Consequently, the employment of SiNWs spread in several application fields: from computational logic where SiNWs are used to realize transistors, to bio-chemical sensing and nanophotonic applications.

In this thesis work we concentrate our attention in the employment of SiNWs in computational logic and bio-chemical sensing. In particular, we aim at giving a contribution in the modelling and simulation of SiNW-based electron devices. Given the current intense investigation of new devices, the modelling of their electrical behaviour is strongly required. On one side, modelling procedures could give an insight on the physical phenomena of transport in nanometer scale systems where quantum effects are dominant. On the other side, the availability of compact models for actual devices can be of undeniable help in the future design process.

This work is divided into two parts. After a brief introduction on Silicon Nanowires, the main fabrication techniques and their properties, the first part is dedicated to the modelling of Multiple-Independent Gate Transistors, a new generation of devices arisen from the composition of Gate-All-Around Transistors, finFETs and Double-Gate Transistors. Interesting applications resulting from their employment are Vertically-stacked Silicon Nanowire FETs, known to have an ambipolar behaviour, and Silicon Nanowire Arrays. We will present a compact numerical model for composite Multiple-Independent Gate Transistors which allows to compute current and voltages in complex structures. Validation of the model through simulation proves the accuracy and the computational efficiency of the resulting model.

The second part of the thesis work is instead devoted to Silicon Nanowires for bio-chemical sensing. In this respect, major attention is given to Porous Silicon (PS), a non-crystalline material which demonstrated peculiar features apt for sensing. Given its not regular microscopic morphology made of a complex network of

crystalline and non-crystalline regions, PS has large surface-to-volume ratio and a relevant chemical reactivity at room temperature. In this work we start from the fabrication of PS nanowires at Istituto Nazionale di Ricerca Metrologica in Torino (I.N.Ri.M.) to devise two main models for PSNWs which can be used to understand the effects of porosity on electron transport in these structures. The two modelling procedures have different validity regimes and efficiently take into account quantum effects. Their description and results are presented.

The last part of the thesis is devoted to the impact of surface interaction of molecular compounds and dielectric materials on the transport properties of SiNWs. Knowing how molecules interact with silicon atoms and how the conductance of the wire is affected is indeed the core of SiNWs used for bio-chemical sensing. In order to study the phenomena involved, we performed *ab-initio* simulations of silicon surface interacting with SO_2 and NO_2 via the SIESTA package, implementing DFT code. The calculations were performed at Institut de Ciencia De Materials de Barcelona (ICMAB-CSIC) using their computational resources.

The results of this simulation step are then exploited to perform simulation of systems made of an enormous quantity of atoms. Due to their large dimensions, atomistic simulations are not affordable and other approaches are necessary. Consequently, calculations with physics-based softwares on a larger spatial scale were adopted. The description of the obtained results occupies the last part of the work together with the discussion of the main theoretical insight gained with the conducted study.

Table of contents

Summary	I
1 Introduction	1
1.1 Fabrication Techniques for Silicon Nanowires	2
1.2 Devices Based on Silicon Nanowires	5
1.3 Silicon Nanowire Based Solar Cells	9
1.4 Silicon Nanowire Based Sensors	10
1.5 Electronic Properties of SiNWs	10
1.5.1 Passivated Nanowires	11
1.5.2 Quantum confinement	11
I SiNWs for Computation	14
2 Multi-Gate Transistors: an Introduction	16
2.1 Short-Channel Effects	16
2.2 Multi-Gate Transistors	18
2.2.1 Double-Gate and FinFET	18
2.2.2 Gate-All-Around transistors (GAA)	19
3 The Model	21
3.1 Introduction	21
3.2 Structure definition and Objectives	21
3.3 The core of the Multi-Gate Device Model	23
3.3.1 Generalities	23
3.3.2 Discussion About Convergence	24
3.3.3 Closed Form Expressions Derivation	25
3.3.4 Quantum mechanical (QME) and Short-Channel effects (SCE)	28
3.4 Generalizations of the method to more complex structures	29
3.4.1 Arbitrary Number of Gates	29
3.4.2 Gateless Sections	31

3.4.3	Doped Channel Sections	32
3.4.4	Sections with Different Geometry	33
4	Verification and Results	34
4.1	Methodology	34
4.2	Two-Section Structure	35
4.3	Three-Section Structure	36
4.4	Three-Section Structure with Fixed Gate Voltages at Extremes . . .	39
4.5	Gateless Section Structure	40
4.6	Computation Times	40
4.7	Discussions	44
4.8	Conclusion	44
II	SiNWs for Sensing	46
5	Porous Silicon	49
5.1	Introduction	49
5.2	Morphology	49
5.3	Fabrication	50
5.3.1	Introduction	51
5.3.2	The Overall Etching Process	52
6	Fabrication of PSNWs	55
6.0.1	Metal and deposition technique tests	55
6.0.2	Gold (Au) - thermal and e-beam evaporator	57
6.1	Ordered sample	59
6.1.1	Solution	61
6.2	TEM Analysis	62
7	PS model	64
7.1	PS-NW model	66
7.1.1	Structural model	66
7.1.2	Transport Model	68
7.1.3	Numerical Parameters	69
7.2	Simulation Results	69
7.3	Conclusions	72
8	Going smaller	74
8.1	Theoretical Background on Transport	75
8.1.1	Quantum Transport	75
8.2	Mesoscopic electron transport	77

8.3	Linear Response Theory	77
8.4	Ballistic Transport	78
8.4.1	Landauer-Buttiker Formalism	79
8.4.2	Scattering matrix and Transfer Matrix	80
8.5	Conclusions	81
9	A New Model for PSNWs	83
9.1	Introduction	83
9.2	The System	84
9.3	Digression	84
9.4	The Model	85
9.5	Transmission coefficient	88
9.5.1	Nanocrystal	88
9.5.2	Nanowire	90
9.6	Self-consistent field	91
10	Model Validation and Results	92
10.1	Validation	92
10.2	Results and Discussion	93
10.2.1	Single Nanocrystal	93
10.2.2	Sequence of two Nanocrystals	95
10.2.3	Nanocrystal + Nanowire + Nanocrystal	95
10.3	Further Analysis	98
10.3.1	Porosity	99
10.3.2	Number of Blocks	101
10.3.3	Geometrical Parameters	102
10.4	Conclusion	105
11	Ab-initio simulations	109
11.1	Introduction	109
11.2	Methods	110
11.3	Results	111
11.3.1	Hydrogen-passivated Surface	111
11.3.2	Non-passivated surface	113
11.3.3	H-passivated surface with SO ₂ molecules	113
11.3.4	H-passivated surface with NO ₂ molecules	115
11.4	Conclusions	117
12	Analysis of Surface Interaction	119
12.1	Methods	120
12.2	Results	121

12.3	Conclusions	133
13	Conclusions	136
A	Density Functional Theory	137
A.1	A brief DFT survey	137
A.1.1	The Hohenberg-Kohn theorem	137
A.1.2	The Kohn-Sham equations	140
A.1.3	The Form of E_{xc}	143
B	List of Publications	147
	Bibliography	148

Chapter 1

Introduction

Silicon nanowires are quasi one-dimensional (1D) structures with a diameter smaller than 100 nm with a consequently large surface to volume ratio. This property can be exploited in many electronic devices [1]: with a gate wrapped around the nanowire, it is possible to optimally control the charge density in the nanowire potential via the gate potential. This has paved the way towards the adoption of silicon nanowires in computational logic. When it comes to sensing devices, the small volume will allow effectively controlling the potential of the nanowire by even a very small input signal, making the approach very sensitive specifically for chemical sensing and bio-sensing [2, 3]. But also the field of energy generation and storage can benefit from the quasi 1D structure. In the solar cells the nanowires allow to more efficiently collect the incoming solar radiation [51] whereby in Li-ion batteries the structure allows for volume expansion [5].

A large number of techniques exist to fabricate silicon nanowires. These can be classified into bottom-up and top-down fabrication techniques. In top-down fabrication, lithography is used to define the fabricated structure that is then transferred from the photo-resist to the substrate by etching or a similar way of structuring the already available material. In the bottom-up approach, the material is added to the substrate in a self-organized way.

This chapter will review the current status of silicon nanowire technology. In the first part the silicon nanowire fabrication techniques will be summarized and there advantages and disadvantages will be discussed. The second part will then review the very important field of silicon nanowire based electron devices. Devices that are targeted to extend the current semiconductor roadmap are discussed together with approaches that are intended to add new functionality to semiconductor devices. The section on silicon nanowire based sensors will then focus on devices that can take full advantage of the know-how from integrated circuit manufacturing and illustrate further concepts. Finally, the possibilities for enhancing solar cells and Li-ion batteries will be discussed. The last part of this introduction is focused

on the general properties of silicon nanowires with particular attention on quantum confinement potential and nanowire passivation.

1.1 Fabrication Techniques for Silicon Nanowires

Fabrication techniques of Silicon Nanowires are generally classified in top-down and bottom-up techniques. Traditionally semiconductor technology is driven by top-down fabrication using photo lithography, an approach which has successfully allowed to scale down device dimensions up to the 10 nm range [6]. In contrast, bottom-up techniques have the potential to produce very complex structures without defining their details by a mask [7]. Both fabrication methodologies are possible for silicon nanowires, each with its own advantages and drawbacks. In particular, in the top-down fabrication, an ideally simple path from present planar structures to FinFETs and nanowire-based devices can be envisioned. However, the etching of the nanowire from the bulk silicon gives non-perfect geometry and requires advanced lithography. On the other hand, an excellent crystal quality and small diameter can be obtained through bottom-up processes. Nevertheless, the realization of complex structures like integrated circuits is still too far to be true. Therefore, combinations of both paradigms are considered.

The most exploited nanowire synthesis method is the vapor liquid solid (VLS) growth mechanism. In the VLS technique the growth results from a phase changes that are mediated through a catalyst particle. That means that the material to be grown, in this case silicon, is delivered in the gas phase, either molecularly or in the form of a gas compound that is introduced into the growth chamber. Figure 1.1 shows a schematic sketch illustrating the widely adopted VLS growth.

In the case of Si, molecular Si precursors can be evaporated either by Si effusion cells, or pulsed vapor deposition. Silicon gas precursors include mono-silane (SiH_4), trichlorosilane (SiHCl_3) or higher order silanes. The catalyst particle acts as a collector of silicon. When employing gas precursors, the catalytic nature leads to lowering of the dissociation energies of the gas. Consequently, a high concentration of silicon atoms is found at the catalyst particle surface, leading to diffusion into the cluster. An important implication of the VLS mechanism is that the size of the Au cluster defines the diameter of the nanowire without the need of further lithographic means. In addition, the catalyst position on the substrate dictates the nanowire placement.

For top-down fabrication of nanowires well-established technologies from silicon VLSI circuit technology can be applied. To form horizontal nanowires that are electrically isolated from the substrate, two approaches are commonly used. In the

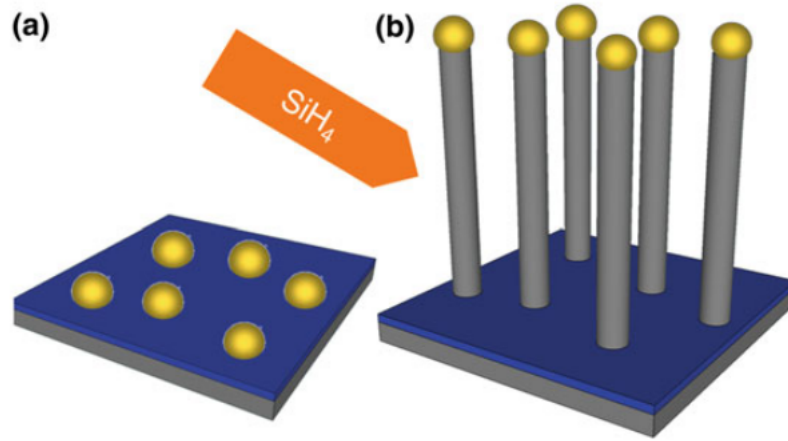


Figure 1.1. Schematic view of VLS growth of silicon nanowires. a) Gold particles formed on the growth substrate. b) VLS growth using silane as silicon precursor.

simplest one, a SOI substrate is used and the nanowire is etched into the thin active silicon layer using an anisotropic etching process [8]. In the other approach bulk silicon and a deep reactive ion etch (DRIE) process are used together to structure a stack of nanowires [9]. Figure 1.2 shows both approaches schematically. The latter approach is such that the footprint is small and there will be several parallel nanowires to carry the current in a device using nanowires.

According to the procedures just described, the bottom-up fabrication will lead to a vertical arrangement of nanowires and the top-down arrangement will lead to a horizontal arrangement of nanowires. If horizontal nanowires have to be fabricated by the bottom-up technique, the alignment is very critical. In general the nanowires will be dispersed on the receiving substrate. For basic research, it can be sufficient to simply use a direct writing lithography technique to further build the required device. However, for mass fabrication an alignment of the structures will be required. Although some promising approaches have been shown, so far no technique for reliable mass fabrication is available. Therefore, the top-down approach seems to be the approach of choice for the mass fabrication of horizontal silicon wires using a silicon substrate. Also vertical wires can be achieved by using lithography and a subsequent anisotropic etching [10, 11], this technique has the drawback that very high aspect ratios have to be etched and dimensional control is very critical. On the other hand, the bottom-up approach naturally yields vertical devices [12] and the precise positioning can be controlled by a defined positioning of the catalyst particles.

Besides the fabrication of the nanowires themselves, a few critical processing steps have to be available to fabricate electron devices. The most important are: the

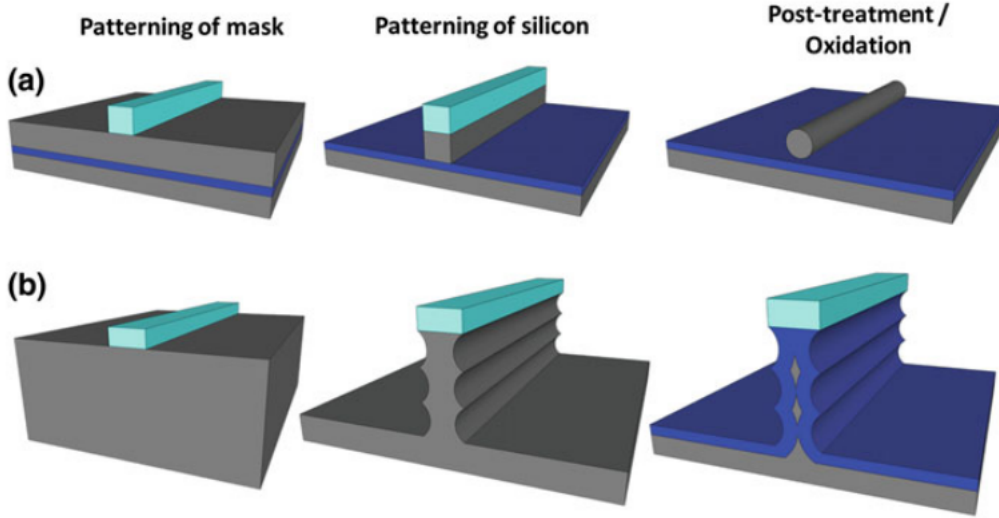


Figure 1.2. Horizontal silicon nanowires fabricated by top down fabrication. a) Starting with SOI substrate and etching using anisotropic reactive ion etching. b) Starting with bulk substrate and etching with deep reactive ion etching and subsequent oxidation. From [1].

previous mentioned alignment of nanowires in case that bottom-up grown nanowires will be used, the doping of nanowires, the formation of contacts to the nanowires and finally the formation of a well-defined dielectric shell.

For alignment, a number of techniques have been proposed [13, 152]. Dielectrophoresis has been used successfully for wire alignment [15, 16]. Microfluidic alignment [81], contact printing [18, 19] and Langmuir-Blodgett techniques can also be used [20, 21]. However, all methods still face issues with either wire density for high integration or rather low yield of the desired structures or both. Therefore, for high device densities comparable or beyond the state of the art, CMOS top-down approach is still the more preferred choice to define the nanowire location. However, for applications on flexible substrates or in sensors with parallel nanowires [19] some of the available procedures like contact printing could already be sufficient.

Doping of nanowire structures is also a critical issue. In modern CMOS fabrication, most doping steps are done using ion implantation. This, however, is not straightforward due to the geometry of silicon nanowires. Specifically the defined doping in a vertical arrangement is problematic. In bottom-up grown structures different options exist to dope the wires during growth. In case of catalyst-enabled growth, it is an intriguing idea to use the catalyst itself as dopant for the nanowire. Nevertheless, especially p-doping by using aluminum catalysts has recently shown very promising results [22].

To contact the nanowires a metal to nanowire contact is required. This can be the limiting factor for the device construction [23]. Using a metal silicide is very favorable method [161, 25].

Finally in order to achieve reproducible device properties it is important to passivate the nanowire surface and form a good gate insulator for a field effect transistor (FET). The natural oxide of silicon is one of the main reasons why silicon has considerably outperformed every other semiconductor for high density and high performance circuits and systems [26]. Therefore, it is natural to also use silicon dioxide in silicon nanowire devices and indeed it can deliver excellent properties [27]. However, also here the higher k value of materials like hafnium dioxide (HfO_2), which is established in CMOS technologies today, is of benefit [28].

1.2 Devices Based on Silicon Nanowires

Silicon demonstrates unique properties in structures with a 1D shape. Quantum confinement of electrons and holes is predicted to be substantial only at aggressive diameters below of 3 nm [29]. Note that this is in contrast to III-V semiconductors, where confinement is visible already at larger diameters. Thus, the behavior of Si nanowires is considered as quasi 1D. The band structure is strongly modified for Si nanowires with diameters below 10 nm. The band gap increases for smaller diameters and a direct band gap can be obtained for sufficiently small diameters [29, 30]. Thanks to these effects and properties, silicon nanowires with very small dimensions can be used in devices in many different ways. One example is represented by field effect devices, where a gate electrode is wrapped around the nanowire, hence providing an optimum geometric gate coupling. In addition to this, if the silicon thickness is small enough to allow a full depletion at low voltages the best scaling behavior of the device can be achieved [31]. Moreover, the density of states can be exploited allowing to design nanowire field effect devices to operate either in a classical gate capacitance limited mode or the quantum capacitance limit. In the latter the channel charge remains constant when scaling down the gate oxide thickness leading to an improved power of delay product [32].

Logic devices benefit largely from the excellent gate control when implemented in a nanowire structure. However, for viable applications additional requirements have to be fulfilled. Thus, alternative concepts to the conventional MOSFET have emerged. The most important of these are illustrated in Fig. 1.3. With ever decreasing device dimensions doping becomes more and more problematic. On the one side the doping profiles need to be controlled much more precisely. However, due to diffusion during dopant activation an ideal steplike profile is hard to achieve even if very short millisecond annealing is used. Second, the number of dopants

in the active channel region decreases. Since the relative variability will scale with $N \approx 1/2$ [33] doping fluctuations will make the control of the threshold voltage nearly impossible [34]. In addition to these difficulties, it has been proven by calculations and experiments, that for certain nanowire geometries, the ionization energies of dopants are higher than in bulk [35, 36]. For nanowires without a surrounding gate dopant deactivation takes place, i.e. to achieve the same doping effect, a higher dopant concentration is needed, especially for thin nanowire diameters.

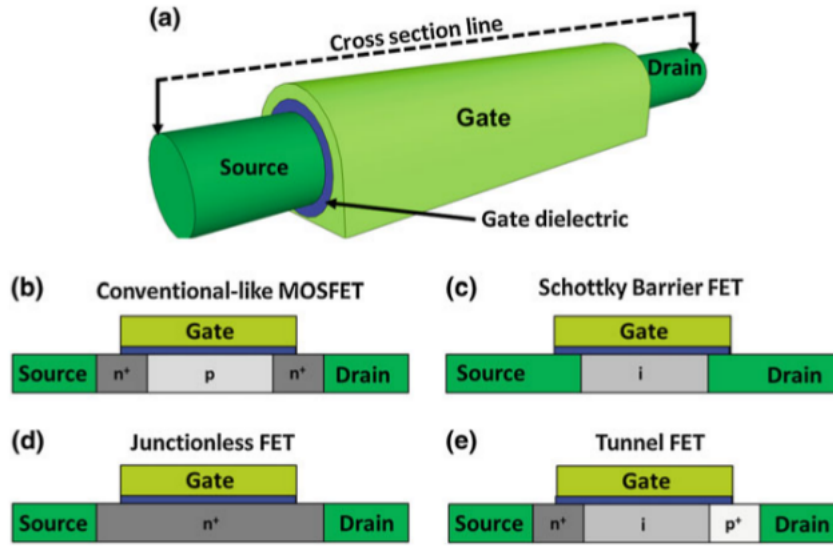


Figure 1.3. Different options for electron devices using silicon nanowires. The top drawing a) shows a generic 3-D view of a silicon nanowire device with metallic source/drain regions and the surrounding gate. The cross sections b-e illustrate different device concepts: b) Conventional nanowire MOSFET, c) Schottky Barrier FET, d) Junctionless FET and e) Tunnel FET. From [1].

Both the Schottky barrier field effect transistor (SBFET) [37, 38] and the junctionless transistor [39] can help to control these issues. In the SBFET, the highly doped source and drain regions are replaced by metal-semiconductor Schottky junctions, and the silicon body of the transistor can be undoped. The device benefits from the nanowire geometry since very sharp and defined silicide junctions can be used [40]. For charge transport this implies that two energy barriers are introduced along the current path. The thickness of these barriers is efficiently controlled by the gate due to the electric field enhancement at the tip-like metal electrode geometry. The on-state for sufficiently small gate lengths is given by tunneling through the Schottky barriers, while the off-state is controlled by thermionic emission over a high and thick energy barrier. The undoped channel eliminates issues of threshold

voltage control caused by doping fluctuations. In the junctionless device, the whole nanowire is highly doped. Thus, the formation of a very sharp junction in the scaled device is elegantly avoided.

One of the biggest challenges for further device scaling is the inability to scale the threshold voltage due to the thermal limit of 60 mV/dec for the subthreshold slope. Since lowering the supply voltage is of very high importance both for physical device scaling and reduction of the power consumption it is one of the most pressing issues to find ways in order to reduce the subthreshold slope below this value. One promising option is the tunneling field effect transistor (TFET) [41].

The TFET would also greatly benefit from the nanowire geometry. From an electrostatic point of view, the nanowire geometry with a surrounding gate stack facilitates sufficient band bending for band-to-band tunneling. Furthermore, for sufficiently small diameters the energy distribution of density of states exhibits van Hove singularities. Hence, a comparatively high amount of states are available for band to band tunneling at the conduction and valence band edges. As the energetic window for band to band tunneling cuts the high energy tail of the Fermi distribution function, the tunnel FET principally enables a switching behaviour with a reduced subthreshold swing below 60 mV/dec at room temperature. However, like in Schottky FETs, the tunneling transmissibility through the energy barriers limits the on-current through the device. Therefore, from today's point of view TFET are alternatives for low operating power. Recently, encouraging results have been shown demonstrating a performance that is coming close to the requirements for an actual implementation [42, 43]. In a recent publication [44] the combination of a junctionless transistor and a tunnel FET is described, combining features of both device types.

All those devices target an improvement of the classical CMOS technology, exploiting the enhanced electrostatic control within the nanowire geometry. However, silicon nanowires also enable a new type of transistor, in which the device polarity can be controlled by an electrical signal [45]. Therefore the same physical device can be used at different times as p-channel or n-channel transistor. These so called reconfigurable field effect transistors (RFET) or Multiple-Independent Gate transistors hold the potential to lower the transistor count needed for the same functionality and be used in complex array configurations. The different concepts to build such a device are illustrated in Fig. 1.4.

In the electrostatic doping approach [46], shown in Fig. 1.4-a, the back-gate is used as program gate to select electron or hole transport. The program gate bends the silicon bands at both junctions simultaneously. Negative program gate voltages increase the barrier height at the conduction band and thereby block electrons. At the same time the energy barrier height for holes is the natural Schottky barrier height. Its thickness is diminished and thermal assisted tunneling of holes can take

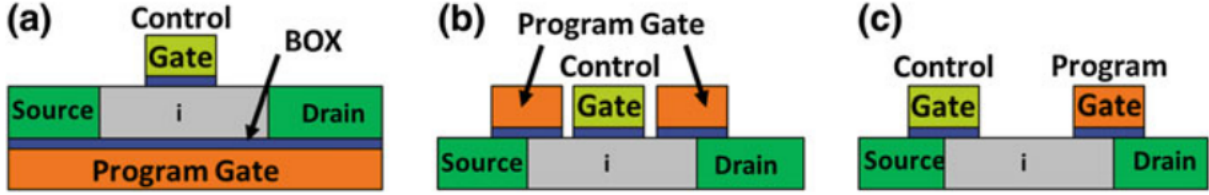


Figure 1.4. Schematic cross sections of the different concepts for reconfigurable silicon nanowire devices. In the electrostatic doping device (a) the back gate is used to adjust the barrier heights and a top gate controls the current trough the device. The simultaneous control of both Schottky barriers (b) can also be accomplished by using top gates and an additional control gate in the middle then controls the carrier flow. In the RFET (c) approach the program gate above the drain junction and the control gate above the source junction control the polarity and the current flow respectively

place. Correspondingly, positive program gate voltages block holes and enable electron injection. Once the program gate is set to a specific polarity, the top gate is then used to adjust the amount of current flowing from source to drain. The use of buried and common gates, as employed in Fig. 1.4-a, implies having a comparatively weak gate coupling to the active region and therefore a high gate operation voltage. Moreover, the independent operation of neighboring devices, as required in integrated circuitry, can only be solved by substantial technological means leading to a limited scalability of this structure.

In the approach sketched in Fig. 1.4-b, the two outer top gates are kept at the same potential and provide a similar function as the back gate in Fig. 1.4-a. Thus, this concept allows the individual control of different devices in one chip. In the top-down realization a surrounding gate architecture is provided for both control and program gates [47]. Moreover, in a single device numerous nanowire channels are vertically stacked in parallel to enhance the drive current. The three gates can also be connected independently to allow the control of the threshold voltage of the device.

The RFET device shown in Fig. 1.4-c uses two independent top gates each overlapping one of the Schottky junctions. One of them is used to control the polarity. The other is used to control the amount of current flowing through the device. In contrast to the other polarity control concepts and to conventional CMOS, the main part of the active region is ungated.

Recently significant progress has been made both in understanding and designing the appropriate transport mechanisms and showing the benefit of building circuits

out of the reconfigurable devices [48]. If CMOS circuits are to be constructed from such devices, it has to be considered, that the geometry cannot be adjusted according to an unbalanced current output of p-channel and n- channel devices since the same device has to be usable in both configurations. Therefore, the output has to be symmetrical for both carrier types. Using stress engineering this could be demonstrated in the approach with two top gates illustrated in Fig. 1.4-c [49].

1.3 Silicon Nanowire Based Solar Cells

Energy generation from renewable sources and storage of electrical energy can benefit from silicon nanowires as well, as they have the potential to increase the optical absorption and collection efficiency in solar cells [50, 51]. Single nanowire solar cells can be used to study the parameters that influence the performance of nanowire based photovoltaics [51, 52]. Additionally, they allow a simple integration with nanowire based electronics and sensors [51]. For general purpose solar cells, however, the single wire elements have to be arranged in large arrays [53]. The low cost bottom-up growth, which is compatible with different types of substrates, is the fabrication method of choice for such devices. In order to accomplish all the requirements, a coaxial structure is the best one. First of all, the possibility to fabricate radial pn- junctions has shown promising results. Figure 1.5 shows a schematic view of a silicon nanowire array based solar cell using this concept. Moreover, the flexibility of combining different materials in the nanowire arrangement is utilized as can be seen, for example, in [54].

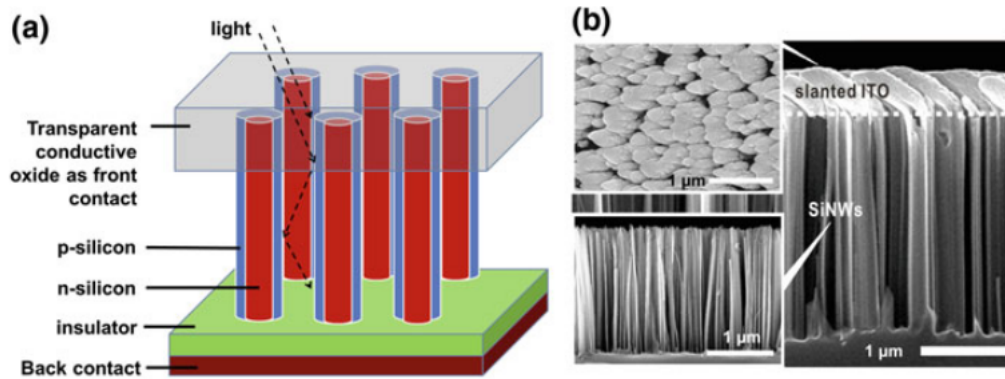


Figure 1.5. a Schematic view of a silicon nanowire based solar cell with a radial pn-junction. b SEM micrographs from top view and cross section of the solar cell, as well as from the silicon nanowire array. From [55]

1.4 Silicon Nanowire Based Sensors

A sensor transforms a physical or chemical signal of the environment into an electrical signal [56]. Normally, the sensor device can be split into the active sensing part, which translates the input signal into an intermediate signal and the transducer that translates the intermediate signal into the final electrical signal. In many cases, the two parts are closely linked. The quasi 1-D properties of nanowires can be utilized in transducers and in some cases also for the active sensing part of the chain. Especially chemical and biochemical sensor research has intensively utilized silicon nanowires in the last decade [57]. The research on chemical and biochemical sensors is again strongly driven by the exploitation of the extremely high surface to volume ratio combined with excellent mechanical stability. Having in mind that excellent field effect transistor devices can be constructed, it is a natural consequence to apply the idea which Bergveld first explored in 1971 [58] in the ion sensitive field effect transistor (ISFET) to measure variations in the impedance. The transfer of these ideas to nanowire-based devices was therefore already demonstrated more than a decade ago [161]. For biochemical sensors the diameter of the nanowires can be as small as the species to be detected. This enables a very high sensitivity of the sensor device even if parallel nanowires are used in order to increase the device current, since the current percolation paths are effectively blocked already by a single molecule per nanowire. Looking at a single nanowire this situation paves the way to single molecule detection as demonstrated in [60].

It is important to point out that nanowire based devices have their specific advantage when it comes to a very sensitive detection in small volumes and therefore can enable biosensors that are not possible using a planar transducer.

The small size, flexible fabrication and mechanical properties of nanowires can also be utilized to extend the functionality of biological sensors. Nanoscale FET devices can be integrated at the tip of a kinked silicon nanowire, as it is reported in [61]. Here, the nanoscale connections are made by the arms of the kinked nanostructure.

1.5 Electronic Properties of SiNWs

Silicon nanowires are, due to their small dimensions, greatly sensitive to the structure details, interface properties which determine the electron properties of the devices. Analogously, in the limit of very large diameter, their properties converge to those of bulk Si. Pristine nanowires turned out to have a limited relevance, at least to date, because experimentally grown SiNWs are always passivated. However, the study of bare unpassivated wires is still interesting for two reasons: a) it leads to the conclusion that passivation is essential to obtain nanowires with predictable and easy to control electrical properties and b) it sheds a light on some atomic-scale

mechanisms of fundamental interest.

An interesting example in this sense is the electronic structure of [100] SiNWs with [100] facets. While other facets, like the [111] facets, have an electronic structure similar to the corresponding infinite surface [100] facets can be very different. In the Si [100] surface each surface atom has two dangling bonds. Wires dominated by such facets have been reported to be metallic. Rurali and Lorente [62], moreover, showed that thin 100 SiNWs sustain two different reconstructions of the [100] facet that turn the wire metallic or semimetallic, in agreement with Ismail-Beigi and Arias [63]. The metallicity rapidly vanishes as the diameter is increased and the semiconducting electronic structure of the Si [100] surface is reobtained.

Such wires are not desirable for electronics application: on the one hand, one wants to work with semiconducting systems; on the other hand, although some application can be found for metallic SiNWs, e.g., interconnects, the metallicity should be much more robust, so that it does not depend on the atomic-scale structure of the wire.

A comprehensive study of the surface reconstruction and electronic structure of pristine [110] wires has been carried out by Singh et al. [64]. The cross section chosen for these wires is such that they have [100] and [110] facets. These [110] SiNWs turned out to be indirect band-gap semiconductors, with the states of the valence band top and the states of the conduction band bottom originating at different facets. However, small variations of the atomic-scale structure or of the cross section can result in major changes in the electronic structure.

1.5.1 Passivated Nanowires

As mentioned surface passivation is required to obtain ultrathin nanowires that are semiconducting and have a predictable and controllable band gap. Notwithstanding, the electronic structure of the nanowires still depends on the growth orientation, on the cross-section shape, and on the diameter. The band gap is strongly anisotropic [65] and, for wires of comparable diameters, it follows the ordering

$$E_g^{100} > E_g^{111} > E_g^{110} \quad (1.1)$$

with the orientation effect still sizeable up to 3 nm in diameter; see Fig. 1.6.

1.5.2 Quantum confinement

One of the most intriguing physical effect that arise in confined systems like SiNWs is the so-called quantum confinement. Such a regime is conveniently described through the particle-in-a-box model system in most quantum mechanics text books (Bransden and Joachain, 2000). The simplified situation considered is an infinite potential

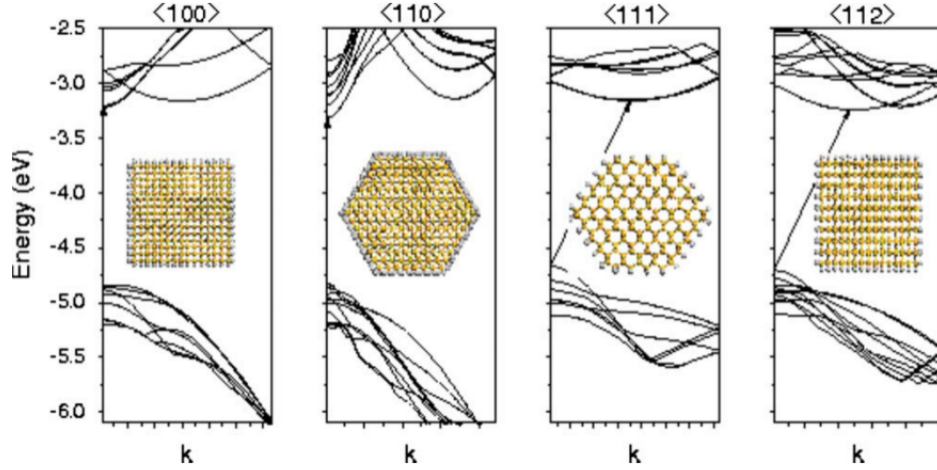


Figure 1.6. Band structures of [100],[110], [111] and [112] SiNWs with a diameter of $3nm$ cross sections in the insets. The arrows indicate the fundamental band gap which is direct for [100] and [110] SiNWs and indirect for [111] and [112] SiNWs. From Ng et al., 2007.

well where the motion of the particles is restricted to be in the direction of the confinement. As the motion of the particles is restricted, their kinetic energy increases and it is readily shown that the eigenstate energies are given by

$$E_n = \frac{\hbar^2 n^2 \pi^2}{2m^* d^2} \quad (1.2)$$

where m^* is the effective mass and d is the width of the potential well. According to the equation, not only the energy levels, but also the spacing between them increases as the confinement becomes more pronounced, i.e., the smaller d is. Quantum confinement has a critical impact on semiconductors because it affects directly their most important electronic property: the energy bandgap. Semiconducting nanowires provide a good approximation of the model situation described above. Clearly, the potential well is not infinitely deep and realistic wire cross sections are difficult to describe analytically, thus there is a need for a detailed electronic structure modelling.

The first experimental proofs of quantum confinement in nanostructured Si were reported in the pioneering works of Canham [66] and Lehmann and Gosele [67], where a simple electrochemical etching process was used to create crystalline Si nanostructures with visible luminescence at room temperature. As TEM images revealed later (Cullis and Canham, 1991), the etched structures consisted of rather disordered bundles of nanowires. Buda et al. [68] performed DFT calculations of the band-gap upshifts in perfect H-terminated SiNWs as a function of wire thickness.

These works showed that the fundamental gap is direct at the Γ point. This makes by itself the probability of radiative recombination higher than in bulk Si, since no phonon is required in the electron-hole recombination process. Unfortunately, as it is well known, standard local and semilocal implementations of DFT fail to account quantitatively for the band-gap of semiconductors and one must resort to self-energy corrections to the Kohn-Sham gap to obtain good agreement with the experimental values. Yet, the trends are expected to be qualitatively correct: Williamson et al., reported band-gap upshift of up to 2 eV for wires of 12 Å diameter. They also showed that a generalization of eq. 1.2 gives a good description of the quantum confinement for wires wider than 23 Å, whereas thinner wires show significant deviations from this idealized EMT picture. In such a range Buda et al. [68] showed that with the more realistic DFT potential the band gap scales as the inverse of the diameter d , rather than $1/d^2$ as predicted by particle-in-a-box arguments where infinitely hard walls are assumed.

Part I

SiNWs for Computation

SINWs for COMPUTATION

**Multiple Independent-Gate
Transistors:**
Modelling & Simulation

SINWs for SENSING

Porous Silicon NWs:
Fabrication & Modelling

Surface Interaction:
Ab-initio & Macroscopic
simulations

Chapter 2

Multi-Gate Transistors: an Introduction

Since the 1990's the cooperation among semiconductor companies and academia led to the elaboration of an instrument to predict more precisely the future of the industry. They called it International Technology Roadmap for Semiconductors (ITRS) organization. It issues a report that serves as a benchmark for the semiconductor industry, describing the type of technology, design tools, equipment and metrology tools that need to be developed to keep pace with Moore's law.

The most important technology of semiconductor industry has been silicon CMOS, and the building block of CMOS is the MOS transistor or MOSFET. With the aim of fulfilling the rhythm of Moore's law, the linear dimensions of transistors have reduced by half every three years. The sub-micron dimension barrier was overcome in the early 1980's, and currently semiconductor manufacturers are producing transistors with a 20nm gate length. The first integrated circuit transistors were fabricated on "bulk" silicon wafers, but at the end of the 1990's, a significant improvement was obtained by switching to a new type of substrate called SOI (Silicon-On-Insulator) in which transistors are made in a thin silicon layer deposited on top of a silicon dioxide layer. Both circuit speed and power consumption improved with SOI technology due to the fact that SOI devices have reduced parasitic capacitances and enhanced current drive.

2.1 Short-Channel Effects

In the ongoing reduction of transistors' dimensions, the distance between the source and drain terminals in MOSFETs reduces dramatically with a consequent weakening of the capability of the Gate electrode in controlling the potential distribution and the current flux in the channel. Hence, pernicious effects called Short-Channel

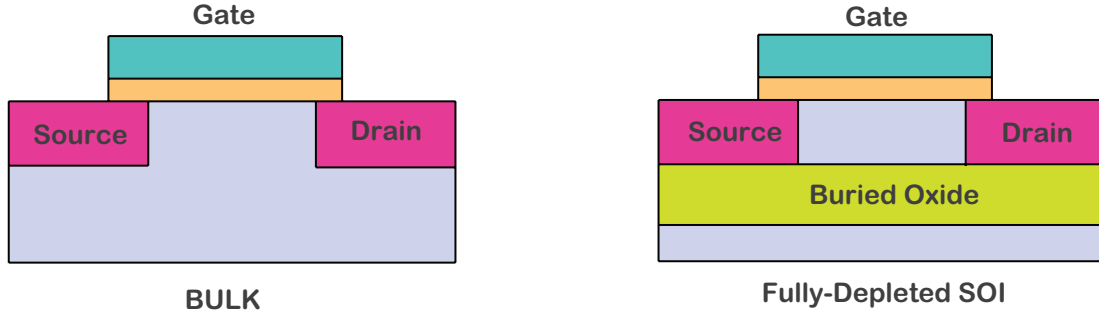


Figure 2.1. Bulk MOSFET and SOI MOSFET

Effects start afflicting MOSFETs functionalities making it impossible to shrink their dimensions below 20nm. If no solution to overcome this limitation could be envisioned, a saturation in the transistors density on chip would certainly occur.

Short-Channel Effects arise when the control on the channel region exerted by the gate is affected by the electric field lines going from drain to source. These lines propagate through the depleted areas associated with the junctions. Their impact on the channel can be reduced, for example, increasing the doping concentration in the channel. However, in very small devices doping become far too high (10^{19}at/cm^3) to allow for the device to work properly. In a "fully depleted SOI" device, on the contrary, the electric field lines addense in the buried oxide (BOX) before reaching the channel region. In this tipology of devices, short-channel effects can be more or less intense depending on the silicon and oxide thickness and on the doping concentration.

In order to give a quantitative description of Short-Channel Effects, a series of parameters has been defined. But, before proceeding with the introduction of these parameters, it is necessary to remind the definition of threshold voltage. The threshold voltage is defined as the difference between the gate and source voltage capable of determining a given surface charge density in the channel.

When increasing the applied drain-source voltage, the potential energy barrier in the channel lowers; its lowering can be quantified through the change of threshold voltage when the applied voltage is high (e.g. 1V) and low (e.g. 0.1V). We have just defined the DIBL (Drain Induced Barrier Lowiering)

$$DIBL = V_{TH}(\text{high } V_{ds}) - V_{TH}(\text{low } V_{ds}) \quad (2.1)$$

Similarly, the effect of the channel length can be expressed via the change in the threshold voltage in condition of long-channel and short-channel device. This quantity is called "Threshold Roll-off":

$$\Delta V_{TH} = V_{TH, \text{ long-channel}} - V_{TH, \text{ short-channel}} \quad (2.2)$$

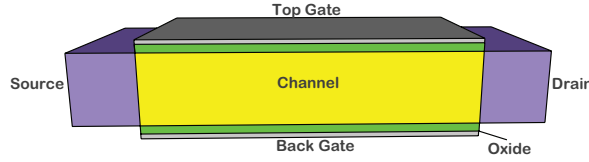


Figure 2.2. Structure of a Double-Gate Transistor.

To conclude, we define a parameter able to express how much the sub-threshold region has been modified; the "Subthreshold Swing" is given by:

$$S = \frac{\partial V_{GS}}{\partial \log I_{DS}} \quad (2.3)$$

2.2 Multi-Gate Transistors

Multi-Gate transistors represent an alternative to silicon-on-insulator MOSFETs in the attempt to increase the current drive and better control the short-channel effects. Some examples of Multi-Gate Transistors are: Double-Gate Transistors, Tri-Gate Transistors, FinFETs, Gate-All-Around Transistors. With the name "double-gate" we usually refer to the case of a single gate electrode on two opposite sides of the device structure. Analogously, things are defined for the "tri-gate". An exception is represented by the MIGFET (Multiple-Independent Gate FET) where two different gate electrodes can be biased with different voltages.

2.2.1 Double-Gate and FinFET

The first paper on Double-Gate MOSFET (fig.2.2) was published by Sekigawa and Hayashi in 1984. In that work the authors showed how a huge decrease in the short-channel effects could be obtained with the insertion of a fully-depleted SOI device between two connected gate electrodes. This device had the name XMOS because its cross-section looked like the greek letter Ξ . By adopting this configuration a better control in the depleted channel region could be obtained compared with the traditional SOI MOSFET; in particular, the impact of the electric field by the drain on the channel is less intense.

The first fabricated Double-Gate MOSFET was, however, the "fully DEpleted Lean-channel TrAnsistor (DELTA, 1989)": the device is made by a narrow and high silicon region called "fin". A modification of DELTA is the known FinFET (fig. 2.3) whose structure is similar to that of DELTA with the exception of an oxide layer (called "hard mask") on the silicon fin. The "hard mask" was introduced to prevent the formation of parasitic channels in the inversion corners in the high section of the device.

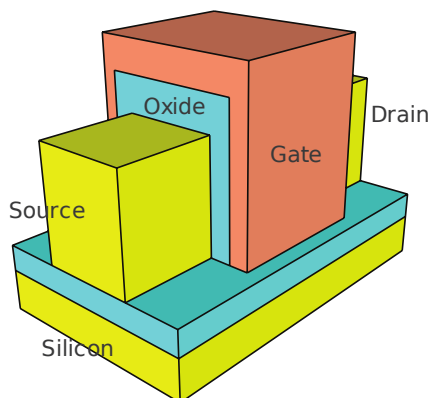


Figure 2.3. Structure of a FinFET.

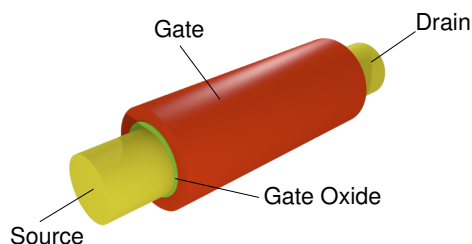


Figure 2.4. Structure of a Gate-All-Around Transistor.

The MIGFET (Multiple-Independent Gate FET) is a double-gate device whose gate electrodes are not connected together and can be biased with different voltages. The main characteristic of MIGFET is the possibility to tune the threshold voltage of the device by changing the potential on one of the gates.

2.2.2 Gate-All-Around transistors (GAA)

The structure which offers the best control on the channel region is the "Gate-All-Around" Transistor (see fig.2.4). In this case, a metal gate entirely wraps the silicon channel exerting the strongest electrostatic control. Moreover, the section of this device can be squared or circular although devices with different cross-sections have been investigated.

A collection of the most important Multi-Gate devices is shown in fig.2.5.

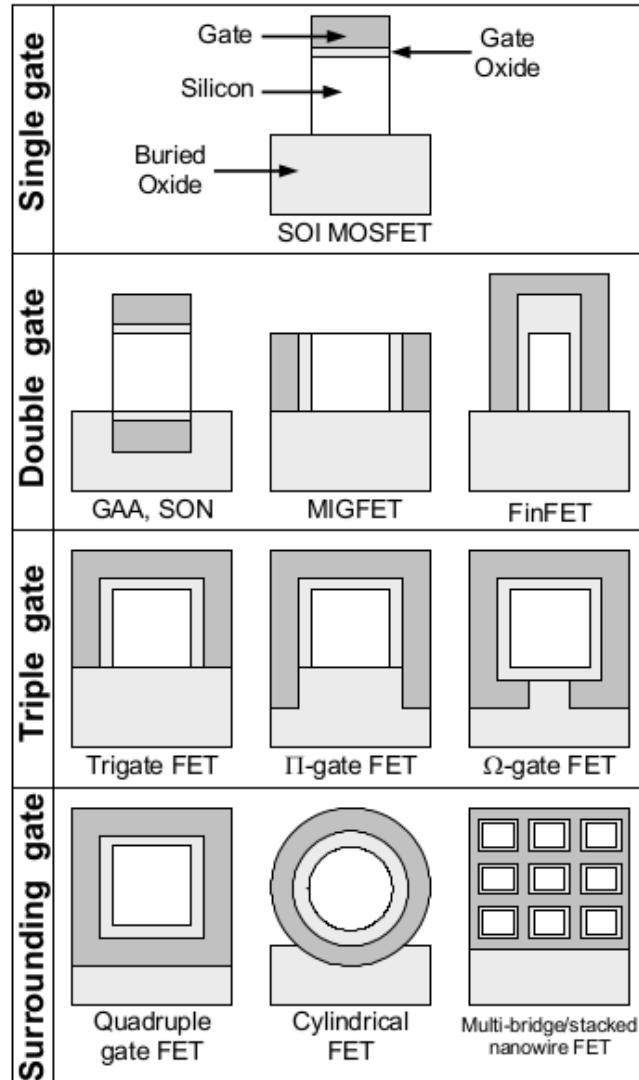


Figure 2.5. Collection of Multi-Gate Devices.

Chapter 3

The Model

3.1 Introduction

In this Chapter we will present the core of the Model. Specifically, the structure definition and the modelling approach are introduced in sect. 3.2 while the description of Quantum-Mechanical and Short-Channel Effects is postponed to sect. 3.3.4. Given the simplicity of the modelling procedure we are going to expose, some generalizations for more complex structures were possible; we will delve into them in sect. 3.4. Only in the next chapter we will present the validation results of our methodology.

3.2 Structure definition and Objectives

To apply the proposed methodology, the device is divided into a series of slices (S_i) for which an electrical model is available. The overall structure is thus decomposed into a series of sections and the study is brought back to the analysis of simpler parts. In the case of Fig. 3.1-a, for example, a single slice is represented by a single-gate Gate-All-Around MOSFET (Fig. 3.2-a). The constitutive sections don't need to be identical or to share the same parameters (they can lack a gate or differ in length). In Section 3.4, we will show, as an explicative case, how to modify the procedure when gateless sections are present and the silicon channel of the device is uniformly doped.

In the proposed method, the electrical behaviour of the single slice (hereinafter section) is supposed to be known and expressed through a model. This allows the current flowing in it to be calculated with a formula which, for GAA MOSFETs, has the form

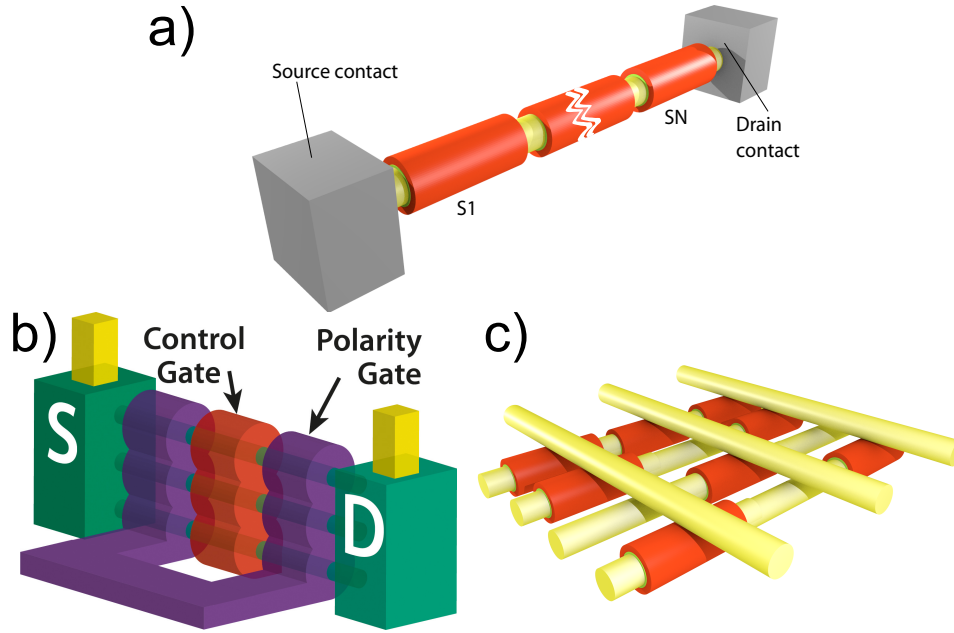


Figure 3.1. General structure of a device with multiple sections and two examples of application: a) Cascade of N Gate-All-Around MOSFETs: current and voltages are related the gate voltages and V_{DS} ; b) Structure of a Gate-All-Around Vertically Stacked Silicon Nanowire FET where different structures in a) are connected in parallel between metallic contacts and biased by three different gate potentials; c) Schematic representation of a Gate-All-Around Silicon Nanowire array: nanowires on the top layer bias the transistors on the bottom one: resulting current flows through the sections.

$$I_{DS} = \mu \frac{2\pi R}{L} \int_0^{V_{DS}} Q(V) dV \quad (3.1)$$

where μ is the mobility of carriers, L is the length of the section, R its radius, $Q(V)$ and V the density charge and the potential along the channel, respectively. Between the drain and source terminals, a potential V_{DS} is applied. The drain current of any single section S_i is then function only of the charge densities at its source and drain ends and can be thus computed independently provided that the potentials V_{Di} and V_{Si} are known.

For the entire structure of Fig. 3.1, the objective is to analyze the voltages and current along the device with no constraint on its parameters: the lengths of the sections L_1, L_2, L_3 , the applied voltages to the gates V_{g1}, V_{g2}, V_{g3} , the radius of the nanowire R and the oxide thickness t_{ox} .

The following hypothesis are necessary: no voltage drop occurs across the contacts between two adjacent sections S_i, S_{i+1} ; the current flowing in each section is the same

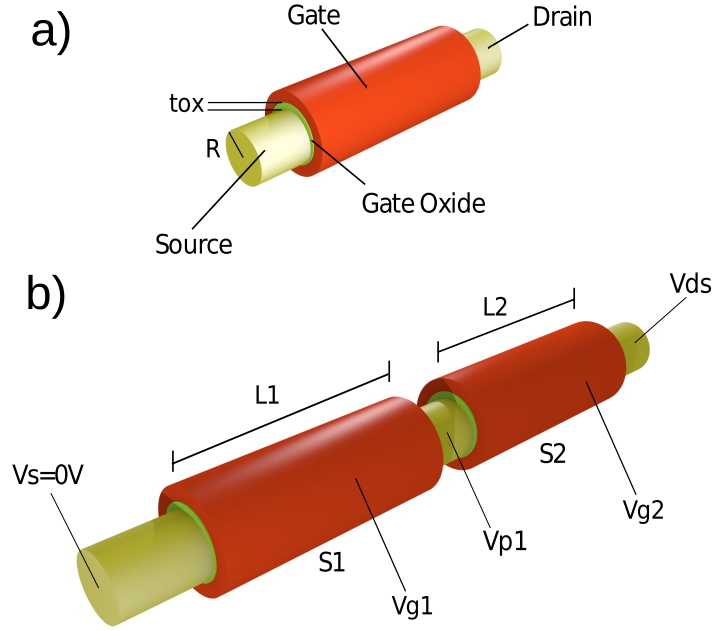


Figure 3.2. Gate-All-Around Single-Gate MOSFET and a two-section structure.

($I_{DS_i} = I_{DS_{i+1}}$). The fundamental ideas behind the proposed methodology will be outlined in the following section.

3.3 The core of the Multi-Gate Device Model

This section presents the method for calculating the voltages and currents along a structure constituted by only two physical sections in order to show the main steps in a simple case.

3.3.1 Generalities

Alg. 1 presents the steps to follow for the analysis of a two-section structure when the charge model in [113] is adopted to describe each section. This scheme is in principle almost independent of the employed charge-based model. A different choice of model would imply slight modifications in the overall method, basically requiring to solve the equations (for current, charge, etc.) outlined in Section 3.3.3 for the new expressions. The considered two-section device is depicted in Fig. 3.2-b. Its electrical behavior is exhaustively described by V_s and V_d , the potentials at its source and drain terminals, V_{p1} the potential at the interface between the sections, I_{DS_i} the current along the section S_i and Q_{si} , Q_{di} the charge densities at source and drain, respectively. The method consists of estimating the charge densities in the structure

and then of calculating the potentials and currents with successive approximations. A traditional approach in determining charge and current would proceed by reducing the number of variables in the equations. However, the strongly non-linear equations to solve do not usually admit closed-form solutions and require numerical solutions. Here, we introduce a procedure that allows us to accurately estimate the potential V_{p1} after few mathematical steps, that will provide the basis to the calculation of the current. All the steps are discussed in details in the following section.

Algorithm 1 Procedure for two sections

```

1: procedure
2:   Estimate  $Q_{s2}$  with  $Q_{s2,in}$                                 ▷ from (3.11)
3:   Calculate  $V_{p1}$                                            ▷ from (3.12)
4:   repeat
5:     Calculate  $Q_{d1}$                                          ▷ from (3.13)
6:     Calculate  $I_{DS1}$                                        ▷ from (3.15)
7:     Calculate  $Q_{s2}$                                          ▷ from (3.16)
8:     Calculate  $V_{p1}$                                          ▷ from (3.17)
9:   until  $\|V_{p1} - V_{p1@previousiteration}\| < \epsilon$ 
10:  return  $V_{p1}, I_{DS1}$ 
11: end procedure

```

3.3.2 Discussion About Convergence

The introduced relaxation method allows us to compute the solution of a non-linear system starting from an initial estimate. Its value is then gradually refined by applying repeatedly an operator until the method converges to a sufficient accuracy. In our case, we refine the value of the intermediate potential V_{p1} . The refinement process can be described, such that an operator \hat{O} is applied to V_{p1} at step m in order to obtain its value at step $m + 1$:

$$V_{p1}(m + 1) = \hat{O}V_{p1}(m) \quad (3.2)$$

This procedure is iterated until the solution is sufficiently accurate, or equivalently until the error between two successive approximations becomes smaller than an arbitrary threshold ϵ :

$$Err(m) := \|V_{p1}(m + 1) - V_{p1}(m)\| < \epsilon \quad (3.3)$$

This condition can be rewritten in terms of the operator \hat{O} , as:

$$\begin{aligned}
Err(m) &= \|\hat{O}V_{p1}(m) - V_{p1}(m)\| = \|(\hat{O} - \mathbf{1})V_{p1}(m)\| \\
&= \|(\hat{O} - \mathbf{1})\hat{O}V_{p1}(m-1)\| \\
&= \|\hat{O}(\hat{O} - \mathbf{1})V_{p1}(m-1) + \hat{K}V_{p1}(m-1)\| \\
&\leq \|\hat{O}\|Err(m-1) + \|\hat{K}\| \|V_{p1}(m-1)\|
\end{aligned} \tag{3.4}$$

In (3.4), we expressed the error at step m as a function of the error at the preceding step and we introduced the non-linear operator $\hat{K} := [\hat{O}, \hat{O} - \mathbf{1}]$ defined as the commutator of the two operators in brackets, with $\mathbf{1}$ is the identity operator. At this point, a formal analysis would be required to validate the convergence of the error. However, such formal proof is difficult due to the strong non-linearity of the operators involved, as highlighted in the following sections. Moreover, the nature itself of the operator \hat{O} depends on several physical parameters (channel lengths, gate voltages, ...) which can vary over a large physical domain, thus making the analytical treatment difficult. Hence, a general proof for the gradual reduction of the error will not be proposed here. We resort, instead, to present a heuristic reasoning which justifies the convergence of the approach.

In the considered device structure, the currents flowing through the different sections are the same, namely $I_{DS1}(V_{p1}(m)) = I_{DS2}(V_{p1}(m))$. According to the device physics, the two currents are continuous functions of V_{p1} , respectively monotonically increasing and decreasing. The value of $V_{p1}(m+1)$ is computed by evaluating one of the members of the equation and solving the resulting expression for a new value of V_{p1} . If the value of V_{p1} used as an estimate is larger than its exact solution, then the next value $V_{p1}(m+1)$ will be smaller than the exact solution since only a smaller potential allow the same current to flow through the devices. The same consideration holds if the estimate of V_{p1} is larger than the exact solution. Thus, the sequence of values of V_{p1} are alternatively larger and smaller with respect to the exact value V_{p0} . If the initial difference between the initial guess and the exact solution is not too large, the method will converge to the exact solution in most cases. For the initial value adopted in the paper, convergence has been verified by extensive simulation for a large variety of parameters' choice. In case of missed convergence, a different initial guess can be used.

3.3.3 Closed Form Expressions Derivation

The introduced procedure requires to solve closed form expression a certain number of times. This number depends on the accuracy to be met: for greater accuracy, a better estimate of Q_{s2} is required. Results will show that this number is usually very small and dependent on the number of sections. In what follows, the equation for

the potential has been written for intrinsic channel. In Section 3.4.3, the derivation for a doped channel will be shown.

According to the hypothesis that the current flowing in each section is the same, we start by imposing the condition $I_{DS1} = I_{DS2}$. By referring to the formula for the current from the model in [113], this is equivalent to (3.5):

$$\begin{aligned} & \mu \frac{2\pi R}{L_1} \left[2 \frac{kT}{q} (Q_{s1} - Q_{d1}) + \frac{Q_{s1}^2 - Q_{d1}^2}{2C_{OX}} + \frac{kT}{q} Q_0 \log \left[\frac{Q_{d1} + Q_0}{Q_{s1} + Q_0} \right] \right] = \\ & = \mu \frac{2\pi R}{L_2} \left[2 \frac{kT}{q} (Q_{s2} - Q_{d2}) + \frac{Q_{s2}^2 - Q_{d2}^2}{2C_{OX}} + \frac{kT}{q} Q_0 \log \left[\frac{Q_{d2} + Q_0}{Q_{s2} + Q_0} \right] \right] \end{aligned} \quad (3.5)$$

where kT/q (henceforth V_{th}) is the volt-equivalent of temperature, where Boltzmann's constant k must be in units of J/K and the temperature T is in units of K . The unit of charge q is $1.6022 \times 10^{-19}C$. Q_0 is a constant with the dimension of a charge, whose value is $(4\epsilon_{Si}/R) \times (kT/q)$, and C_{OX} is the oxide capacitance of a cylindrical capacitor given by $\epsilon_{OX}/(R \log(1 + t_{OX}/R))$. Q_{di} and Q_{si} relate to the potentials at the source and drain ends by the charge-control equation (3.6), where $V = V_{si}$ and $V = V_{di}$ for the two cases Q_{di} and Q_{si} respectively:

$$\begin{aligned} V_{GSi} - \Delta\varphi - V - \frac{kT}{q} \log \left(\frac{8}{\delta R^2} \right) &= \frac{Q}{C_{OX}} + \\ &+ \frac{kT}{q} \log \left(\frac{Q}{Q_0} \right) + \frac{kT}{q} \log \left(\frac{Q + Q_0}{Q_0} \right) \end{aligned} \quad (3.6)$$

where $\Delta\varphi$ is the difference between gate metal and silicon working functions. No analytical solution for the charge densities and V_{p1} can be found from (3.5) and (3.6). However, we can actually realize that, in our problem, we have:

$$V_{s1} < V_{d1} \equiv V_{p1} \quad (3.7)$$

$$V_{s2} \equiv V_{p1} < V_{DS} \quad (3.8)$$

These inequalities express the fact that, assuming that the potential on the source of the structure is zero ($V_{s1} = 0V$) and that a positive voltage V_{DS} is imposed to the whole structure (a negative V_{DS} does not imply modifications due to the symmetry), a positive voltage drop occurs on each of the two inner regions between their drain and source terminals. This is to say that the drain potential is larger than the source potential on both inner devices. These considerations made, the monotonic trend of charge with voltage revealed by (3.6) yields consequently:

$$Q_{d1} < Q_{s1} \quad (3.9)$$

$$Q_{d2} < Q_{s2} \quad (3.10)$$

As a first approximation, we can neglect Q_{d1} and Q_{d2} in (3.5) in order to find an initial estimation of Q_{s2} and solve the resulting equation (3.11). We stress here that this is only an initial estimate for the charge densities at the drain contacts, which will be corrected by successive iterations of the procedure. The obtained approximate initial value of Q_{s2} is called $Q_{s2,in}$:

$$\frac{1}{2C_{OX}L_2}Q_{s2,in}^2 + \frac{2V_{th}}{L_2}Q_{s2,in} - \frac{Q_{s1}^2}{2C_{OX}L_1} - \frac{2V_{th}Q_{s1}}{L_1} = 0 \quad (3.11)$$

With the obtention of $Q_{s2,in}$, V_{p1} is easily found by directly solving the charge-control equation (3.6) as:

$$\begin{aligned} V_{G2} - \Delta\varphi - V_{p1} - \frac{kT}{q} \log \left(\frac{8}{\delta R^2} \right) &= \frac{Q_{s2,in}}{C_{OX}} + \\ &+ \frac{kT}{q} \log \left(\frac{Q_{s2,in}}{Q_0} \right) + \frac{kT}{q} \log \left(\frac{Q_{s2,in} + Q_0}{Q_0} \right) \end{aligned} \quad (3.12)$$

This value of V_{p1} is, however, only a rough estimate whose accuracy needs to be improved. We proceed then and compute Q_{d1} through (3.13) and (3.14):

$$Q_{d1} = C_{OX} \left(-\frac{2C_{OX}V_{th}^2}{Q_0} + \sqrt{\left(\frac{2C_{OX}V_{th}^2}{Q_0} \right)^2 + B} \right) \quad (3.13)$$

$$B = 4V_{th}^2 \log^2 \left(1 + \exp \left(\frac{V_{GS1} - V_T + \Delta V_T - V_{p1}}{2V_{th}} \right) \right) \quad (3.14)$$

These relations, taken from [114], give reasonably accurate solutions to (3.6). The parameters non explicit here, such as $V_T, \Delta V_T$ or V_0 , can be found in [114]. In particular, V_T corresponds to the threshold voltage and plays a crucial role in describing the quantum mechanical and short-channel effects in the device, as it will be described in the next subsection. From Q_{d1} , the current I_{DS1} in the first section is given by (3.15):

$$\begin{aligned} I_{DS1} = \mu \frac{2\pi R}{L_1} \left[2 \frac{kT}{q} (Q_{s1} - Q_{d1}) + \frac{Q_{s1}^2 - Q_{d1}^2}{2C_{OX}} + \right. \\ \left. + \frac{kT}{q} Q_0 \log \left[\frac{Q_{d1} + Q_0}{Q_{s1} + Q_0} \right] \right] \end{aligned} \quad (3.15)$$

The current must be equal in the two sections. Imposing again the condition (3.5), we now get a new equation for Q_{s2} (3.16):

$$\begin{aligned} \frac{1}{2C_{OX}}Q_{s2}^2 + 2V_{th}Q_{s2} - \frac{I_{ds1}L_2}{2\pi\mu R} \frac{Q_{s1}^2}{2C_{OX}L_1} - 2V_{th}Q_{d2} + \\ - \frac{Q_{d2}^2}{2C_{OX}} + V_{th}Q_0 \log \left(\frac{Q_{d2}^2 + Q_0}{Q_{s2,in} + Q_0} \right) = 0 \end{aligned} \quad (3.16)$$

Finally, a more accurate estimate of V_{p1} can be found by substituting this new value in (3.17):

$$\begin{aligned} V_p = V_{G2} - \Delta\varphi - \frac{kT}{q} \log \left(\frac{8}{\delta R^2} \right) - \frac{Q_{s2}}{C_{ox}} + \\ - \frac{kT}{q} \log \left(\frac{Q_{s2}}{Q_0} \right) - \frac{kT}{q} \log \left(\frac{Q_{s2} + Q_0}{Q_0} \right) \end{aligned} \quad (3.17)$$

The introduced procedure allows us to describe voltages and currents in a structure consisting of two different sections by means of a limited number of computational steps. It does not require numerical solutions of nonlinear equations, which usually represent a consequent overhead on the computational efficiency and time requirements. A fundamental feature of the proposed method is its iterative nature. Steps can be repeated in sequence in order to meet the accuracy requirements (see Alg. 1). Yet, good accuracy of data after only one iteration has been verified for two-sections devices (two iterations are necessary for three-sections). This will be shown in next sections.

3.3.4 Quantum mechanical (QME) and Short-Channel effects (SCE)

When the dimensions of the sections enter the nanometer range ($< 10nm$), quantum mechanical effects start affecting the behaviour of the device. Consequently, the charge density should be computed taking into account the quantum potential confinement inside the channel. Following [124] and [125], this effect produces a bandgap opening which can be described with a semiempirical shift of the threshold voltage V_T in the compact model on which our procedure relies. The change of V_T is

$$\Delta V_{T(QME)} = \frac{\Delta E_{qm}}{q}$$

where ΔE_{qm} is the shift of the conduction band due to potential confinement. Its actual expression depends on the geometry of the sections and on the assumption

made on the shape of the confining potential.

Analogously, SCE and DIBL are modelled with an extra shift in the threshold voltage given by

$$\Delta V_T = -2\gamma_{SCE}(V_{To} - V) + \gamma_{DIBL}V_{ds}$$

where V_{To} is the long-channel threshold voltage while the parameters γ_{SCE} and γ_{DIBL} are determined trough extrapolation from simulation results.

3.4 Generalizations of the method to more complex structures

The method illustrated in the preceding section can be extended to more complex structures. Indeed, our method presents features which make it useful to describe a wide variety of problems. The most important is its independence on the model adopted for describing each section. In the following, we describe how to modify it, while maintaining the same model in each section, when the number of connected devices is arbitrary (subsect. A), when devices without gate contact are considered (subsect. B) and when doped-channel sections are present in the structure (subsect. C). The whole procedure will be illustrated and schematized. Finally, some considerations are made about the possibility of adapting the method also to devices with different geometry with respect to Gate-All-Around MOSFETs (subject. D).

3.4.1 Arbitrary Number of Gates

The method enables an efficient description of structures with an arbitrary number of gates as illustrated in Fig. 3.3. By referring to the model proposed in [113], the extension of the algorithm proposed to this general case is almost straightforward (see Alg. 2). By supposing that the current flowing in each of the n devices is the same, we impose that for $i = 2, \dots, n$:

$$I_{DSi} = I_{DS1}$$

The choice of current I_{DS1} in the above equation is arbitrary and any other current in the device could be adopted. Under the initial assumption $Q_{di} < Q_{si}$, this leads to the following equation to a first estimate $Q_{si,in}$ of Q_{si} :

$$\frac{1}{2C_{OX}L_i}Q_{si,in}^2 + \frac{2V_{th}}{L_i}Q_{si,in} - \frac{Q_{s1}^2}{2C_{OX}L_1} - \frac{2V_{th}Q_{s1}}{L_1} = 0 \quad (3.18)$$

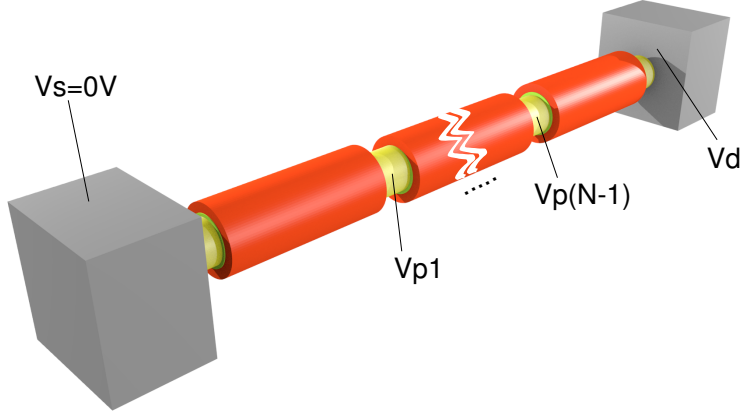


Figure 3.3. N -section Structure.

The voltages at the interface of adjacent sections V_{pi} can then be described with the charge-control equation:

$$V_{Gi} - \Delta\varphi - V_{pi} - \frac{kT}{q} \log \left(\frac{8}{\delta R^2} \right) = \frac{Q_{si,in}}{C_{OX}} + \frac{kT}{q} \log \left(\frac{Q_{si,in}}{Q_0} \right) + \frac{kT}{q} \log \left(\frac{Q_{si,in} + Q_0}{Q_0} \right) \quad (3.19)$$

The charge densities at the drain, instead, are given by (3.13) and (3.14). The current comes from:

$$I_{DSi} = \mu \frac{2\pi R}{L_i} \left[2 \frac{kT}{q} (Q_{si} - Q_{di}) + \frac{Q_{si}^2 - Q_{di}^2}{2C_{OX}} + \frac{kT}{q} Q_0 \log \left[\frac{Q_{di} + Q_0}{Q_{si} + Q_0} \right] \right] \quad (3.20)$$

with $i = 1, \dots, n-1$. Given the currents, the charge densities at source ends Q_{si} and the values for V_{pi} are obtained from the following equations respectively:

$$\frac{1}{2C_{OX}} Q_{si}^2 + 2V_{th} Q_{si} - \frac{I_{DS1} L_i}{2\pi\mu R} \frac{Q_{s1}^2}{2C_{OX} L_1} - 2V_{th} Q_{di} + \frac{Q_{di}^2}{2C_{OX}} + V_{th} Q_0 \log \left(\frac{Q_{di}^2 + Q_0}{Q_{si,in} + Q_0} \right) = 0 \quad (3.21)$$

$$V_{pi} = V_{G(i+1)} - \Delta\varphi - \frac{kT}{q} \log \left(\frac{8}{\delta R^2} \right) - \frac{Q_{s(i+1)}}{C_{ox}} - \frac{kT}{q} \log \left(\frac{Q_{s(i+1)}}{Q_0} \right) - \frac{kT}{q} \log \left(\frac{Q_{s(i+1)} + Q_0}{Q_0} \right) \quad (3.22)$$

The aforementioned procedure is summarized in Alg. 2, for an illustrative number of sections equal to three. Starting from an estimate of Q_{s2} and Q_{s3} , the procedure iterates four closed form calculations to attain voltage (V_{p1} , V_{p2}) and current (I_{ds}) results.

Algorithm 2 Procedure for three sections

```

1: procedure
2:   Estimate  $Q_{s2}$  and  $Q_{s3}$  with  $Q_{s2,in}$  and  $Q_{s3,in}$ 
3:                                     ▷ from (3.18)
4:   repeat
5:     Calculate  $Q_{d1}$  and  $Q_{d2}$                                      ▷ from (3.13)
6:     Calculate  $I_{DS1}$ ,  $I_{DS2}$  and  $I_{DS3}$                              ▷ from (3.20)
7:     Calculate  $Q_{s2}$  and  $Q_{s3}$                                      ▷ from (3.21)
8:     Calculate  $V_{p1}$  and  $V_{p2}$                                      ▷ from (3.22)
9:   until Accuracy not met
10:  return  $V_{p1}$ ,  $V_{p2}$ ,  $I_{DS1}$ 
11: end procedure

```

3.4.2 Gateless Sections

As stated in the previous chapter, not all parts of complex devices are gated. Fig.3.4 shows an example of a structure where an inner section is not wrapped with a gate. The problem of determining the potential along the structure and the resulting

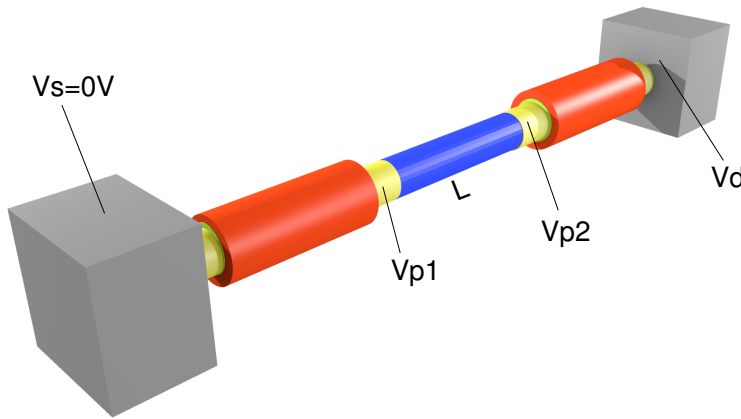


Figure 3.4. Structure with a gateless section

current can be addressed easily through the method already discussed with only

slight modifications. Let us define the parameters related to a gateless section: L_R the length of the section, N_D its doping level and R its radius. No control is actually exerted externally on the charge density along the gateless section. In the context of Fig. 3.4, where the inner part is gateless, this leads to a simple resistive behavior of the slice:

$$V_{p1} = V_{p2} - RI_{DS2} \quad (3.23)$$

where the resistance of the channel is related to the channel length and doping level by:

$$R = \rho \frac{L_R}{A} = \frac{1}{q\mu N_D} \frac{L_R}{2\pi R^2} \quad (3.24)$$

where A is the section of the channel, L_R its length and ρ the channel resistivity. By introduction of this new equation into the previous methodology, one gets a simple algorithm to derive potentials V_{p1}, V_{p2} and current I_{DS} . Alg. 3 describes schematically the whole iterative process, that is again very close to the one presented in Section 3.3.3 for a two-sections structure. The main difference between the two is given by (3.23) which is now adopted to compute V_{p1} instead of (3.22).

Algorithm 3 Procedure for structures with gateless sections

```

1: procedure
2:   Estimate  $Q_{s2}$  with  $Q_{s2,in}$                                 ▷ from (3.11)
3:   Calculate  $V_{p2}$                                               ▷ from (3.22)
4:   repeat
5:     Calculate  $Q_{d2}$                                            ▷ from (3.13)
6:     Calculate  $I_{DS2}$                                            ▷ from (3.20)
7:     Calculate  $V_{p1}$                                            ▷ from (3.23)
8:     Calculate  $Q_{d1}$                                            ▷ from (3.13)
9:     Calculate  $I_{DS1}$  and  $Q_{s2}$                                 ▷ from (3.20) and (3.16)
10:    Calculate  $V_{p2}$                                            ▷ from (3.22)
11:   until Accuracy not met
12:   return  $V_{p1}, V_{p2}, I_{DS1}$ 
13: end procedure

```

3.4.3 Doped Channel Sections

We now adapt the general procedure to doped channel sections. The structure is formally identical to the one shown in Fig. 3.3 and the change in doping level can be described in the charge-model of a single section. By referring to the model in [113], it suffices to reanalyze the entire procedure leading to the final formulas for current

and charge densities along the channel and to modify the inputs of the problem. The main difference which arises in the model's deduction is a new solution of the Poisson equation for the potential in a perpendicular direction to the channel length. If N_A is defined to be the channel doping (all the remaining quantities do not vary), the solution becomes, after a few approximations not reproduced here for the sake of brevity:

$$\psi(r) = -\delta \frac{N_A}{4n_i} \frac{kT}{q} R^2 + \delta \frac{N_A}{4n_i} \frac{kT}{q} r^2 + V + \frac{kT}{q} \log \left(\frac{-8B}{\delta(1 + Br^2)^2} \right) \quad (3.25)$$

This is the first step to move forward a charge-control equation. By imposing the appropriate boundary condition at the channel-oxide interface [113], one finally arrives to (3.26) relating the charge density to the potential along the channel:

$$\begin{aligned} V_{GS} - \Delta\varphi - V - \frac{kT}{q} \log \left(\frac{8e^{\alpha/(V_i C_{ox})}}{\delta \frac{N_A}{n_i} R^2} \right) &= \\ &= \frac{Q - \alpha}{C_{ox}} + \frac{kT}{q} \log \left(\frac{Q - \alpha}{Q_0} \right) + \frac{kT}{q} \log \left(\frac{Q - \alpha + Q_0}{Q_0} \right) \end{aligned} \quad (3.26)$$

where the only new quantity is $\alpha = \varepsilon_{Si} \frac{N_A}{2n_i} \frac{kT}{q} R$, a parameter related to the device structure and obviously to its channel doping. By noticing the numerous similarities between this formula and (3.6), it is possible to apply slight substitutions to (3.26) in order to fall back on the one previously discussed. The change of variables to be accomplished is:

$$Q \leftarrow Q^* = Q - \alpha \quad (3.27)$$

$$\delta \leftarrow \delta^* = \frac{e^{\alpha/(C_{ox} V_i)}}{N_A/n_i} \quad (3.28)$$

This small changes make it easy and effortless to include such a modification in the general frame of the method for the solution of structures with doped channels.

3.4.4 Sections with Different Geometry

The proposed method also applies to problems where devices with a different geometry are involved. Again, this is performed by substituting the employed models in the different sections. An interesting case is the cascade of FinFETs, where the models from [106] and [125] can be effortlessly adopted in applying the methodology discussed here, thanks to their evident similarities with [113] for Gate-All-Around MOSFETs.

Chapter 4

Verification and Results

This chapter focuses on techniques and procedures used to implement and verify the results of the methodology we described in the previous chapters. Specifically, we will deal with the tests that we performed for devices of growing complexity (Sections 4.2 to 4.3) and under different biasing conditions (Sections 4.4).

4.1 Methodology

This methodology was developed in Matlab [126], mainly because the focus of the work, at an early stage, was accuracy and scalability and Matlab language allows rapid prototyping. The structure considered in the experiments is shown in Fig. 3.3. Most of the results shown are for two and three section devices, but data are provided from experiments up to nine sections. The method was validated through an extensive experimental comparison of results with the exact numerical solution and with the output from a physics-based software. Specifically, we have computed the potential at the interface between different sections in various multiple-gate structures as a function of the applied voltages and structural parameters. Data were then compared with two set of results calculated by TCAD software Atlas including the computation of quantum mechanical effects [127]. The first set was obtained numerically for the entire structure, while the second one considers the values obtained just for potentials (V_{p1} , V_{p2}) from the numerical simulation. This approach was chosen to better assess the validity of the algorithm that estimates potentials into the structure and the relative importance of this step into the overall procedure. Simulations in Atlas were performed under the assumption of a Boltzmann distribution for carriers in the silicon channel and of highly doped contacts ($10^{23}cm^{-3}$). The latter condition guarantees a small voltage drop across the contacts themselves. Complex structures analyzed present sections with channel radius between $5nm$ and $10nm$ while their oxide thickness is $1.5nm$. Quantum mechanical

effects, and in particular the potential confinement, which are expected to play a role in the device characteristics in this range of geometrical parameters, are taken into account as described in section 3.3.4. Analogously, the short-channel effects, *Drain Induced Barrier Lowering* (DIBL), sub-threshold swing and mobility degradation are, indeed, consistently modelled in the charge-model adopted of each section. The channel lengths of simulated devices range from $60nm$ to $300nm$. These dimensions of channel length are, instead, sufficiently high for ballistic transport not to take place and for coherent transport not to become evident. Hence, diffusive regime of transport is assumed.

4.2 Two-Section Structure

Fig. 4.1 shows the potential V_{p1} in a two-section device for different values of gate voltage V_{g2} with varying drain-source voltage. Each section is $300nm$ long, has radius $R = 6nm$ and oxide thickness $t_{OX} = 1.5nm$. The gate voltage applied to the first section is $V_{g1} = 0.6V$. The graph reveals that our numerical procedure, after only one iteration step, gives accurate outputs if compared with the exact numerical solution. Indeed, maximum relative errors of 1.6% are obtained after one iteration. Thus, for a two-section structure, only one iteration is actually sufficient to get accurate results. This is also true if we let other parameters vary in the same structure, such as in Fig. 4.2 where the length of section L_2 is varied between $60nm$ and $450nm$ while L_1 is kept at $L_1 = 300nm$. We compared also the results with the simulation data from TCAD Atlas.

Fig. 4.3 and Fig. 4.4 present the data from the simulator corresponding to the plots of Fig. 4.1 and Fig. 4.2 respectively. Coherence of values is observable. Worst relative errors of a few percent are obtained for relatively large V_{DS} polarization combined with shorter channel. For longer channels, relative errors well below 1% are obtained over the full biasing range.

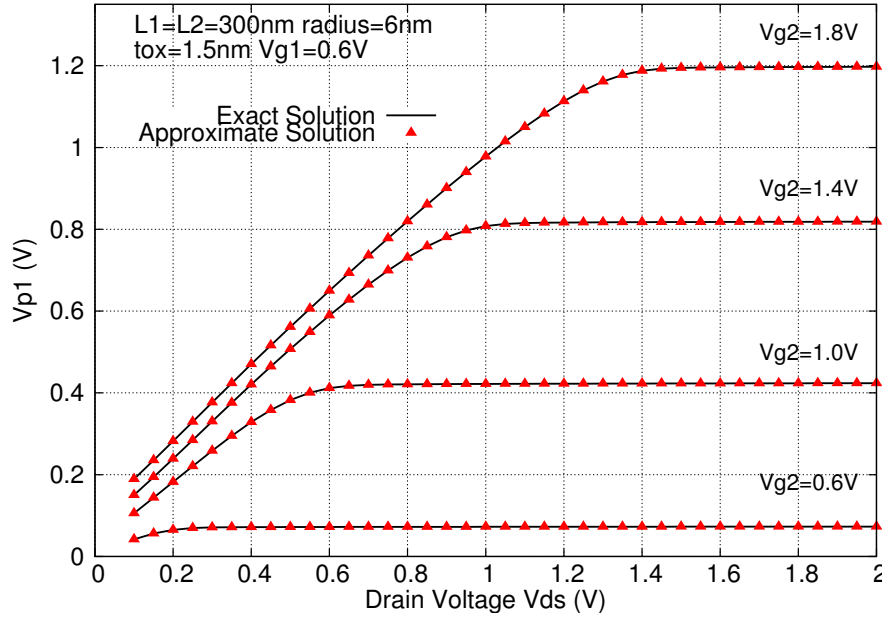


Figure 4.1. Comparison of the exact solution of V_{p1} with data from the model in a two-section structure for different values of V_{g2} ; in the inset a zoom of the region with low V_{ds} is shown.

4.3 Three-Section Structure

While augmenting the complexity of the structure by cascading more sections, the method preserves its validity and accuracy. This is shown for a three-section device in Fig. 4.5, where the potentials at the interface between the two sections are represented as a function of the total voltage applied. Data were obtained by iterating just twice the proposed method. This led to a discrepancy in results from numerical simulations that tops to a few tenth of percent across the full range of potentials considered. A direct comparison was also made with Atlas simulation outputs. Fig. 4.6 plots the values of V_{p2} for different V_{g3} in a structure of three sections with $L_1 = L_3 = 300nm$, $L_2 = 150nm$, $R = 6nm$, $V_{g1} = 0.6V$ and $V_{g2} = 0.8V$. Data largely agree with simulation results, with relative errors of few percent over the full biasing range (V_{g2} from 1V to 2V), showing little sensitivity of the methodology to variations in V_{g2} .

In Fig. 4.7, the potential V_{p2} with varying V_{DS} for different values of L_3 are shown. Data from Atlas stand close to the numerical model adopted also for high voltages.

From the values of potentials obtained, the current has been estimated. Fig. 4.8 shows the current flowing in a three-section structure when V_{g1} and V_{g3} are kept

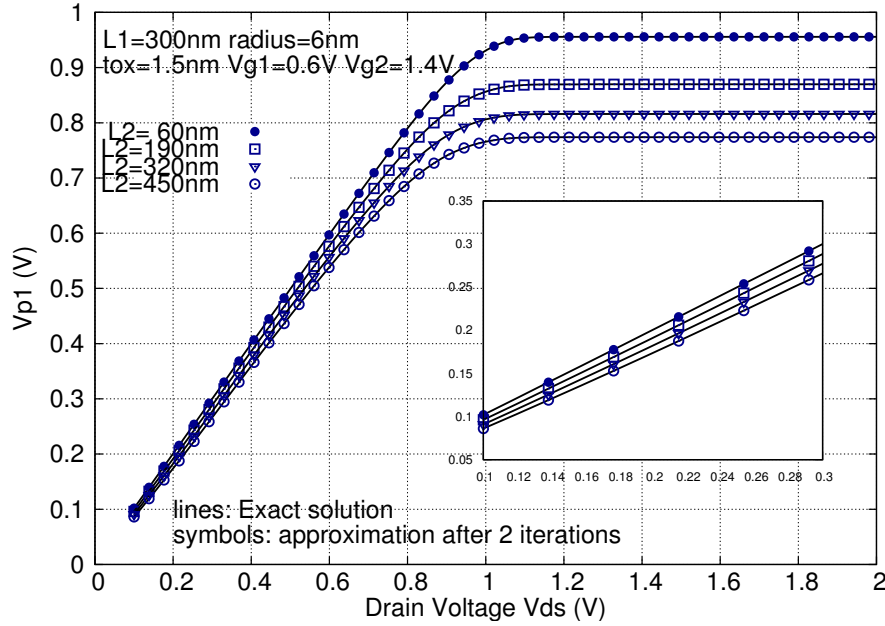


Figure 4.2. Comparison of the exact solution of V_{p1} with data from the model in a two-section structure for different values of L_2 ; region with low V_{ds} is shown in a larger scale in the right box of the figure.

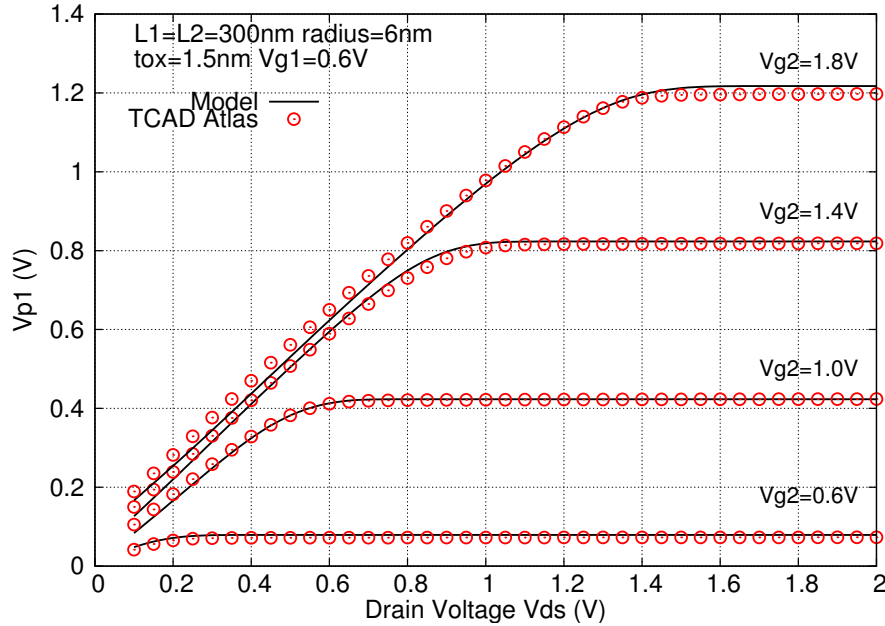


Figure 4.3. Comparison of the exact solution of V_{p1} with output from TCAD Atlas: two-section structure for different values of V_{g2} .

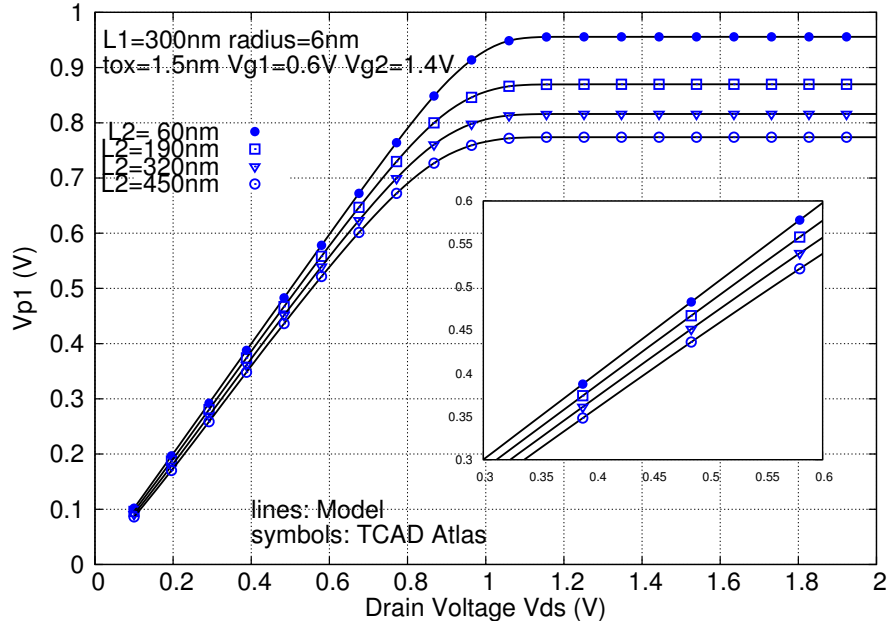


Figure 4.4. Comparison of the exact solution of V_{p1} with output from TCAD Atlas in a two-section structure for different values of L_2 .

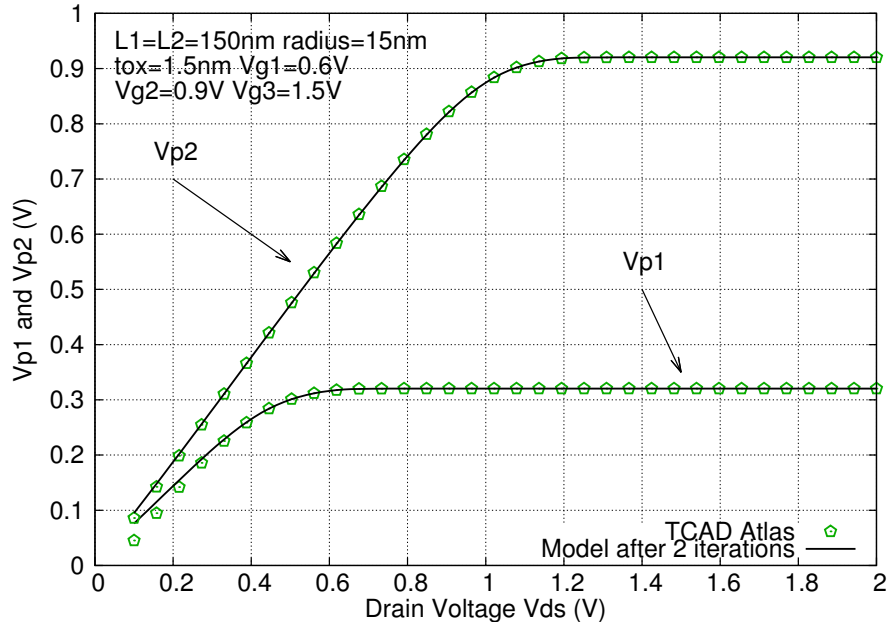


Figure 4.5. Comparison of the exact solution of V_{p1} and V_{p2} with data from the method in a three-section structure.

fixed while V_{g2} is varied. Comparison with data from Atlas in linear and logarithmic

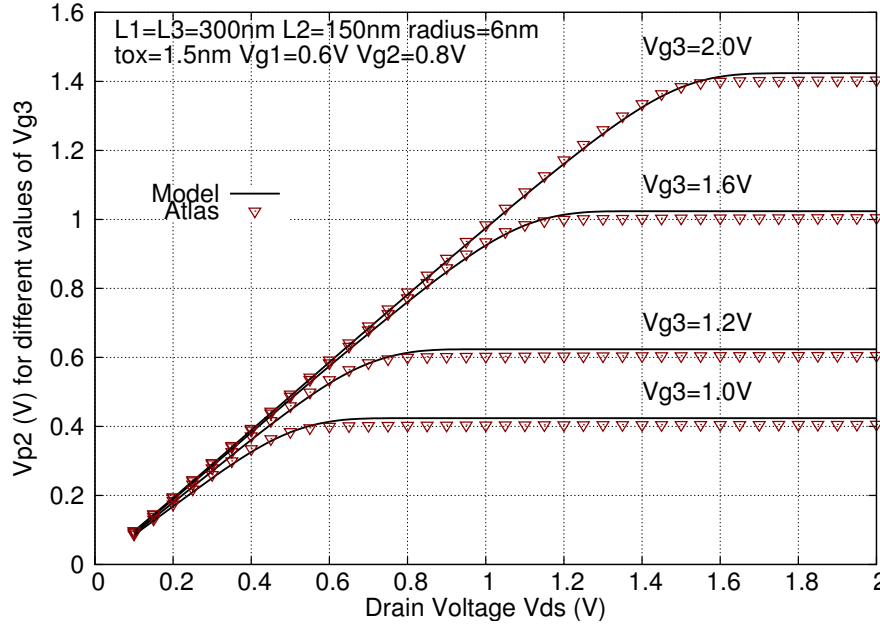


Figure 4.6. Comparison of the exact solution of V_{p2} with data from TCAD Atlas in a three-section structure for different values of V_{g3} .

scale shows good accuracy over the whole range of applied voltages. More precisely, the figure reveals how the operating region of the central section changes when the gate voltage applied is varied. For small values of V_{g2} the section operates in sub-threshold region since its gate voltage is lower than V_{g1} , thus limiting the overall current flowing into the device. When V_{g2} is increased over $V_{g1} = 0.6V$, the section exits the subthreshold region and enters saturation: then the current continues to increase but with a lower growing rate.

4.4 Three-Section Structure with Fixed Gate Voltages at Extremes

Structures with three sections are often used to realize double-gate devices by fixing the same potential on the two lateral gates [116], thereby leading to the condition $V_{g1} = V_{g3}$. Fig. 4.9 and Fig. 4.10 show how V_{p1} and V_{p2} vary with V_{DS} when V_{g2} is kept constant and $V_{g1} = V_{g3}$. Exact numerical data and method output are represented. Using the obtained values for V_{p1} and V_{p2} , the current flowing in the series of the sections has been subsequently evaluated and compared with numerical exact. In Fig.4.11, a plot of relative errors on current value is shown. In the worst

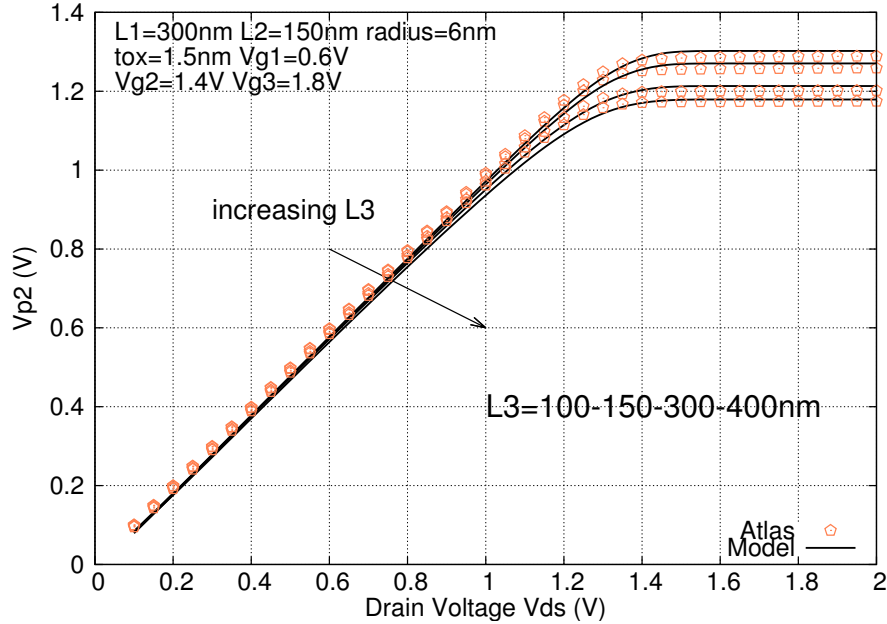


Figure 4.7. Comparison of the exact solution of V_{p2} with data from TCAD Atlas in a three-section structure for different values of L_3 .

case, the strongly non-linear error tops at 4%.

4.5 Gateless Section Structure

Finally, we present an example of data obtained for a structure with gateless section. Fig. 4.12 shows the relative errors of V_{p1} and V_{p2} as a function of V_{DS} with respect to the exact values of potential. A maximum error of 1.8% is obtained. This section is required to correctly model the region of multi-gate devices with uniform doping level, as detailed before. Relative error tops for very low V_{DS} , with 0.1% at $V_{DS} = 1\text{V}$.

4.6 Computation Times

A final discussion is worth doing on the timing efficiency of our model. The experiments have been performed on MIG devices made of up to nine sections under different biasing conditions, reported for each test. Some results are worth pointing out for test cases that are particularly significant. For a three section structure, relative errors on I_{DS} of less than 4% are shown in Fig. 4.11. From a timing perspective, current evaluation for the mentioned cases required less than 0.2ms in an

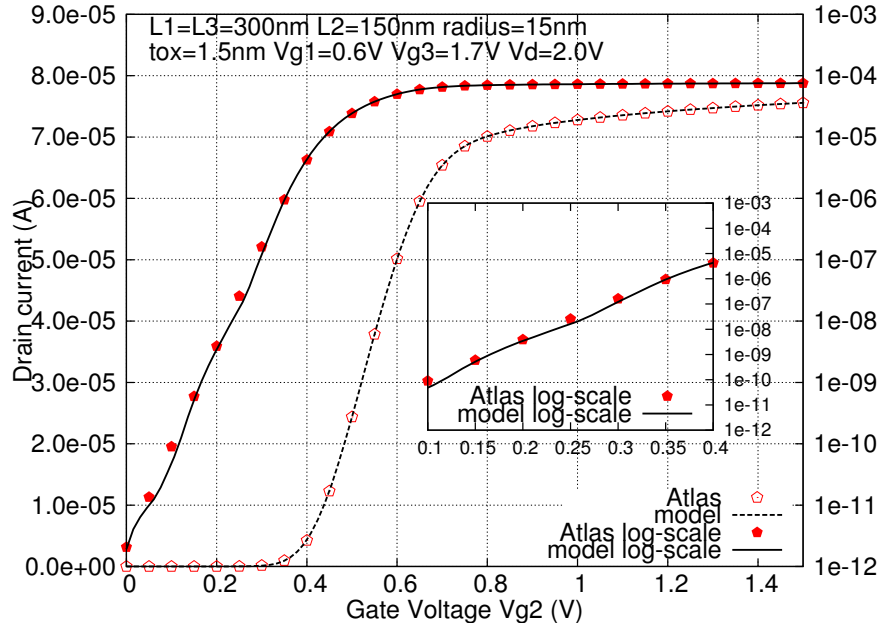


Figure 4.8. Current I_{DS} in a three-section structure where $V_{g1} = V_{g3}$ for different values of V_{g2} . Dotted line: current from the model in linear scale; solid line: current from the model in logarithmic scale. Points represent data from simulator Atlas in linear and logarithmic scale.

interpreted language, with given drain and gate voltages. These times result one order of magnitude shorter than computation times necessary for a numerical solution where tenths of milliseconds are necessary. The method is, therefore, computationally efficient.

Fig. 4.13 shows CPU times necessary to solve potentials and currents in structures with a variable number of devices under a single bias condition. Both curves reveal a linear trend with the number of devices connected. We kept the number of iterations (1IT) of the model constant along the bottom curve (squares) obtaining an overall proportionality of time and number of sections, but a variable accuracy (between acc10% to more than acc40% in the worst case). In the other case, we adopted a variable number of iterations in order to get a particular level of accuracy (acc3%). One iteration (1IT) was necessary for a two-section structure, and three iterations for all the others (3IT). Still the trend remains linear and the computation times approximately doubles. Similar iterations performed using a spice engine (Eldo) required more than one order of magnitude in time. Clearly, this is not affordable in a context where thousand of devices are to be simulated in the same time.

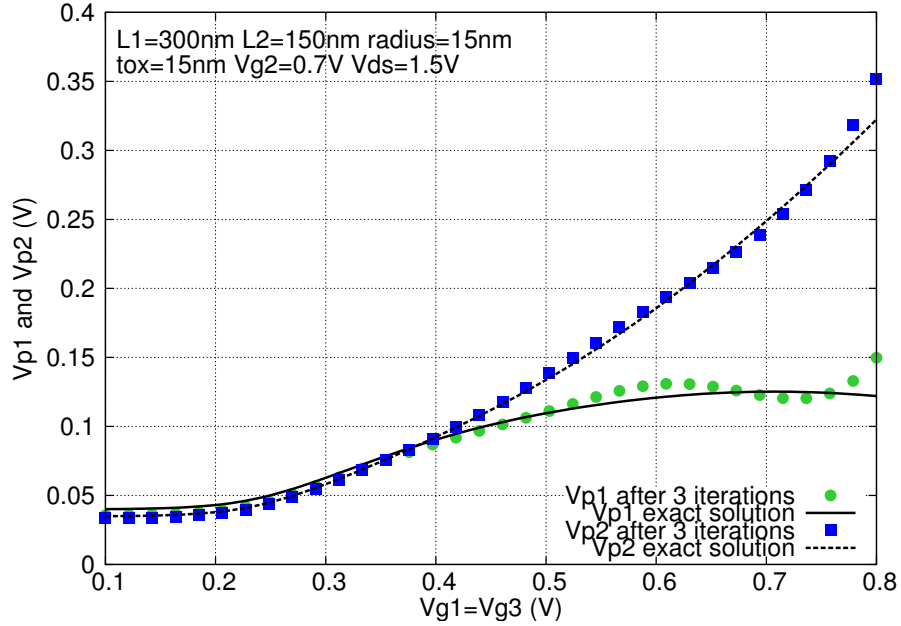


Figure 4.9. Comparison of values of V_{p1} and V_{p2} obtained from the method after three iterations with exact results in a triple structure with $V_{g1} = V_{g3}$, $V_{g2} = 0.7\text{V}$.

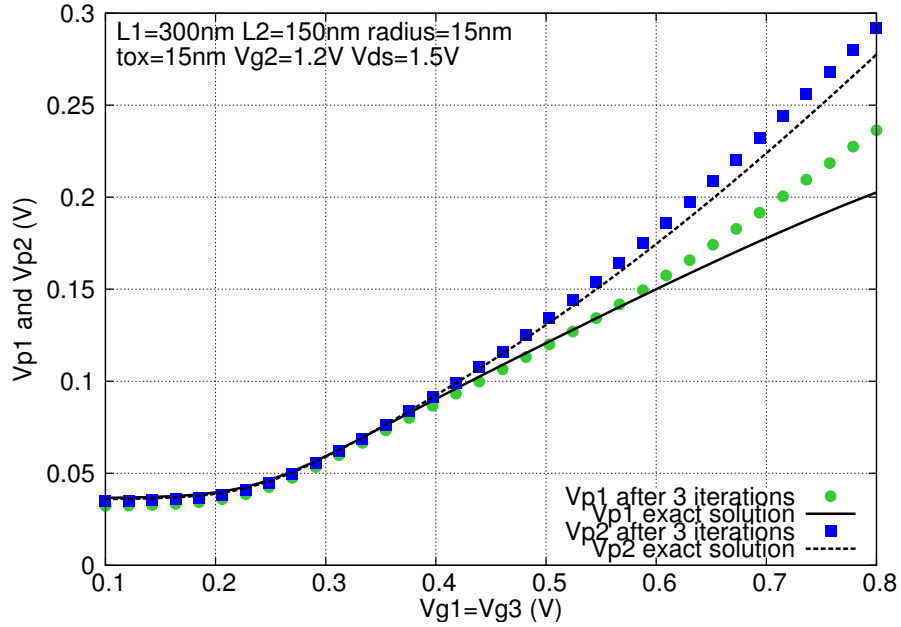


Figure 4.10. Comparison of values of V_{p1} and V_{p2} obtained from the model after three iterations with exact results in a triple structure with $V_{g1} = V_{g3}$, $V_{g2} = 1.2\text{V}$.

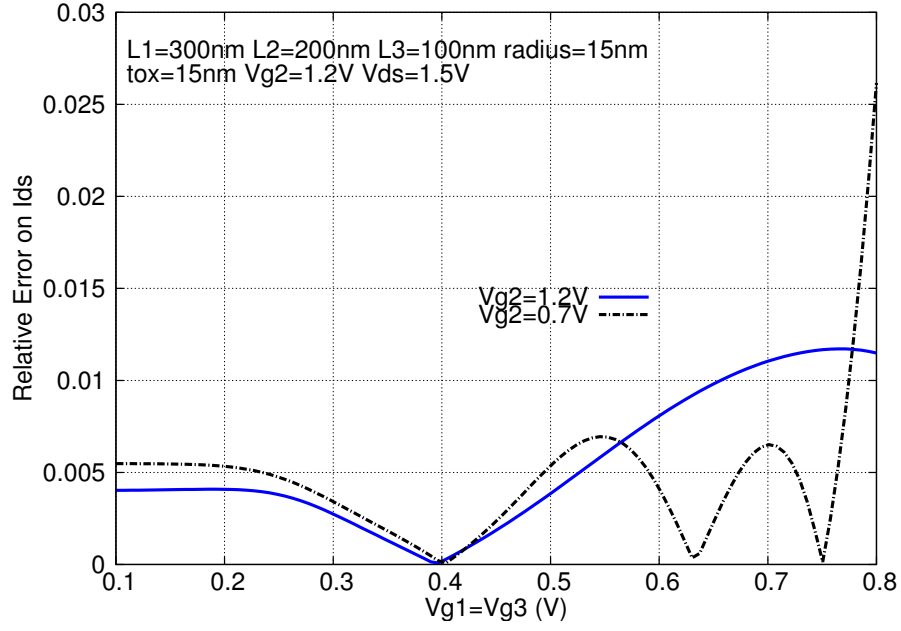


Figure 4.11. Relative errors on I_{DS} in a three-section structure where $V_{g1} = V_{g3}$ for two different values of V_{g2} .

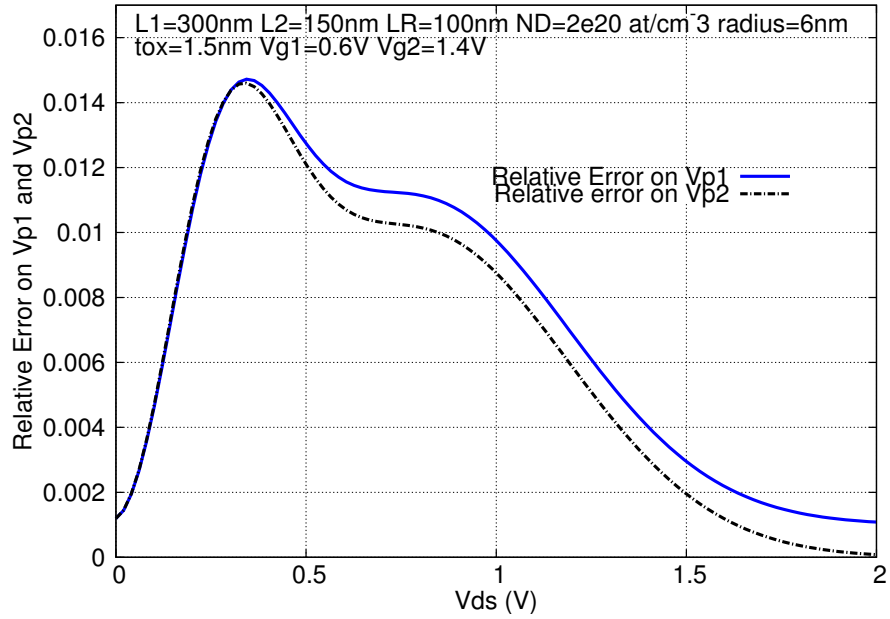


Figure 4.12. Relative errors on V_{p1} and V_{p2} in a three-section structure with a gateless section with parameters $N_D = 2 \cdot 10^{20} \text{ cm}^{-3}$, $L_R = 100 \text{ nm}$.

4.7 Discussions

Overall, our results indicate that the proposed methodology suits the need for versatile, accurate and scalable modeling of MIG devices. Tests were performed by varying the structural aspects of devices as well as the biasing conditions (see Fig. 4.1 to Fig. 4.7) over large ranges of parameters (e.g., $50nm$ to $400nm$ for section length, $0V$ to $2V$ for potentials). Versatility was also demonstrated by simulating structures made of up to nine sections, each section potentially differing from its neighborhood in different respects (length, diameter, etc...), as previously described. Efficiency was shown both in terms of computation time required and in scalability, due to the linear dependence of computation time on the number of sections, irrespectively of the targeted accuracy (see Fig. 4.13). In addition, note that the measured performance is underestimated, because an interpreted language has been used to implement equations to speed up development and to focus on accuracy rather than focusing on performances.

According to the performed analyses, and in particular those in Fig. 4.12, we conclude that relative errors on potentials are always below 2% in the measurement range. Results for current show analogous behavior, with only slightly degraded performance (4% maximum relative error) for a three sections structure.

Therefore, it follows that the proposed methodology is well suited to be applied in circuit simulators where efficiency and scalability are key enabling features.

4.8 Conclusion

This section concludes our contribution in modelling of MIG transistors. In particular, we presented a new iteration-based analytical model suitable to analyze complex semiconductor structures with several cascaded devices. Based on the computation of charge densities and potentials along the structure, it presents a high degree of versatility: we illustrated its application to a series of two or more Gate-All-Around MOSFETs. Nevertheless, no constraint actually holds on the topology and features of the sections in the structure. FinFETs-based structures can easily be analyzed through the methodology presented only with the modification of the analytical expressions for charge and currents in each section. Besides, generalizations of the method have been discussed and the inclusion of gate-less sections with description of quantum mechanical (QME) and short-channel effects (SCE) has been presented. The method has an iterative nature, although only few numerical steps are necessary to compute potentials and currents in the structure. Computational efficiency of the method is a key feature. In particular, accuracy of 3% in potentials can be obtained for up to nine sections in linear time, after just two or three iterations, without nonlinear equations to be solved numerically.

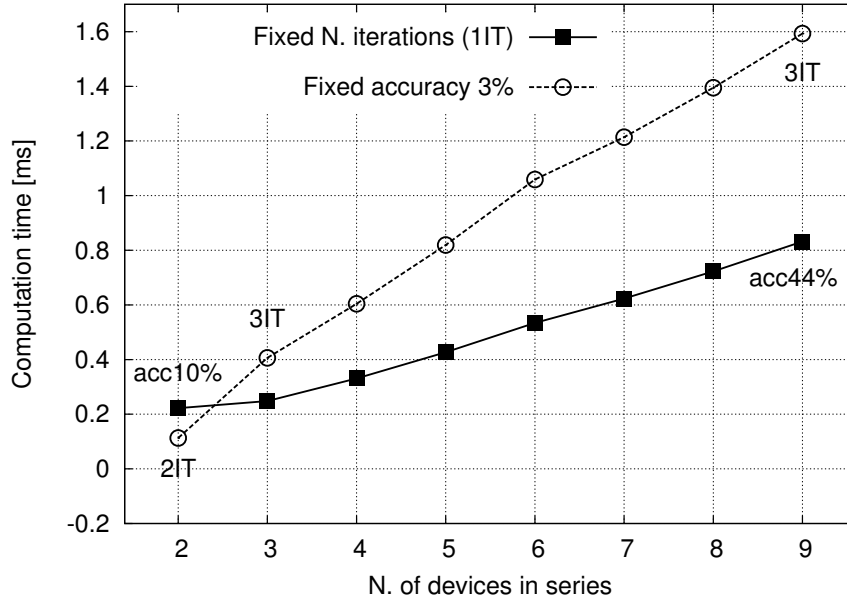


Figure 4.13. Computation times (in seconds) required to solve complex structures with different number of devices: with fixed number of iterations of our model (squares) and with the minimum number of iterations required to get an accuracy of 3% on potentials (circles).

Verification has been demonstrated through extensive simulation on devices with channel lengths ranging from 50nm to 450nm and radius larger than 1nm. The comparison of the data obtained with our model to results from commercial physics-based software reveals a good agreement. Similarly, relative errors top at 1.8 percent on potentials and about 4% on currents with respect to exact numerical solutions. The method is also timing efficient leading to accurate values of potentials in a shorter amount of time than a numerical method would require. Computation times of one order of magnitude shorter have been found, still maintaining the aforementioned accuracy and linear proportionality with the number of devices.

Part II

SiNWs for Sensing

Silicon nanowire gas sensors, which have attracted much attention in recent years are recognized to be a next generation building block for ultra-fast chemical sensing systems. In comparison with bulk silicon field transistors, the sensors made of silicon nanowires have many improved characteristics. In particular, (i) nanowire gas sensors based on silicon would be readily integrated with sophisticated CMOS integrated circuits that enable direct electrical detection without time-consuming labeling chemistry. Moreover, (ii) they showed high surface-to-volume ratio and consequent ultra-sensitivity. Due to their small size, few gas molecules are sufficient to change the electrical properties of the sensing elements. This allows the detection of a very low concentration of gas within several seconds. Not secondarily, (iv) silicon nanowire-based sensors exhibit high chemical reactivity at room temperature. These characteristics for gas sensing suggest that silicon nanowire devices could revolutionize many aspects of sensing and detection in biology, medicine, and chemistry.

Among the many intriguing properties of silicon nanowires, high surface-to-volume ratio stands as one of the most relevant. In this respect, Porous Silicon (PS) has emerged as a very promising alternative to crystalline silicon in sensing technology. Thanks to the irregular microscopic structure of this material, the surface-to-volume ratio is dramatically increased largely improving the potentiality with respect to crystalline silicon. We devote the next part of this thesis work to Porous Silicon. Specifically, in the next chapters we will describe the fabrication technology we used to fabricate our Porous Silicon Nanowires. Subsequently we will face the problem of modelling of Porous Silicon Nanowires: two models will be presented and discussed which, differing in the regime of validity and theoretical framework, are capable of describing the transport properties in PS-Nanowires. Their technicalities and results will be described in details in the following chapters.

SINWs for COMPUTATION

**Multiple Independent-Gate
Transistors:**
Modelling & Simulation

SINWs for SENSING

Porous Silicon NWs:
Fabrication & Modelling

Surface Interaction:
Ab-initio & Macroscopic
simulations

Chapter 5

Porous Silicon

5.1 Introduction

Porous silicon (PS) is a material obtained via anodic dissolution of silicon in HF solutions. Since the first report of PS formation in the 1950s, several studies have been conducted, particularly after 1990 when luminescence of PS was discovered. The findings revealed that PS has extremely rich morphological features with very different properties from those of silicon. Moreover, the formation process of PS is a very complex function of many factors such as HF concentration, type of silicon, current density, and illumination intensity. In literature a large amount of data on PS is available and, since it is not possible to cover all aspects of PS in one chapter, we will focus here on the phenomena related to the properties of silicon: the formation of PS and the resulting morphology.

5.2 Morphology

The so-called morphology, determined by the distribution of materials in space, is a very difficult quantity to describe. Indeed, to characterize morphology of PS represents a very hard task due to its rich details with respect to the range of variations in pore size, shape, orientation, branch, interconnection, and distribution. Qualitatively, the morphological features of PS present in the literature can be summarized by Fig. 5.1. Six different aspects are taken into account: pore shape, pore orientation, shape of a pore bottom, fill of macropores, branching, and depth variation of a PS layer.

As it will become clear from the description of the fabrication process of PS Nanowires, the morphology of PS is determined by all factors involved in anodization, particularly the factors related to the substrate. For example, doping concentration, which does not impact the nature of electrochemical reactions, largely

determines the morphology of PS.

Hence, the morphology of PS can be classified according to the type and concentration of doping, into four main categories: (1) moderately doped p-Si ($10^{15} - 10^{18} \text{at/cm}^3$) (2) highly doped p-Si ($> 10^{18} \text{at/cm}^3$) and (3) n-Si and (4) lowly doped ($< 10^{18} \text{at/cm}^3$). The PS formed on moderately doped p-Si has extremely small pores ranging typically from 1 to 10 nm. The pores are highly interconnected as illustrated in Fig. 5.1(5f). For heavily doped p and n types, the pores have diameters typically ranging from 10 to 100nm. The pores show clear orientation and are less interconnected as illustrated in Fig. 5.1(5e). For n-Si, the pores, with a wide range of diameters from 10 nm to are generally straight and clearly separated as shown in Fig. 5.1(5a-d). For lowly doped p-Si, the PS can have two distinctive and continuous pore diameter distributions: large pores on the order of micrometers and small pores on the order of nanometers as shown in Fig. 5.1(6c). The large pores can be fully or partially filled by the small pores as shown in Fig. 5.1(4a-c).

The morphology of the PS formed on n-Si also strongly depends on illumination conditions, that is, intensity, frequency, and direction (front or back). Very different morphologies are produced by front versus back illumination. Back illumination generally produces straight pores, whereas front illumination typically produces a two-layer PS as shown Fig. 5.1(6c).

Among the morphological features, the average pore diameter of a PS, as a quantifiable and easily measurable parameter, is most commonly determined. Pores can be classified as micropore if the pore diameter is less than 2 nm, as mesopore if it is between 2 and 50 nm, and as macropore if it is larger than 50nm. For simplicity, the pores discussed in this thesis are categorized as only micropores (less than 10nm).

5.3 Fabrication

A proposed methodology of fabrication that presents clear advantages in terms of costs, size control (shape, geometrical dimensions) and typology (doping type and level) is Metal-Assisted Etching (Ma-E) [82]. The SiNWS synthesized by this approach are virtually aligned across large areas up to wafer-scale. Moreover, Ma-E can be used both in presence of a quasi-continuous metal film or a patterned one. This yields ordered arrays of nanowires with diameter defined by the initial sphere size. Most interestingly, Ma-E results in the formation of pores in the etched structures due to holes diffusion [111].

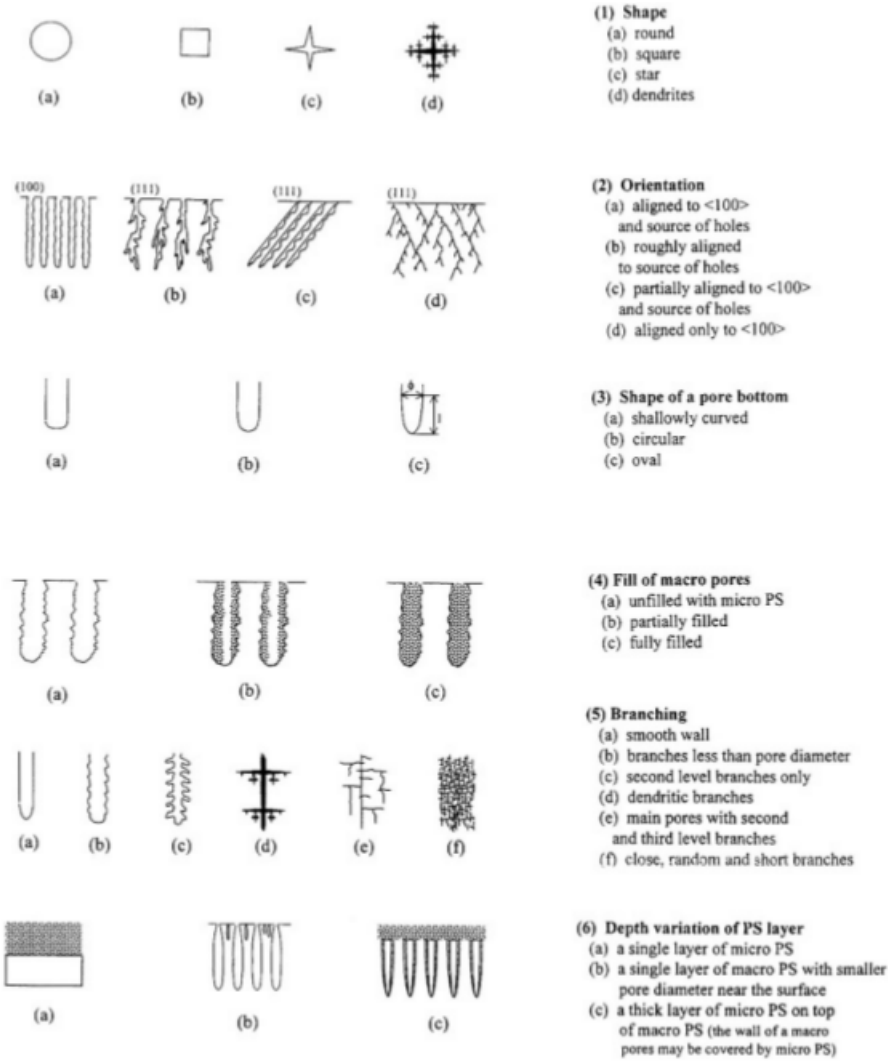


Figure 5.1. Schematic illustration of morphological features of PS. From [88]

5.3.1 Introduction

First studies on Metal-Assisted Etching of Silicon were reported in 1997. Porous Silicon was fabricated by etching a Si substrate with Aluminium in a solution composed of HF , H_2O and HNO_3 . In that first experimental setup, the necessary time to etch Silicon was significantly decreased due to the presence of Al catalyst film on the surface of the Si substrate. In a typical metal-assisted etching process, a Si substrate is partly covered by a noble metal and it is subjected to an etchant composed of HF and an oxidizing agent, typically hydrogen peroxide (H_2O_2). Si

underneath the noble metal is etched much faster than the Si portion without noble metal coverage. As a result, the noble metal digs the Si substrate, generating pores in the Si substrate or, as a side effect, Si wires. Fig.5.2 shows the described process.

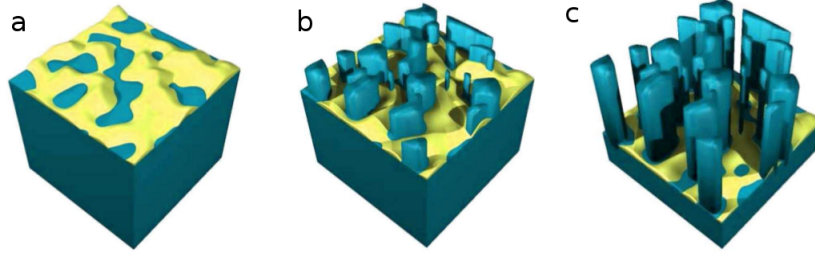
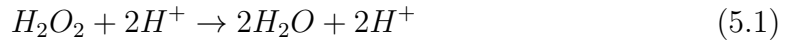


Figure 5.2. a) Silicon is partly covered with noble metal; b) After the dip in the MaE solution, metal sinks in the substrate; c) At the end of the etching, Si structures remain: memory of the metal layer morphology.

Various possible anode and cathode reactions have been suggested to describe the metal-assisted etching analogous to the anodic etching of Si in HF or stain etching of Si in HF/HNO_3 . However, there is a general agreement on the fact that H_2O_2 is reduced at the metal (cathode reaction):



Li and Bohm [111] and Harada [86] proposed that the reduction of protons into hydrogen was another cathode reaction in addition to the reaction above (5.1):



On the contrary, Chartier et al. [87] assert that the gas evolution during the etching is due to an anode reaction. The conclusion of this study came from the hypothesis that H_2O_2 instead of H^+ is the principal reaction agent at the cathodic sites, because in an HF solution without O_2 and H_2O_2 , the Si substrate covered with metal is not etched. At the same time, the possibility that the gas generated from a decay of H_2O_2 was excluded because gas evolution did not occur on a metal particle over Si substrate in solution in the absence of HF. At the anode, the Si substrate is oxidized and dissolved.

5.3.2 The Overall Etching Process

Based on the previous results, five steps can roughly describe the process in metal-assisted etching (fig. 5.3):

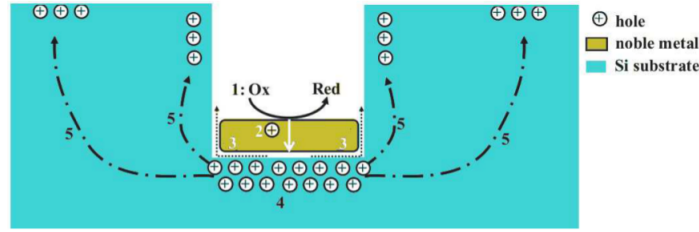


Figure 5.3. Scheme of the processes involved in metal-assisted chemical etching. Numbers indicate the steps introduced in section 5.3.2

- The oxidant is preferentially reduced at the surface of the noble metal due to the catalytic activity of the noble metal on the reduction of the oxidant.
- The holes generated due to the reduction of the oxidant diffuse through the noble metal and are injected into the Si that is in contact with the noble metal.
- The Si is oxidized by the injected holes and dissolved at the Si/metal interface by HF. The reactant (HF) and the byproducts diffuse along the interface between Si and the noble metal.
- The concentration of holes has its maximum at the Si/metal interface. Therefore, Si which is in contact with the metal is etched much faster by HF than a bare Si surface without metal coverage.
- The holes diffuse from the Si under the noble metal to off-metal areas or to the wall of the pore if the rate of the hole consumption at the Si/metal interface is smaller than the rate of the hole injection.

Therefore, the off-metal areas or sidewalls of the pore may be etched and form microporous silicon, analogous to the case of the electrochemical stain etching. An example of this phenomenon is shown in fig. 5.4.

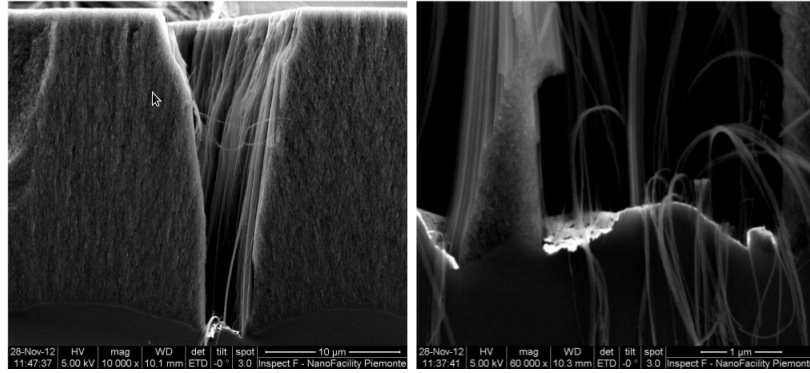


Figure 5.4. Section of a Si p^+ sample after 5 minutes of MaE. It is possible to see the porous silicon due to the hole diffusion where the metal did not sink into the substrate.

Chapter 6

Fabrication of PSNWs

In this section we will describe the process exploited for the fabrication of silicon nanowires. Based on the Metal-Assisted Chemical Etching approach, to which we devoted our discussion in the previous chapter, the details of the process will be given and the images of the resulting devices presented. We conclude the chapter with the analysis conducted through Transmission Electron Microscopy that we performed on the wires we fabricated.

6.0.1 Metal and deposition technique tests

Sputtering is a Physical-Vapour Deposition (PVD) process involving the removal of material from a target, in our case a clean solid cathode (fig. 6.1) [128, 129, 130].

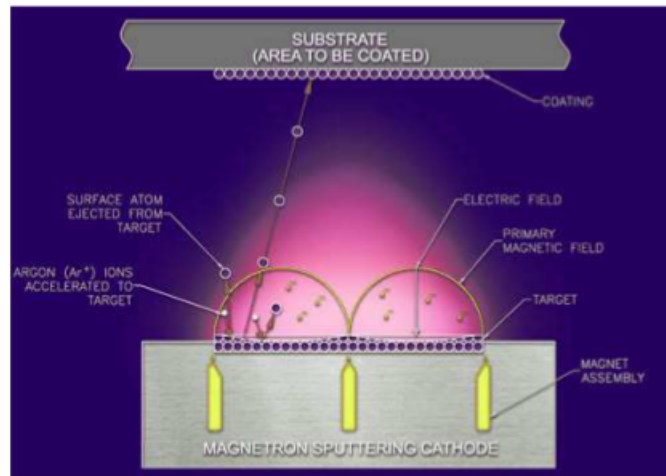


Figure 6.1. Sketch of a plasma sputtering process.

This is fulfilled by bombarding the target with positive ions emitted from a noble gas discharge. When ions with high kinetic energy engrave the cathode (they are accelerated by an electric field), the consequent collisions remove, or sputter, atoms from the material. Transferring kinetic energy from impacting ions to surface atoms is the basis of sputter coating. Emitted atoms thicken onto a substrate forming a film of the same material of the target. To accomplish physical sputtering, electrons would need very high kinetic energies (at least several hundreds of keV), since the energy transfer between the light e^- and the heavy atoms is very inefficient. Therefore, ions are commonly used for this purpose because they can be accelerated using electric fields unlike neutral atoms. The useful range for sputter deposition is considered to be above the threshold of 5keV; sputtering is a rather inefficient process where 95% of energy is dissipated as target heat. Nowadays, sputtering has developed into a versatile deposition technique that could deposit most materials. A vacuum chamber, a sputter source, vacuum sensors, a substrate holder and a pumping system are components of a typical sputter deposition system. Rare gas is ionized using large potentials at the source, resulting in the generation of a plasma and deposition from a target material onto the substrate and chamber walls.

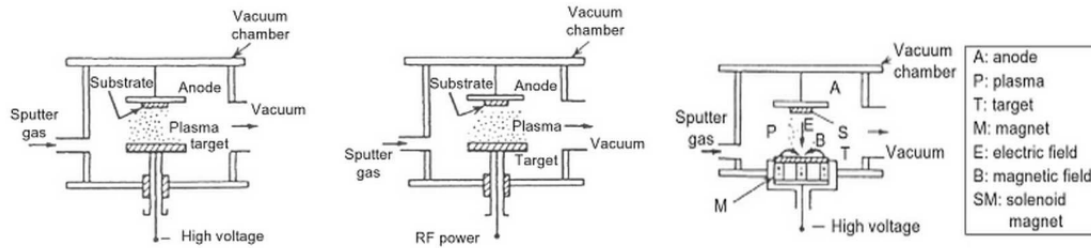


Figure 6.2. a) DC diodes; b) RF diodes; c) Magnetron

Figure 6.3. Basic Configuration of sputtering systems (from [130])

The two most common typologies of sputter sources are diodes (fig. 6.2-a and 6.2-b) and magnetrons (fig. 6.2-c). These configurations can be operated with direct current (DC) or radio frequency (RF) potentials to generate a plasma through the ionization of noble gas. An external potential is applied from an outside power source, charging the target to a high negative voltage (3 to 5kV). A rare gas, usually Argon, is introduced into the vacuum chamber between the target and the grounded substrate and chamber walls. The large difference in potential forms a plasma, caused by ionization of the Ar atoms (Ar^+). This ionization results in a negatively charged electron and positively charged ion pair, instead of the plasma that retains a neutral charge. Positively charged ions are attracted and accelerated

by the electric field, resulting in a collision with the target material. Bombardment of the target with these high-energy ions leads to sputtering of the target atoms, forming a coating on the substrate and the chamber walls. In this type of configuration, the target and the substrate holder can be considered a parallel plate capacitor. A drawback of this typology of sputtering system is the low efficiency.

Magnetron sources overcome the limitations of the diode sources by using a magnetron field to control the motion of electrons. Magnetron sources use the properties defined in this physical law to control the electrons generated in the plasma and apply them toward a plasma regeneration. The key difference between a planar magnetron source and a diode one is that a permanent magnet is placed behind the target. The resulting magnetic field confines the electrons to a circular path on the surface of the target disk. These energized electrons further ionize the gas molecules through collision, resulting in a large increase in plasma density at the target surface and increase from the target, with reduced irradiation of the substrate and chamber walls. Because the sputtered target atoms are relatively massive and neutrally charged, they are not affected by the magnetic field and they migrate to coat the substrate and exposed chamber surfaces. The key advantages of this type of source include a vast improvement in efficiency compared to the diode source, sputter deposition rate is improved because of the increased plasma density.

In our experimental setup, a target of gold palladium (Au/Pd 68/32 wt %) is mounted in a Cressington Sputter Coater 108auto sputter system. The thickness of the metal was measured by profiling.

6.0.2 Gold (Au) - thermal and e-beam evaporator

Evaporation deposition Evaporation is an ordinary method of thin-film deposition; source material is evaporated in vacuum. Vacuum allows vapour particles to go through directly to the substrate, where they recondense in a solid state. Evaporation is commonly used in a microfabrication; the coatings, also called films, are usually in the thickness range of angstroms to microns and can be a single material or can be multiple materials in a layered structure. The object to be covered by the material evaporated can be any of a wide variety of things such as: semiconductor wafers, solar cells, optical components, etc... Thermal Evaporation involves heating a solid material inside a high vacuum chamber, taking it to a temperature which produces its vapour pressure. In vacuum, even a relatively low-vapour pressure is sufficient to raise a vapour cloud inside the chamber. This evaporated material at this point constitutes a vapour stream, which crosses the chamber and hits the substrate, sticking to it as a coating.

There are two methods of heating the source material. One of these, often referred to as filament evaporation, is a simple electrical resistive heat element, or

filament that exploits Joule effect. The filament source offers the safety of low voltage, although very high current is required, usually several hundreds amps.

The other common method to heat the material is to use an electron beam, or e-beam; this is generally known as e-beam evaporation. This is a more "high-tech" approach to heat up a material and involves some high voltage (usually of the order of 10kV), so e-beam systems always include extra safety features. The source itself is an e-beam gun, where a small and very hot filament boils off electrons which are then accelerated by the high-voltage, forming an electron beam with high energy. At the standard 10kV, even 0.1A of this beam current will deliver 1kW of concentrated power and this heats the material, which is contained in a hearth which is water cooled to prevent its destruction. Examples of the structures obtained with the described deposition techniques of gold on silicon substrate are shown in fig.6.4. After the Metal-assisted etching procedure the structures look very different; in particular, the e-gun evaporated approach produces nanowires with the same length, very similar in diameter and well distributed over the sample (fig. 6.5).

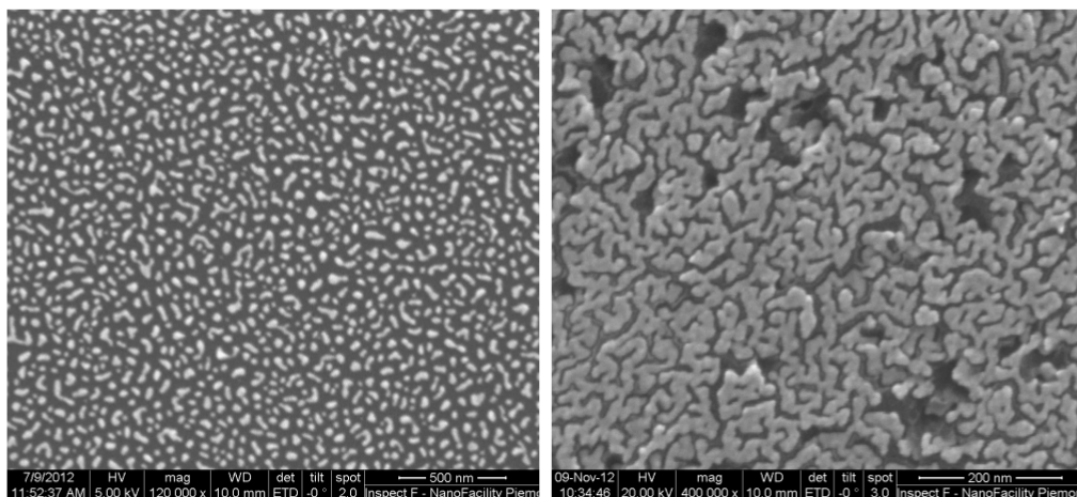


Figure 6.4. Comparison between 10nm gold layer deposited by thermal and e-beam evaporator. a) Thermal evaporator; b) e-gun evaporator.

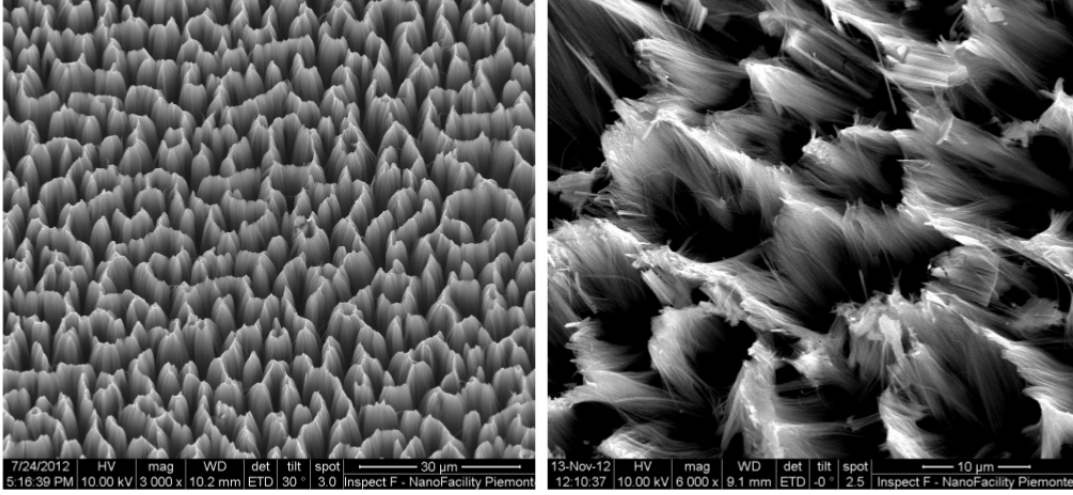


Figure 6.5. Comparison between 3 min MaE etch on a sample covered with gold deposited by thermal and e-beam evaporator. a) Thermal evaporator; b) e-gun evaporator.

6.1 Ordered sample

From the images shown, it is clear that it is practically impossible to pick silicon nanowires with similar geometrical features from the multitude of fabricated nanowires. To overcome this problem, it is necessary to pattern the metal deposition creating a mask that makes holes in a continuous metal layer; a proposed solution is to use polystyrene (PS) nanospheres. These nanospheres are fabricated in many different dimensions, from 80nm to 500nm and beyond. To prepare the silicon substrate for the nanosphere deposition, it was dipped in Piranha solution ($H_2SO_4 : H_2O_2, 3 : 1$) at $80^\circ C$ for one hour. Since the mixture is a strong oxidizing agent, it removes most organic matter and it also hydroxylates surfaces (adds OH groups), thus making them highly hydrophilic. Polystyrene nanospheres with diameter of $180nm \pm 5\%$ in aqueous solution at 10% in weight were spread on the silicon substrate by spin-coating in order to obtain a self-assembled monolayer packed into the hexagonal closed packed planar structure. Initial acceleration and rotation speed play a fundamental role in the success of the process. In our case, we used a combination of two steps: in the first 10s the sample rotates at 500 rpm reaching this speed in 1s; after that, 30s 350 rpm with maximum acceleration allowed (1066 rpm/s). Phase one is used to eliminate the dilution water from the substrate surface; in the second part, nanospheres organize themselves. A portion of silicon substrate covered by the monolayer can be seen in fig. 6.6-a.

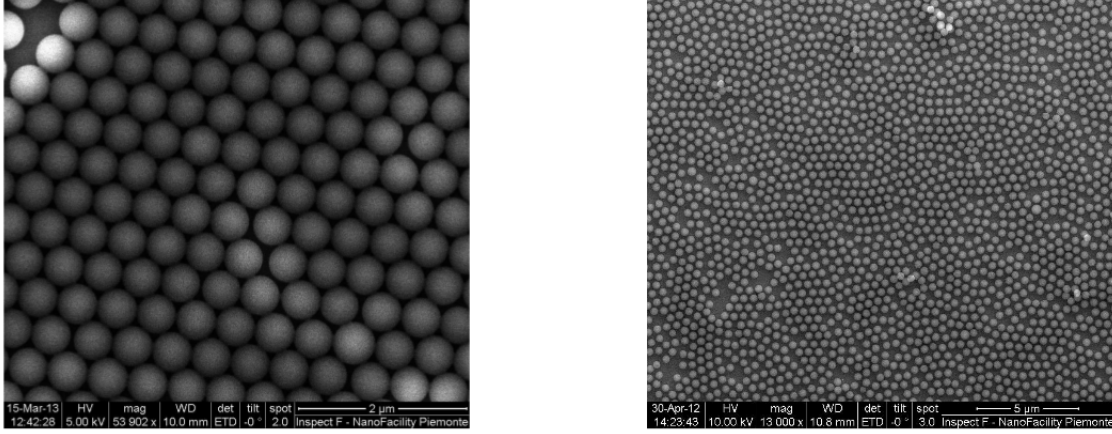


Figure 6.6. SEM images of the fabrication process of nanowires using polystyrene nanospheres to pattern the metal deposition. a) PS spheres are spun over the Si sample. b) $O_2 : Ar$ plasma etch is performed.

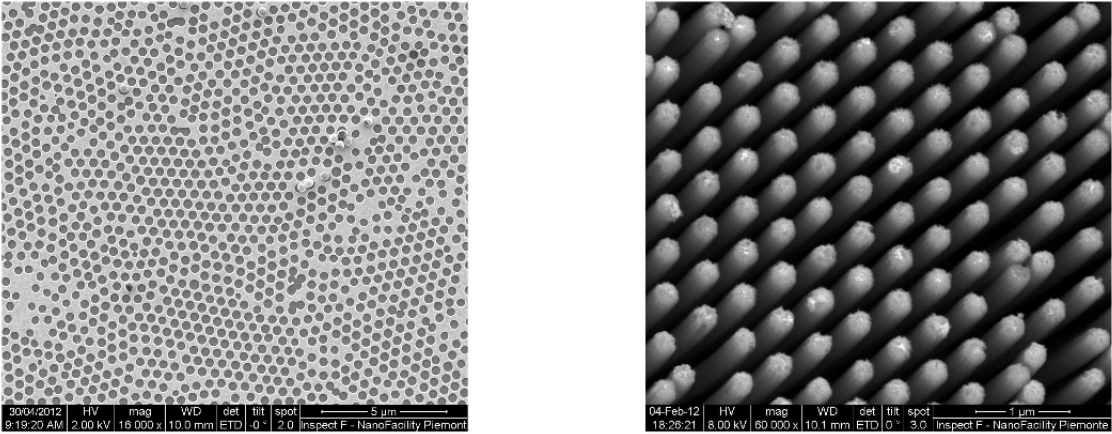


Figure 6.7. SEM images of the fabrication process of nanowires using polystyrene nanospheres to pattern the metal deposition. c) Gold layer is deposited and spheres are removed. d) Nanowires are fabricated by MaE.

A 2 min oxygen and argon plasma etching (100W) was performed in order to reduce their dimension down to 110/120nm.

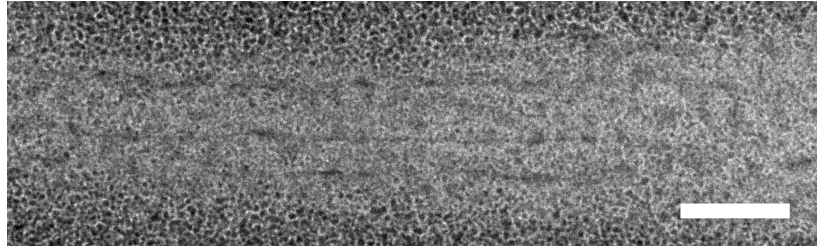
At this stage, a 20nm thick gold film was deposited on the sample using an e-beam evaporator. A so-called "antidot" metal pattern remained on the silicon surface after the spheres removal in ultrasonic bath. In fig.6.6-b and 6.7-c the reduced spheres and the metal pattern after the spheres removal are shown. Metal-Assisted Etching was performed dipping the sample in the chemical solution composed of deionized water,

6.2 TEM Analysis

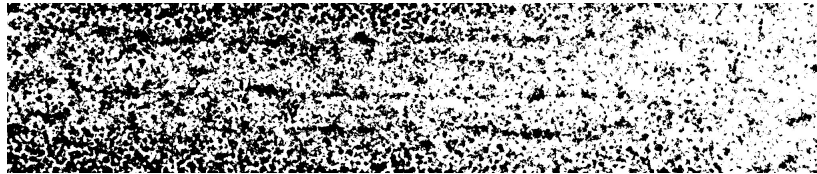
As discussed in the previous sections, the devices resulting via the Metal-Assisted Etching process are Si nanowires characterized by a an irregular microscopic structure in which crystalline regions are immersed in a network of amorphous material of Silicon and oxide. Differently stated, the nanowires have a porous structure which largely affects their transport properties.

The first step in our modelling procedure of porous silicon begins with an analysis of the fabricated devices: their microscopic structure is observed and the average geometrical properties are extracted. Given the complicated structure of each single device, whose atomistic configuration is made of millions of atoms, and given the actual impossibility to control the wires' properties through a manipulation of the process parameters, a statistical approach represents the only viable methodology for a correct description of the problem. Moreover, it has been verified experimentally how a direct correspondence exists between, for example, the HF concentration and the resulting average porosity of the wires. As a consequence, a statistical approach will allow a simple and efficient connection between the physical real devices and the parameters' reduction which is always implied in the following modelling process.

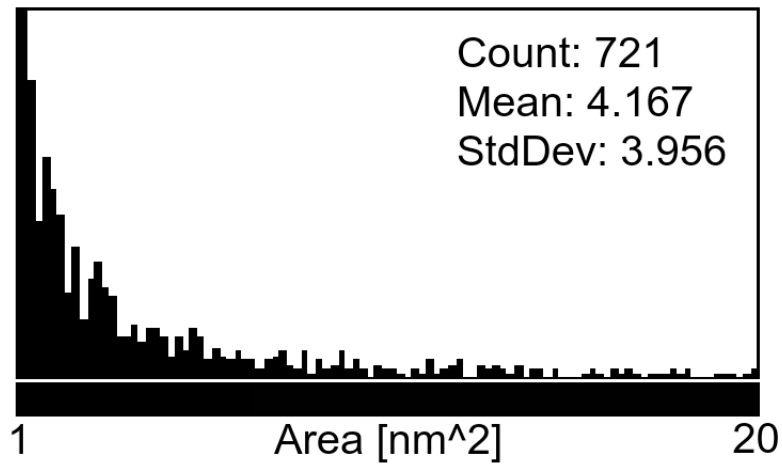
In order to extract information on the fabricate devices, Transmission Electron Microscopy (TEM) was performed after having scratched the NWs on a TEM grid. Hence, their structural properties could be investigated and extrapolated data have been used as a starting point for subsequent simulations. Fig. 6.9-a shows the internal structure of a NW: darker dots are nanocrystals of silicon immersed in a porous structure. Using ImageJ software it has been possible to locate the nanocrystals exactly and, consequently to statistically evaluate mean and distributions of their geometrical properties. Starting from these images, a binary (b/w) copy is generated (fig. 6.9-b) and a graph of the area distribution can be plotted, like in fig. 6.9-c. According to the results in the picture nanocrystals have an average area of $4.1nm^2$.



(a) TEM image of a single Si NW (marker: 50 nm)



(b) ImageJ b/w conversion



(c) Area distribution of Si nanocrystals

Figure 6.9. TEM image analisys

Chapter 7

PS model

In this chapter we describe the procedure we followed to construct a simple model for a porous silicon nanowire; this model is suitable for numerical analysis in the physics-based software TCAD Atlas [127]. This physics-based software allows easily to describe complex geometrical semiconducting structure and to analyse their relevant electrical quantities solving self-consistently different sets of equations for modelling electron transport. The software will allow to conduct the electrical characterization of a PS-NW: as a consequence, data on the main electrical quantities of the material can be obtained together with their dependence on physical and geometrical parameters.

As it is evident from Fig. 7.1, representing the results of elaboration of an image of the fabricated nanowires, silicon nanocrystals are immersed among non-crystalline regions forming an irregularly networked pore structure.

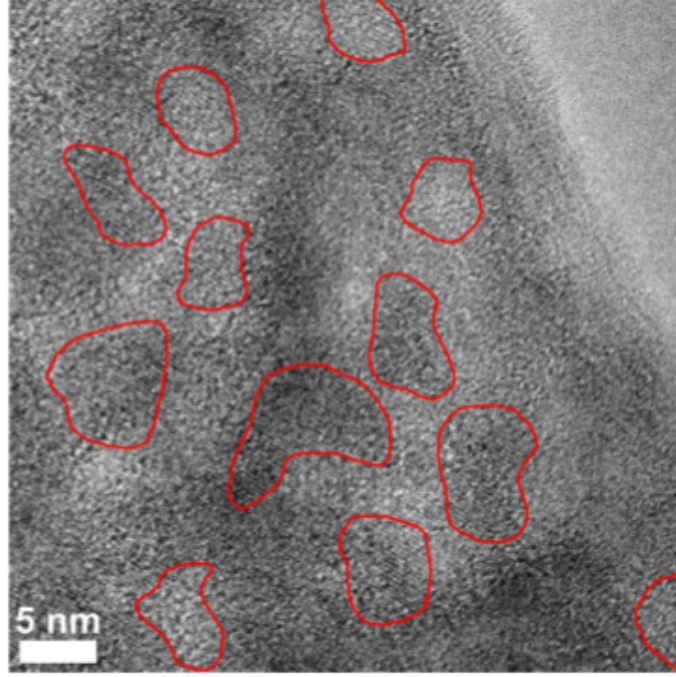


Figure 7.1. Transmission Electron Microscope Image of silicon nanowire.

The model we describe here is intended to be a simulative model. The simulative approach seems to be the most promising way to tackle the problem of modelling PS nanowires. The uniform distribution of the pores along the channel and the statistics of their geometrical properties make an analytical treatment of the electrical problem rather impractical.

Moreover, at the best of authors' knowledge, no models are present in physical simulators for porous materials, nor physical data are present to describe their electrical properties (mobility, energy gap, dielectric constant,...); the reason for this being the unavoidable dependence of the electrical parameters of the materials from the dimensions of the pores and from their effective shape.

In order for it to be effective, a physical model of these devices is strongly required.

The chapter is structured as follows. In the next section we give a description of the structural model of PS nanowire as implemented in the simulator while the transport models adopted to analyse the electrical quantities and the numerical parameters are the focus of the following sections. Finally, the last section is devoted to the presentation and discussion of the simulation results.

7.1 PS-NW model

7.1.1 Structural model

We modelled a PS-NW as a 3D-wire with square section composed of p-doped crystalline silicon ($N_A = 10^{15}$ atoms/cm³). Its lateral surfaces are drilled through slit pore segments randomly arranged and filled with air. These pores have a squared section; their number, depth and position are randomly chosen according to the geometrical properties of our fabricated devices in a way which will be explained in the following. An image of a silicon nanowire with this structure is shown in Fig. 7.2.

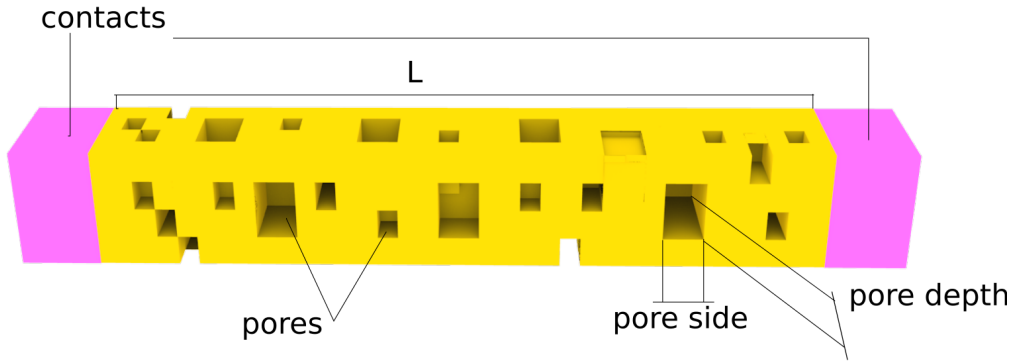


Figure 7.2. Geometry of a Porous Silicon Nanowire as adopted in the model described: pores dipping on the surface of silicon crystalline silicon.

This is the simplest model of a pore in a PS-NW (see fig. 7.3-a): air has been inserted in the volume created from the slits. However, in general, non-crystalline silicon and/or gas fill that space, thus changing the electrical conductivity of the whole device. To keep things treatable by Silvaco Atlas software, air is actually the proper choice. Secondly, this allowed us to focus attention on the dependence of

the nanowire resistivity from the physical parameters of the device. It is worthy to be mentioned that the peculiar geometry chosen for the pores does not restrict the range of devices to be simulated and subsequently does not limit the validity of the obtained results. In fact, we left the pores the possibility to spatially overlap and intersect each other so that ramified porous entities can arise thus making the pores' geometry rather arbitrary. Fig. 7.3-b shows some examples of more complex pores which could arise from the intersection of square-section pores.

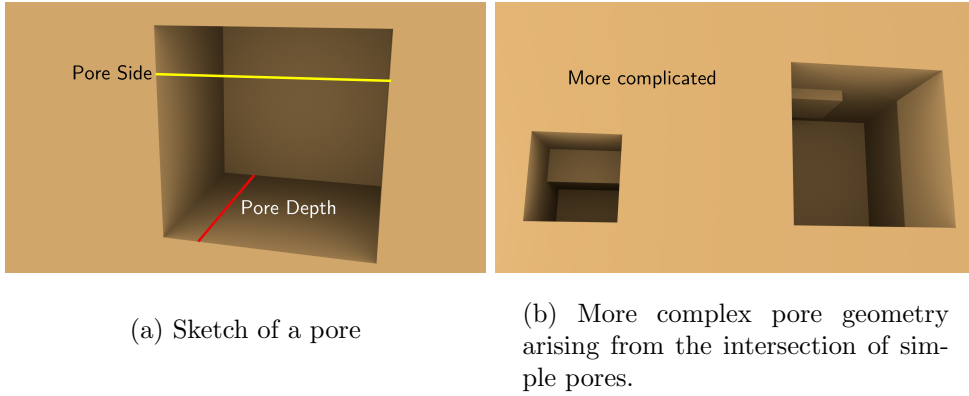


Figure 7.3. Examples of pores geometry.

The contacts have been chosen to be non-rectifying metal contacts in order not to include the effects of the Schottky contacts in the transport process. We have described the structure of the PS-NW in Atlas software by means of a rectangular mesh, denser in correspondence of the interfaces between different materials (silicon-air/metal) and sparser elsewhere. This guarantees a faster convergence of the numerical method implemented in the nodes of the grid. The image of a mesh as described in Atlas is depicted in fig.7.4.

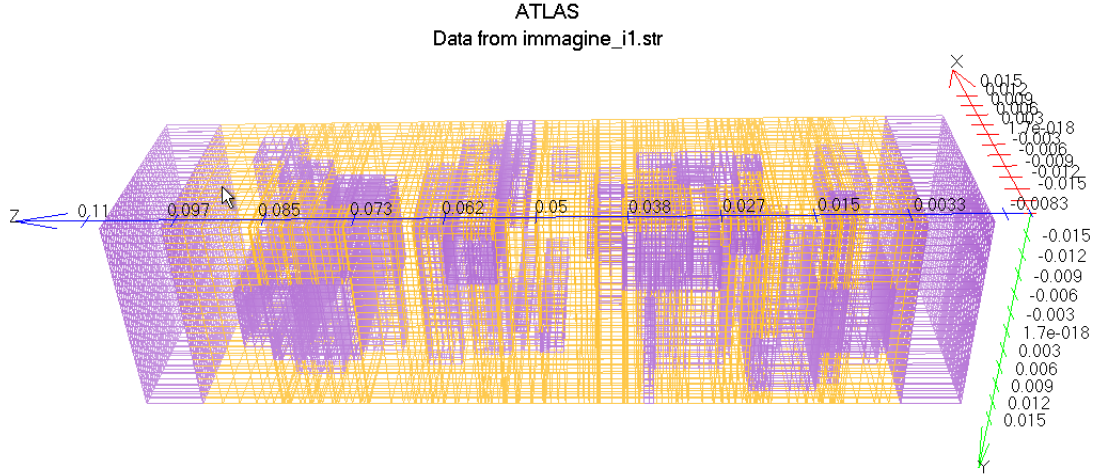


Figure 7.4. Atlas mesh of a PS NW (pores are coloured in purple).

7.1.2 Transport Model

The analysis of the transport properties in the structure of Porous Silicon Nanowires just described requires the implementation of a set of equations, which, solved self-consistently on the grid of points of fig. 7.4, allow to determine the relevant electrical quantities in the semiconducting structure.

Since the geometrical dimensions of the wires considered are in the range of hundreds of nanometers of length and tenths of nanometers in the cross-section side, we adopted a semi-classical description of the carriers' concentration. In particular, we chose the Boltzmann distribution of the carriers in the channel. This parameter is the input of a drift-diffusion model for current and electric field. Moreover, the carriers' mobility has been chosen to depend on the local electrical field according to the model FLDMOB implemented in Silvaco Atlas. It takes into account the effect of velocity saturation of the carriers through a reduction in the effective mobility according to the Caughey and Thomas expression which provides a smooth transition between the low-field and high-field regimes ([127]). As it will become clear, non-uniformities of the electrical field in the channel are responsible for a gradual reduction of the current with the applied voltage. This mobility model coherently describes the current saturation effect in presence of non-homogeneous electrical fields.

The presence of pores with depths smaller than a 10nm actually demands for a treatment of the quantum-mechanical effects arising in the structure. Specifically, potential confinement in transverse direction is expected to play a role in the discretization of energy levels engendering a reduction of the charge density in the

channel and a consequent decrease of current flow. To take into account the quantum effects, calculations have been performed with the Quantum Bohm Potential model implemented in Atlas.

The model introduces a position dependent quantum potential Q which is added to the potential energy of a given carrier type. This quantum potential is derived using the Bohm interpretation of quantum mechanics [132] and takes the form

$$Q = -\frac{h^2}{2} \frac{\gamma \nabla(M^{-1} \nabla(n^\alpha))}{n^\alpha} \quad (7.1)$$

where γ and α are two adjustable parameters, M^{-1} is the inverse of the effective mass and n is the electron (hole) density. Q is added to the continuity equations and the self-consistent cycle is solved.

In particular, the iterative scheme used to solve the non-linear BQP equation along with a set of semi-classical equations is as follows. After an initial semi-classical solution has been obtained, the BQP equation is solved on its own Gummel iteration to give Q at every node in the device. The semi-classical potential is modified by the value of Q at every node and the set of semi-classical equations is then solved to convergence as usual (using a Newton or Block iterative scheme). Then, the BQP equation is solved to convergence again and the process is repeated until self-consistency is achieved between the solution of the BQP equation and the set of semi-classical equations.

7.1.3 Numerical Parameters

The nanowire we analysed through simulations has a channel length of $100nm$ and a squared section of $900nm^2$. In order to obtain valuable information about the fabricated nanowires, we simulated many devices whose pores present geometrical characteristics similar to those shown in fig. 7.3-b. According to the results of a statistical analysis on the actual pores, their distribution along the simulated wire is uniform while the pore depths and sides are normally distributed with average values respectively $\mu_{depth} = 19.2nm$, $\mu_{side} = 6.3nm$. The corresponding standard deviations are $\sigma_{depth} = 11.4nm$, $\sigma_{side} = 3.2nm$.

7.2 Simulation Results

Fig. 7.5 shows the current-voltage characteristics for some actual realizations of silicon nanowires: each curve corresponds to a particular device with specific distribution and properties of pores. As it is clear, the current behaviour is strongly non-linear, each curve reaching a saturation value for sufficiently high voltage applied. Specifically, in the regime of low voltage, the current in each nanowire increases

linearly with a slope which is influenced by the concentration and dimensions of the pores. A larger amount of silicon removed by the pores produces a greater differential resistivity of the device since less conductive paths are available for current. As the voltage is increased, the current rate gradually decreases. This behaviour can be justified by considering the distribution of the electrical field in the channel (Fig. 7.6): for sufficiently high voltage the electric field ceases to be uniform, becoming more intense in certain particular regions (lighter regions in the figures). There, the electric field will soon reach a value such that the mobility saturation will occur according to the transport mobility chosen. The current flow in that region will consequently be limited by the mobility of the carriers thus reducing the overall charge flow along the device. Current will continue to increase with voltage until more regions will be interested by a strong electrical field. Then the current will plateau. The voltage at which the current deviates from linearity and the saturation current are actually dependent on the specific configuration of pores along the channel.

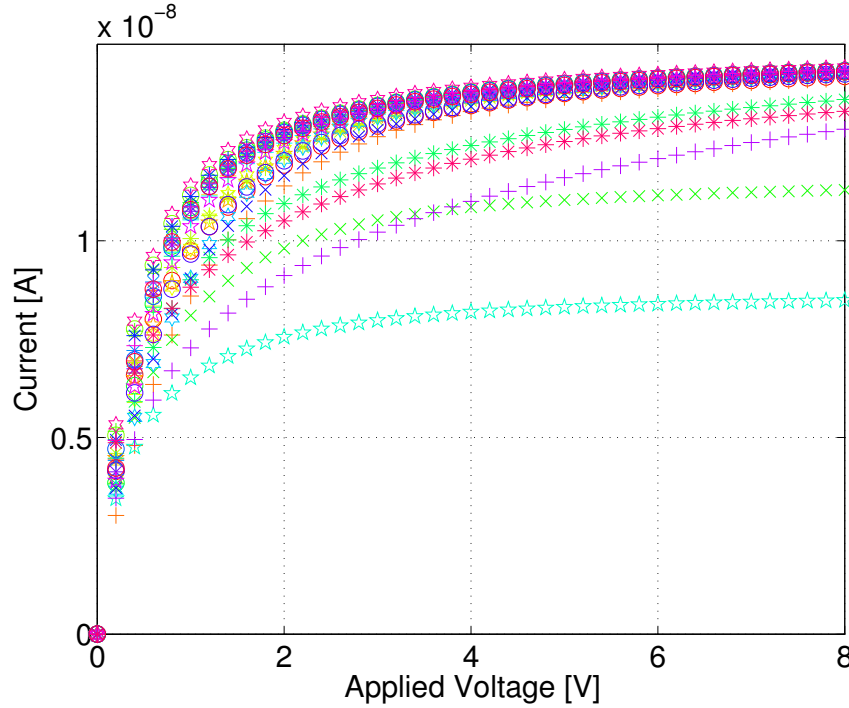


Figure 7.5. Voltage-Current characteristics of some PS-NWs having different geometrical parameters (position, depth, side). Their position along the wire is uniformly distributed, their depth and side are normally distributed.

Fig. 7.7 shows the differential resistivity of a PS-NW averaged over the ensemble of devices which have been analysed. The vertical bars in the figure represent

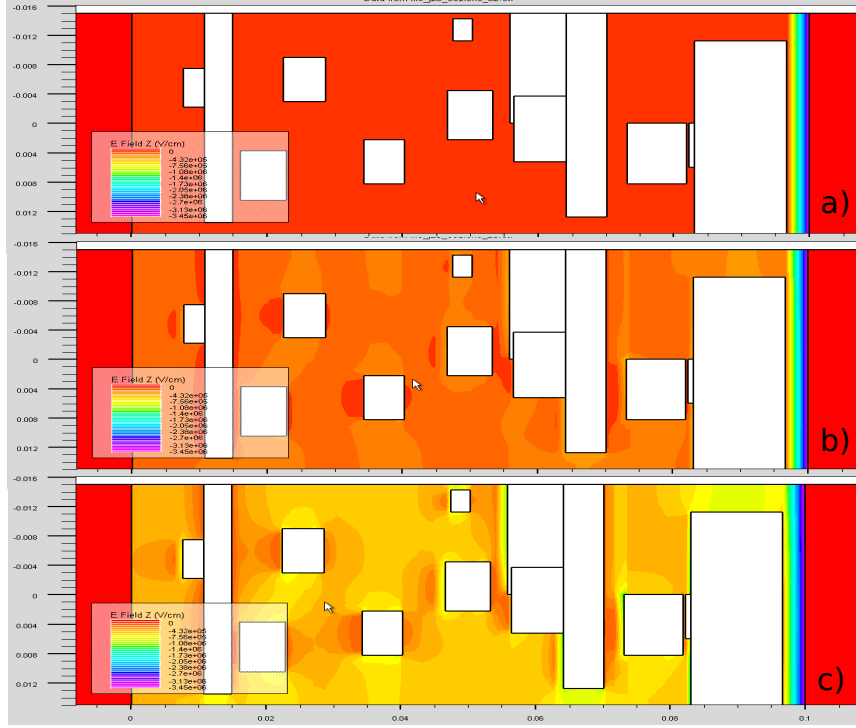


Figure 7.6. Electric field distribution in a section of a PS-NW with $L = 100nm$ and section $900nm^2$ for a) $V = 0.2V$, b) $V = 2.5V$ and c) $V = 8V$. The uniform electric field for low voltages becomes non-uniform for higher voltages provoking the velocity saturation of carriers in some channel regions. Higher voltages increases the extensions of saturated regions and total current consequently plateaus.

the standard deviation. The resistivity naturally grows with voltage, while the increment of the corresponding standard deviation can be easily explained: for high voltages, a small difference in the variation of current for two devices can result in a large difference in the differential resistivities: these consequently present a larger deviation from the average value.

We finally discuss the results of the simulation of the ensemble of different nanowires for different doping channels. Higher doping levels produce lower resistivity as shown in Fig. 7.8 where the average resistivity and its standard deviation computed at $V = 1.0V$ are depicted. Moreover, larger deviations from the average values are found for increasing doping level, due to the fact that, for fixed applied voltage, electrical field in more doped channels is higher with respect to the electrical fields in channels with lower doping. In more doped devices this reduces the carriers' mobility (increasing resistivity) counteracting the effects of the augmented concentration of carriers through doping. Doping can then be used to trim the sensitivity of the sensor, as well as applied voltage has to be carefully defined at the PS-NW sensor engineering phase. In other words, detailed data on what can be

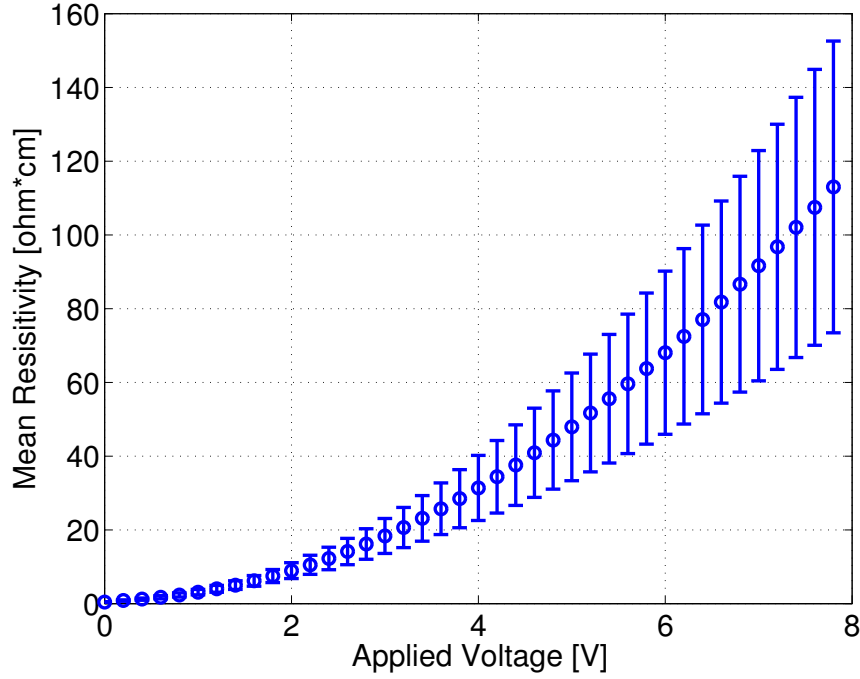


Figure 7.7. Average differential resistivity of an ensemble of PS-NWs with $L = 100nm$ and section $900nm^2$ as a function of the applied voltage. The vertical bars represent the standard deviation.

obtained are essential during a sensor design and simulation phase, thus confirming the importance of the modelling attempt presented in this work.

7.3 Conclusions

In this chapter we presented a simplified model for Porous Silicon Nanowires. Starting from a TEM analysis of our fabricated devices, we devised a simple methodology to study electron transport in highly non crystalline wires. In particular, the model is apt to be implemented in a physics-based simulator due to the strong geometrical correspondence between the crystalline and porous regions. The implementation of the model in the software TCAD Atlas allowed to understand the main physical phenomena taking place when current flows. A gradual reduction in the carrier mobility has been found as the major cause of a current plateauing for high applied voltage. In this respect, mobility decreases in correspondence of the constrictions in the wire generated by neighbouring porous areas. As a consequence, a reduction in the conductance followed.

The effects of doping analysed are fully in agreement with the classical theory of doping: an increase in conductance (reduced resistivity) has been highlighted due

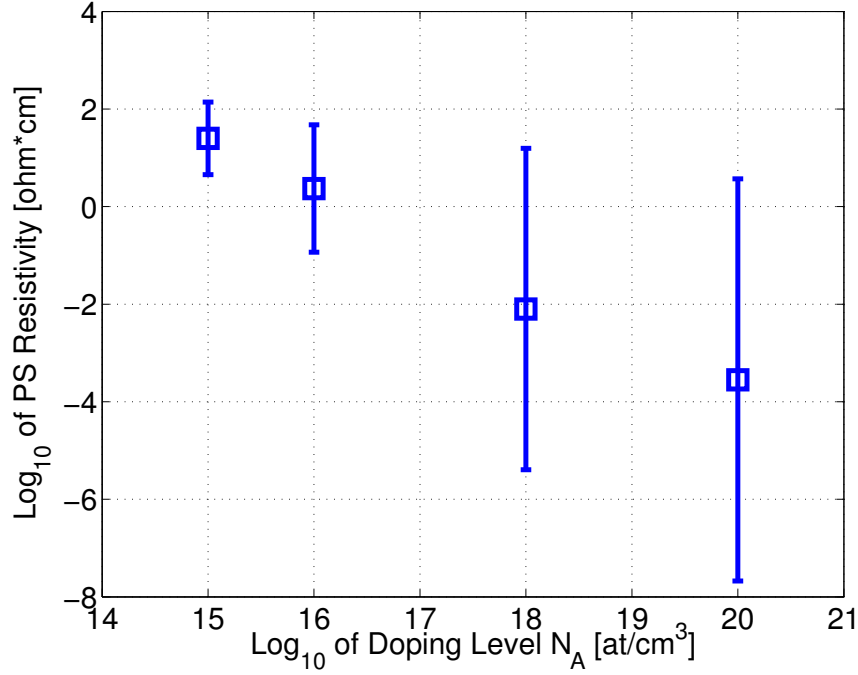


Figure 7.8. Differential Resistivity computed at $V = 1.0V$ averaged over a large number of nanowires with different channel doping.

to the larger amount of carriers available for transport.

The methodology described in this chapter presents some intrinsic limitations. On one side, it relies on the availability of software capable to simulate physical quantities in the structure. Devising a model which could be implemented without any other dependency is actually a problem worthy to be investigated. On the other side, the dimensions of the wires considered were so large that a classical drift-diffusive regime of transport was assumed to hold. Quantum effects, in particular quantum potential confinement due to porous regions, was taken into account via a potential correction known as Bohm potential. When the dimensions of the wires and of the pores are dramatically reduced entering the nanometer regime, the drift-diffusive transport is not realised and a description of quantum transport becomes necessary. To overcome these limitations a new model has been devised: we built a simulative tool which allows to describe in a fully quantum manner the problem of transport in PSNWs highlighting the pivotal role played by quantum effects (potential confinement and coherence). The presentation of this model is given in the upcoming chapters.

Chapter 8

Going smaller

The preceding chapters were focused on the description of a simulative model for Porous Silicon Nanowires. There, we presented a methodology to simulate a porous silicon structure which allowed to understand the main transport mechanisms involved in the conduction process. This enlightened the pivotal role played by the path constrictions in the structures: the high-field mobility saturation occurring in the same regions has been adduced as the principal cause of the non-linear behaviour of current with voltage. Before going ahead, an important remark is in order on the dimension scale of the devices analysed. We studied nanowires with lengths of hundreds of nanometers. The transport properties in these structures are mainly related to drift-diffusion process, efficiently described by semi-classical models. On the other side, quantum effects are strongly limited to the potential confinement effect in the direction perpendicular to transport. Hence, a quantum correction, like the one implemented in the model, is capable of taking into account the physics behind conduction.

These premises pose the problem of transport modelling in PSNWs with smaller dimensions. In this intriguing situation, the channel length is of the order of a few nanometers and the section side is smaller than 10nm. The corresponding configuration of the device makes unavoidable a fully quantum treatment of the problem, now largely dominated by quantum effects and coherent transport.

The aim of this chapter is to give an overview of the quantum theory of transport in coherent structures. In the first section a description of the main features of quantum transport is given. Then, the known Landauer-Buttiker formalism is presented and the main parameters entering the model (transmission spectrum, current) will be introduced.

8.1 Theoretical Background on Transport

8.1.1 Quantum Transport

Differently from classical transport, the characteristics of quantum transport stem from unique peculiarities such as coherence and quantization well described by quantum physics. Quantum transport is consequently resolved into several regimes mainly depending on a lengthscale comparison. These classifications are crucial to understand mesoscopic conductor transport properties. Besides Fermi wavelength, other relevant characteristic lengths are defined for classified transport regimes: (1) mean free path, l_{mfp} , (2) thermal diffusion length, l_T , and (3) phase coherence length, l_ϕ .

Mean Free Path l_{mfp} Mean free path, as the name indicates, is an average distance in which particles can move freely. The hindrance to free motion is due to scattering by defects, impurities or grain boundaries. Elastic scattering does not conserve momentum but energy, while inelastic scattering changes both momentum and energy of incident particles. Thus, mean free paths due to elastic and inelastic scattering should be differentiated although generally l_{mfp} refers to the elastic mean free path. In semiconductors l_{mfp} is closely related to the mobility of carriers and in metals it is much longer than λ_F . As l_{mfp} becomes comparable to λ_F , systems with such l_{mfp} are called in the dirty limit.

Thermal Diffusion Length l_T At non-zero temperatures, electron wavepackets have energy width about $k_B T$ where k_B is the Boltzmann's constant and T is the temperature. This energy uncertainty induces diffusion in time. l_T is a characteristic length of diffusion process due to thermal energy.

Phase Coherence Length l_ϕ Within l_ϕ , particles preserve their phase. Dynamical interactions including mutual Coulomb interactions among electrons and electron-phonon interactions disturb phase coherence. Therefore, this length is important to determine whether quantum interference effects from phase coherent sources can be detectable or not in systems.

Regime	Condition
Ballistic	$L_x, L_y, L_z < l_{mfp}, l_T, l_\phi$
Diffusive	$l_{mfp}, l_T \ll L_x, L_y, L_z$
Dissipative	$l_\phi < L_x, L_y, L_z$

Table 8.1. Classified quantum electron transport

Comparisons of such scales define three distinct transport regimes in Table 8.1. Varying the physical length of mesoscopic conductors we enter different regimes. Condition states that both in dissipative and in diffusive regime, transport quantities are dominated by scattering process similar to classical case. In detail, dissipative conductors suffer from inelastic as well as elastic scattering losing previous information of momentum and energy, whereas diffusive conductors have elastic scatterers, preserving momentum but not energy. For the ballistic regime, on the other hand, all dimensions of ballistic conductors are much smaller than all length scales, namely electrons participating in conduction process do not encounter any kinds of scattering sources without modifying momentum and energy.

As an extension from classical argument between resistance and scattering, ballistic conductors are not resistive at all in principle. It is true and indeed confirmed empirically with a special care to eliminate the contact resistance between electron reservoirs and a ballistic conductor [89]. It implies that ballistic conductors in measurements have non-zero resistance, but it comes not from scattering processes but from electron modes selected at the interface of a reservoir and a conductor. There needs to be an alternative way to express resistance beyond Ohm's law. Landauer captured the significance of the wave nature of charge carriers in mesoscopic conductors, and he developed the theory to estimate resistance or conductance in terms of transmission probabilities of propagating electron modes analogous to electromagnetic photon modes. He predicted a finite resistance of mesoscopic conductors connected to electron reservoirs at both ends without introducing scattering [90]. His prediction which was back then at the heart of controversy against the classical perspective of resistance had driven intensive experimental efforts on ballistic transport by designing appropriate device structures and geometries QPC in previous section closed the controversy with observation of conductance plateaus in the ballistic regime [91, 92].

Previous perspectives to envision resistance properties are based on single and independent particle picture. The final quantity of resistance is computed by multiplying the one electron value with the total number of electrons. This single-particle picture works very well in conductivity of bulk systems and Landauer's theory since interactions between electrons and nucleus and electrons and electrons are negligible in high dimension by efficient screening. However, interactions affects electron transport rather significantly in lower dimensions partly because of low electron density and partly because of insufficient screening among particles. Therefore, single-particle picture breaks down in lower dimensional conductors and it should take into account of interactions. It is not a simple task to handle various forms of interactions with many electrons, especially Coulomb interactions between electrons are notoriously difficult to be solved in an analytical manner. Such conductors where particle-interactions cannot be ignored are particularly called 'strongly correlated systems'.

8.2 Mesoscopic electron transport

The preceding chapter discussed main features and differences between classical and quantum transport. In a very general conceptual framework, transport processes are related to the response of a system to external stimulation. For example, firing up a part of a system generates a temperature gradient, inducing a net heat flow across it. Closely connected to the thermal conduction, the movement of electrons due to a non-zero electrical potential along a system yields electrical conductivity, one of the material characteristics. Conductivity measurements by probing a current change according to a bias voltage across a system, have provided valuable information to identify the states of matter, metal or insulator. The next section pays a particular attention to the electrical transport properties, discussing fundamentals and the implications in mesoscopic conductors.

8.3 Linear Response Theory

Linear response theory (LRT) raises a practical question: how a system in equilibrium responds when its equilibrium state is disturbed. It formulates the response function of a many-particle system which is stimulated by an external source. LRT assumes that the external stimulation is weak enough that it can be treated as a perturbation, justifying the Taylor series expansion. Plus, the perturbation expansion series are converging rapidly after the first linear term; thus, considering the first non-trivial linear term would be sufficient to describe the response of systems. This response function is a measurable quantity, therefore it is real-valued. In transport, the response function is a macroscopic transport coefficient. Since it is shown that the response function relates to the correlation functions in the system, LRT describes a nonequilibrium system in terms of fluctuations about its equilibrium state. Therefore, understanding the dynamics of a system in equilibrium is essential to predict nonequilibrium situations.

Suppose we have a system whose isolated Hamiltonian is denoted as H_0 . If a weak time-dependent disturbing field $A \cdot F(t)$ is applied to the system at time t_0 , the perturbed Hamiltonian H at later time t becomes $H = H_0 - A \cdot F(t)$ where A is the internal quantity conjugate to the field $F(t)$. LRT says that the average of A in the nonequilibrium $\langle A(t) \rangle$ can be written as

$$\langle A(t) \rangle = \langle A(t) \rangle_0 + \int_{-\infty}^t dt' R(t, t') F(t') + O(F(t)^2) \quad (8.1)$$

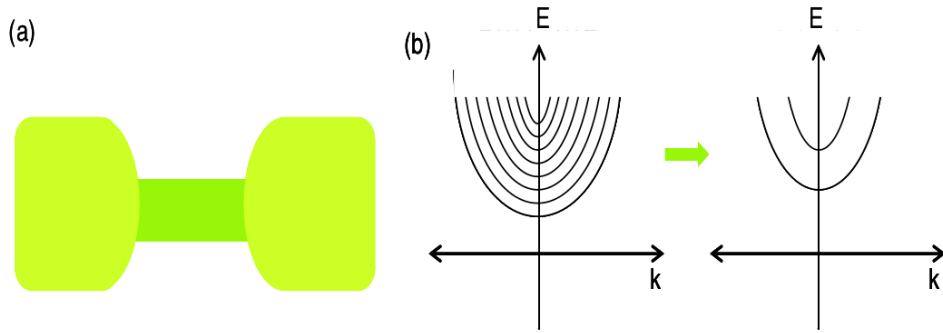


Figure 8.1. (a) An one-dimensional ballistic conductor in a two-terminal configuration. (b) The energy dispersion of free electrons in a reservoir (left) and a conductor (right).

where $\langle \dots \rangle_0$ is the average over equilibrium ensembles. $R(t, t')$ is the linear response function, which relates two times t' and t . t' is the time at which the external field acts on the system and t is the time of measurement. Thus $t > t_0$, it is the causality property. A simple example of the response function is the conductivity in equilibrium, which in connection with Eq.8.1 is known as the Green-Kubo formula. It states that the equilibrium conductivity σ of a one-dimensional system subjected to a constant voltage V at time $t = 0$ is given in terms of the current density $j_x(t)$ along the x-direction,

$$\sigma = \frac{V}{k_B T} \int_0^\infty dt \langle j_x(0) j_x(t) \rangle_0 \quad (8.2)$$

Conductance in mesoscopic conductors can be computed as the response function described above. Note that the mathematical strategies are different depending on which regime (either ballistic or diffusive) the actual transport occurs.

8.4 Ballistic Transport

Ballistic transport refers to the transport of electrons without encountering any types of scattering sources. In other words, the system size is smaller than the mean free path and the inelastic scattering length. Based on the point of view that conductance arises from scattering, conductance is predicted to be infinite in the ballistic regime; however, finite conductance has been measured in the ballistic conductors. This observation boosted theoretical interests to understand the origin of finite conductance.

8.4.1 Landauer-Buttiker Formalism

Landauer brilliantly captured the wave nature of electrons in mesoscopic conductors, and he interpreted the conductance as the transmission probabilities of propagating modes analogous to electromagnetic fields in optical waveguides. Suppose a simple one-dimensional (1D) ballistic conductor with two leads coupled to bulk electron reservoirs, as illustrated in Fig. 8.1(a). Adiabatic transition from bulk reservoirs to the device and zero temperature are assumed. In case of free electrons, Fig. 8.1(b) presents the energy dispersion relations in bulk reservoirs (left) and the conductor (right). The horizontal axis represents the longitudinal wavenumber k . Due to the spatial confinement, the allowed modes in the conductor are discrete, while the modes in the bulk are relatively dense. Therefore, not all modes below the Fermi energy can propagate into the conductor due to energy and momentum conservation, yielding that only certain modes can be matched in both regions. Mode reflection at the interface of two dissimilar materials causes finite conductance even with a ballistic conductor. Sometimes this finite resistance is called 'contact resistance'. In the simplest case, one channel in the conductor exists. The current I across the conductor with the applied bias voltage V is given as $\int_{E_F}^{E_F+eV} e\rho(E)v_g(E)dE$ with energy-dependent density of states ρ and group velocity v_g . The density of states ρ in 1D is given by $1/2\pi\hbar v_g(E)$. Note that in 1D, there is a magic cancellation of the velocity component, yielding the product of $\rho(E)$ and $v_g(E)$ is constant $1/h$. Thus, the current including spin degeneracy is

$$I = \int_{E_F}^{E_F+eV} e \frac{2}{h} dE = \frac{2e^2}{h} V \quad (8.3)$$

reducing the conductance G to $G = I/V = 2e^2/h \equiv G_Q$ denoted as the spin-degenerate quantum unit of conductance. G_Q is measured when the mode is completely transmitting into the opposite reservoir. For a mode which is transmitting with a probability T , the conductance G is $G = G_Q T$. Moreover, if there are more than one channel involved in the transport process and each mode has an individual transmission probability T_i , then the conductance G is obtained as a sum over all modes

$$G = G_Q \sum_i T_i \quad (8.4)$$

known as the 'Landauer formula' [72, 73]. Then, Buttiker further extended the Landauer's formula into multi-lead and multi-mode systems even in presence of a magnetic field. He established coherent scattering formalism. Conductance measured in two leads α and β is ,

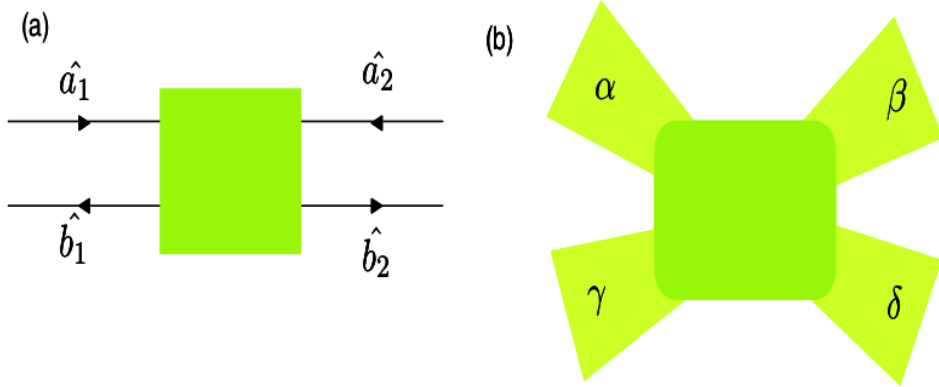


Figure 8.2. A two-port system represented by second quantized operators.

$$G_{\alpha \rightarrow \beta} = G_Q \sum_{n=1}^{N_\alpha} \sum_{m=1}^{N_\beta} |t_{\beta\alpha, mn}|^2 \quad (8.5)$$

with channel modes m, n .

8.4.2 Scattering matrix and Transfer Matrix

Second quantization representation is an elegant way to describe mesoscopic conductors. This is powerful in many aspects: first, it deals straightforwardly with indistinguishable many particles; second, it automatically satisfies exchange rules of bosons or fermions. The previous 1D, one-channel conductor is regarded as a two-port system drawn in Fig. 8.2(a). The operators \hat{a}_i annihilate particles in the incoming channels into the scattering site, and the operators \hat{b}_i do in the outgoing channels. The index i is either 1 or 2. How incoming and outgoing operators are related is written in a compact matrix form. There are two different ways to connect those operators: (1) scattering matrix S and (2) transfer matrix T . A certain form is more efficient than the other, depending on the situation. The components of these matrices are transmission and reflection coefficients between corresponding modes.

Consider an example to view how to form the matrices with a two-port system with one channel. First, the S-matrix gives an obvious connection of the incoming channels versus the outgoing channels such that

$$\begin{pmatrix} \hat{b}_1 \\ \hat{b}_2 \end{pmatrix} = \begin{pmatrix} r_{11} & t_{12} \\ t_{21} & r_{22} \end{pmatrix} \begin{pmatrix} \hat{a}_1 \\ \hat{a}_2 \end{pmatrix} \equiv S \begin{pmatrix} \hat{a}_1 \\ \hat{a}_2 \end{pmatrix} \quad (8.6)$$

Since S is unitary, $SS^\dagger = S^\dagger S = 1$, two conditions among components should be met:

$$SS^\dagger = \begin{pmatrix} r_{11} & t_{12} \\ t_{21} & r_{22} \end{pmatrix} \begin{pmatrix} r_{11}^* & t_{21}^* \\ t_{12}^* & r_{22}^* \end{pmatrix} = \begin{pmatrix} 1 & 0 \\ 0 & 1 \end{pmatrix} \quad (8.7)$$

, reading that

$$|r_{11}|^2 + |t_{12}|^2 = |r_{22}|^2 + |t_{21}|^2 = 1 \quad (8.8)$$

$$r_{11}t_{21}^* + t_{12}r_{22}^* = r_{11}^*t_{21} + t_{12}^*r_{22} = 0 \quad (8.9)$$

Second, a T-matrix describes how the left operators propagate to the right side:

$$\begin{pmatrix} \hat{b}_2 \\ \hat{a}_2 \end{pmatrix} = \begin{pmatrix} T_{11} & T_{12} \\ T_{21} & T_{22} \end{pmatrix} \begin{pmatrix} \hat{a}_1 \\ \hat{b}_1 \end{pmatrix} \equiv T \begin{pmatrix} \hat{a}_1 \\ \hat{b}_1 \end{pmatrix} \quad (8.10)$$

The benefit of the T-matrix representation is to readily compute the overall T-matrix T_{all} as a particle propagates several T-matrices until it reaches the final location. Explicitly, it means

$$\begin{pmatrix} \hat{b}_N \\ \hat{a}_N \end{pmatrix} = T^{(N)}T^{(N-1)} \dots T^{(1)} \begin{pmatrix} \hat{a}_1 \\ \hat{b}_1 \end{pmatrix} \equiv T_{all} \begin{pmatrix} \hat{a}_1 \\ \hat{b}_1 \end{pmatrix} \quad (8.11)$$

Thus, T_{all} expresses $T_{all} = T^{(N)}T^{(N-1)} \dots T^{(1)}$. The components of T are rewritten in terms of r_{ij} and t_{ij} ,

$$T_{11} = t_{21} - \frac{r_{11}r_{22}}{t_{12}} \quad (8.12)$$

$$T_{12} = \frac{r_{22}}{t_{12}} \quad (8.13)$$

$$T_{21} = -\frac{r_{11}}{t_{12}} \quad (8.14)$$

$$T_{22} = \frac{1}{t_{12}} \quad (8.15)$$

8.5 Conclusions

In this Chapter we briefly reviewed the theoretical framework of Transfer Matrix Formalism and Landauer formulas for current. As already mentioned, their validity extends to the coherent regime of transport of nanostructures whose dimensions are smaller than the so-called coherence length. Specifically, they both rely on the assumption of absence of inelastic scattering meaning that electrons are free to move

from one electrode to the other of the device without experiencing inelastic scattering, like phonon-electron scattering.

The Transfer Matrix Formalism and the Landauer formula represent the main ingredients of the numerical model for Porous Silicon Nanowires which will be presented and discussed in the next chapters. As it will become clear, they will be exploited to derive a methodology to describe a simplified scheme of Porous Silicon Nanowires and to compute their main electrical quantities.

Chapter 9

A New Model for PSNWs

9.1 Introduction

The overview of the last chapter on ballistic transport and on the main theoretical tools adopted to describe the transport properties of semiconducting nanostructures represents the starting point of a new model for Porous Silicon Nanowires. This model will be discussed in this Chapter.

As it will be clarified soon, a Porous Silicon Nanowire is here modelled with a sequence of Silicon Nanocrystals and Nanowires immersed in a dielectric matrix. Hence, profound differences exist between this simple scheme of PSNW and the numerical model we presented some chapters ago. In particular, the nature of a sequence of nanocrystals and nanodots intrinsically requires a quantum treatment of the problem while the drift-diffusive transport was supposed in the other modelling methodology. Not secondarily, non diffusive transport in absence of inelastic scattering strongly modifies the overall electrical behaviour of these devices.

The model we are going to present is easily scalable to arbitrarily long structures (with lengths smaller than the coherence length) and allowed us to conduct a systematic study of electron transport properties of 1D porous silicon nanowires [177, 176, 149]. Nanocrystals and wires dimensions in the structures are here considered randomly chosen variables. Thus, transmission spectrum, conductance and current are evaluated and statistically averaged over a large number of structure configurations. As a result, a deeper understanding of transport in realistic random sequences of crystals and wires is obtained via a quantitative description of the phenomena involved. The impact of the geometrical properties of the device is also extensively discussed.

The chapter is organised as follows: in section 9.2 the model of PSNW is described while in sect. 9.3 we briefly digress upon existing models. The theoretical quantities used for its analysis are then presented in Sect. 9.4. A fundamental role

in the envisioned procedure is played by the transmission spectrum of dots and wires whose discussion takes sect. 9.4. The self-consistent technique adopted to model self-charge interaction is discussed in sect. In the next Chapter we will present the results of the model validation for small structures along with the results of a systematic analysis of transport in 1D random arrays of dots and wires.

9.2 The System

In this section we give a detailed description of the 3D system which will be analysed and studied in the following. We will consider a structure constituted by a succession of silicon nanocrystals, with dimensions smaller than 5 nm, and longer sections of silicon nanowires. The structure is schematically depicted in fig.9.1.

Specifically, a random spatial distribution of silicon nanocrystals, behaving as Quantum Dots (QD's or 0-D systems), is connected through longer sections of wires (1-D systems) thus creating a disordered electrostatic potential. The corresponding potential profile results in a sequence of wells and barriers: the former, corresponding to the silicon blocks, the latter to the separation gaps filled with insulator (air in our case). An example of potential distribution is shown in fig 9.2.

In our model Silicon nanocrystals are taken to be of parallelepiped shape with linear dimensions smaller than 5nm guaranteeing a quantum confinement in all spatial directions. On the contrary, longer pieces of silicon nanowires are chosen with a longitudinal dimension larger than 8nm in the direction parallel to transport. Moreover, distances among the different blocks belong to the range of some nanometers (less than 4nm and larger than 1nm) in order to ensure a weak coupling between two adjacent blocks.

The first and last blocks of the succession are coupled to two electrode contacts working as ideal carrier reservoirs. As it will be proved, the coupling effect with the contacts is of pivotal importance for the conduction properties of the whole disordered system.

9.3 Digression

The model for PSNW which we have just presented can be viewed as a specific realization of a more general paradigm of semiconducting nanostructures in which the embedding of low-dimensional structures in an insulating matrix is realized. These devices have already been fabricated and showed interesting properties (Coulomb blockade, Kondo effect [140]). In particular, experimental procedures have been assessed which are capable of producing structures composed of coupled quantum dots where the dot interaction determines the overall transport properties [141, 142, 143].

This led, among all, to the demonstration of the concept of multi-dot memory using semiconductor nanocrystals embedded in an insulator matrix as floating-gate [144] and of the single-electron transistor [145].

From a theoretical viewpoint, research has mostly focused on single QDs discovering many novel transport phenomena, such as the staircaselike current-voltage (I-V) characteristic [150], Coulomb blockade oscillation [151], negative differential capacitance [152] and the Kondo effect [153]. Electron transport through several QDs has been the object only of recent investigation and models have been proposed using NEGF technique [154, 155] and taking into account the potential due to the self-interaction. Only small systems can, however, be analysed with this approach, suffering for a lack of scalability.

9.4 The Model

We present here the model adopted to analyse the structure described above. The theoretical framework for the present discussion is the transfer matrix formalism, largely applied in the study of electron transport in mesoscopic systems in presence of coherent transport [135]. Together with the standard Landauer theory, this approach allows to calculate the current flowing in the system via the simple formula

$$I(V) = \frac{e}{\hbar} \int_{-\infty}^{+\infty} \frac{d\epsilon}{2\pi} T^{(n)}(\epsilon, V) (f_L(\epsilon - \mu_L) - f_R(\epsilon - \mu_R)) \quad (9.1)$$

where $f_{L/R}(\epsilon) = [\exp((\epsilon - \mu_{L/R})/T) + 1]^{-1}$ is the Fermi-Dirac function of the left/right electrode, $\mu_{L/R} = \pm eV/2$ are the corresponding electronic chemical potentials under a symmetrical drop of the applied voltage V and T is the temperature in energy units.

The quantity $T^{(n)}(\epsilon, V)$ corresponds to the transmission coefficient of the structure obtained as a result of the application of transfer matrix tool. The remainder of the section describes the procedure we adopted to compute it.

We divide the original system in n components called "blocks" (see fig.9.3), where each block can be a silicon nanocrystal (QD) or a silicon nanowire (1D wire) with given geometrical parameters. The generic k -th block is described by the transfer matrix

$$M_k = \begin{bmatrix} \alpha_k & \beta_k \\ \beta_k^* & \alpha_k^* \end{bmatrix} \quad (9.2)$$

with the condition $|\alpha_k|^2 - |\beta_k|^2 = 1$, in order to satisfy the properties of flux conservation and time-reversal invariance.

Exploiting the polar representation of transfer matrices [160], the matrix can be expressed in the form

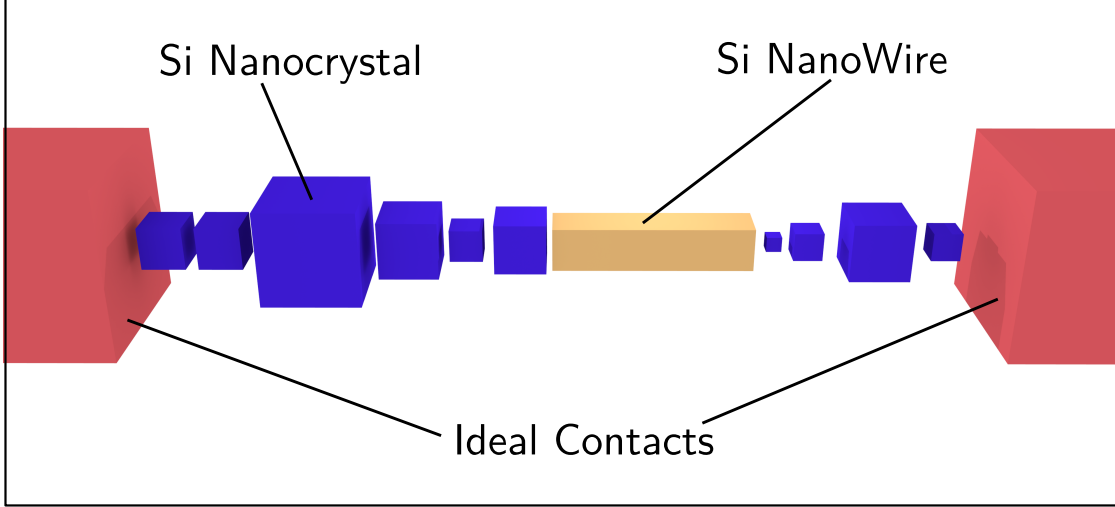


Figure 9.1. General structure of system investigated in the present work. A sequence of silicon nanocrystals (in blue) and silicon nanowires (in orange) is depicted. For simplicity a parallelepiped shape of the blocks is considered. The structure is then contacted with two ideal carrier reservoirs, in red in figure.

$$\begin{aligned}
 M_k &= \begin{bmatrix} \alpha_k & \beta_k \\ \beta_k^* & \alpha_k^* \end{bmatrix} \\
 &= \begin{bmatrix} e^{i\phi_k} & 0 \\ 0 & e^{-i\phi_k} \end{bmatrix} \cdot \begin{bmatrix} \sqrt{1+\lambda_k} & \sqrt{\lambda_k} \\ \sqrt{\lambda_k} & \sqrt{1+\lambda_k} \end{bmatrix} \\
 &\cdot \begin{bmatrix} e^{i\psi_k} & 0 \\ 0 & e^{-i\psi_k} \end{bmatrix}
 \end{aligned} \tag{9.3}$$

Here ϕ_k and ψ_k are phases and λ_k is the "radial parameter" of the given representation. The formers express the coherence contribution to the transfer matrix and their behaviour depends in a complicated way on the geometrical parameters of the block [159]. On the contrary, a simple relation links the radial parameter λ_k to the physically relevant transmission coefficient T_k of the k -th block, yielding

$$T_k = \frac{1}{1 + \lambda_k} \tag{9.4}$$

This equation plays a fundamental role in our model since it allows to construct the transfer matrix of each block of the chain from the transmission coefficient of the same block. In the following section we will describe the expressions for the

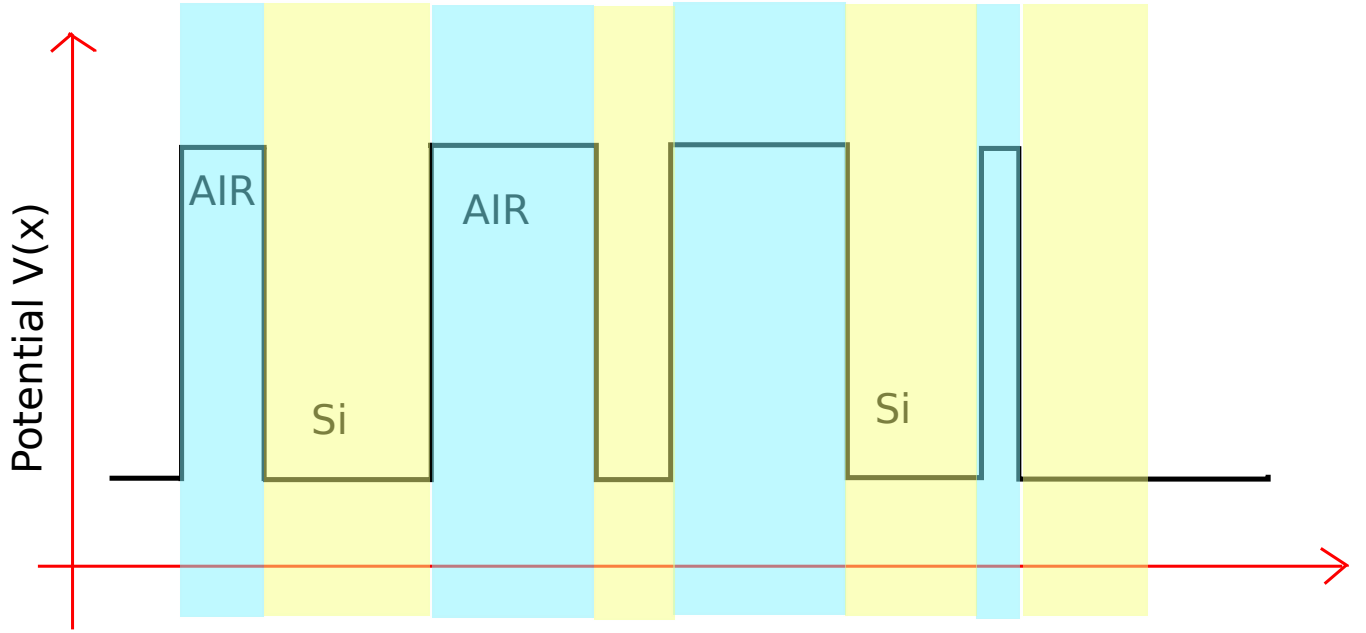


Figure 9.2. Example of simplified potential in the structure. Quantum wells and barriers correspond to quantum dots and insulating layers respectively.

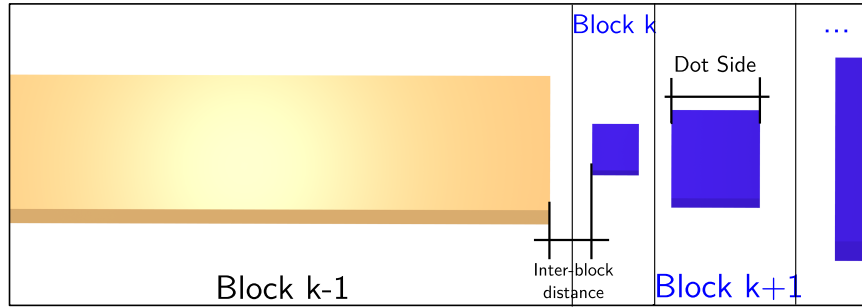


Figure 9.3. Larger picture of the main parameters entering the model: the side of the blocks and the relative distances.

transmission coefficient of a Quantum Dot and a Quantum wire.

The transfer matrix of the chain of n blocks is eventually given by the product

$$\begin{aligned} M^{(n)} &= M_n \cdots M_k \cdots M_2 M_1 \\ &= \begin{bmatrix} \alpha^{(n)} & \beta^{(n)} \\ \beta^{(n)*} & \alpha^{(n)*} \end{bmatrix} \end{aligned} \quad (9.5)$$

from which the transmission coefficient of the chain of the n blocks is derived via

$$T^{(n)} = \frac{1}{\alpha^{(n)}} \quad (9.6)$$

It is now necessary to discuss the dependence on the energy of the various parameters introduced above. The elements of the transfer matrices and, in particular, the radial and phase parameters, show, indeed, a strong dependence on the energy. However, while it can be reasonable to assume a particular behaviour of the transmission coefficient (and hence of λ) of the blocks with energy (see the following section), the task is instead of formidable complexity for ϕ_k and ψ_k , given the huge number of geometrical parameters entering the system. Consequently, we will limit ourselves to discuss the results of transmission properties upon properly averaging over the phase parameter values.

9.5 Transmission coefficient

The model described in the preceding section relies on the knowledge of the radial parameter appearing in the transfer matrix for each block. The radial parameter $\lambda(\epsilon)$ of each block can be easily deduced from the transmission coefficient $T(\epsilon)$ (see eq.(9.4)). We now describe the particular shape of the transmission coefficient adopted for a nanocrystal and a nanowire.

9.5.1 Nanocrystal

In a silicon nanocrystal, quantum confinement effect along all spatial directions ultimately determines the formation of discrete energy levels in the density of states of the system. In the case of an isolated cubic nanocrystal with side L , the laws of quantum mechanics dictate that the allowed energies of a particle are

$$E_{n_x, n_y, n_z} = E_0 + \frac{\hbar^2 \pi^2}{2m^* L^2} (n_x^2 + n_y^2 + n_z^2) \propto \frac{\hbar^2}{m^* L^2} \quad (9.7)$$

where m^* is the effective mass of the particle, E_0 is the reference energy with respect to the Fermi level at equilibrium ($E_F = 0$), $\hbar = h/(2\pi)$ is the reduced Planck's constant and $n_{x,y,z} = 1, 2, 3, \dots$ are quantum numbers.

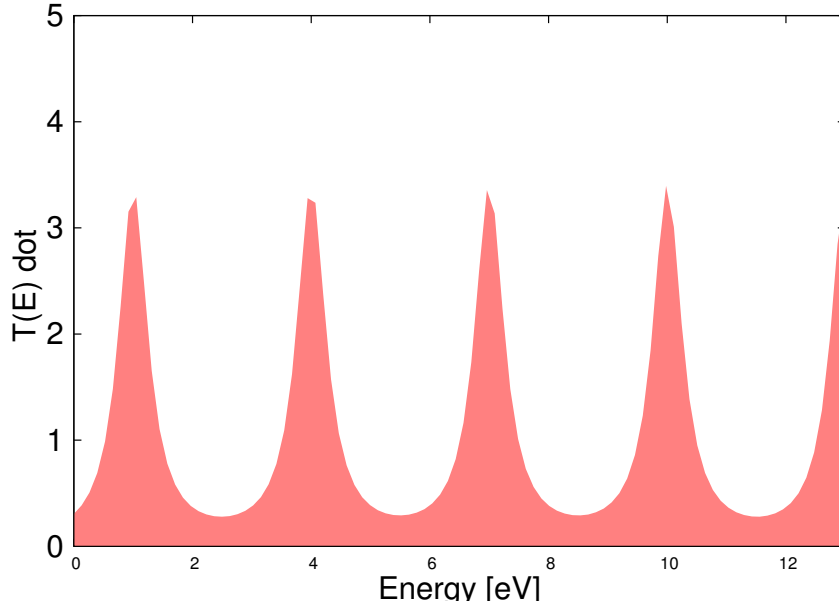


Figure 9.4. Example of Transmission Spectrum of Nanocrystal.

When, however, the dot is coupled to electrodes or neighbouring systems, interactions are known to provoke a broadening of the above energy levels. The energy width of the dot levels due to the electron transfer coupling to the left and right systems is given by Γ^K , $K = L, R$. In terms of the Hamiltonian of the system, these widths equal $\Gamma^K = 2\pi \sum_{k \in K} |V_{kK}|^2 \delta(E - \epsilon_k)$, where V_{ik} are the coupling matrix elements [135].

Following a common tradition, the transmission coefficient of a coupled dot can then be expressed through the simple approximated formula

$$T_{dot}(\epsilon) = \sum_N \frac{\Gamma_N^L \Gamma_N^R}{(\epsilon - \epsilon_N)^2 + (\Gamma_N/2)^2} \quad (9.8)$$

where $N = \{n_x, n_y, n_z\}$ is a composite index and $\Gamma_N = \Gamma_N^L + \Gamma_N^R$. It is noteworthy to highlight that the Γ 's of each block depend on its distance from the adjacent blocks, on the density of charges in them, the dimensions of the latter and on the applied voltage V . Given the complicated nature of these parameters, in the following analysis we will neglect, for simplicity, the explicit dependence of Γ 's on V and we will treat the interaction effects in the structure due to the potential drop through the self-consistent field procedure described in the next section. An example of transmission spectrum for a nanocrystal is shown in fig. 9.4.

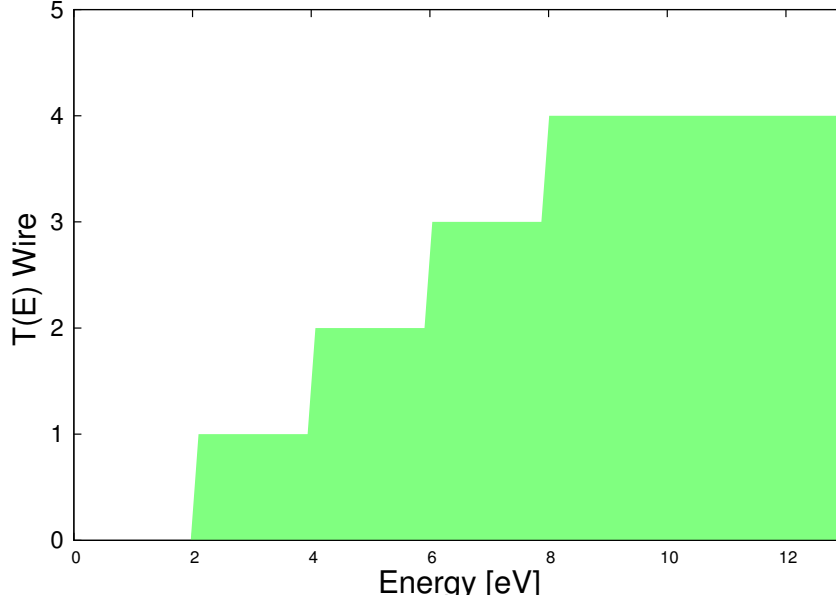


Figure 9.5. Example of Transmission Spectrum of Nanowire (without accounting for spin).

9.5.2 Nanowire

In a silicon nanowire, or sufficiently long sections of it, quantum confinement is almost restricted to the transverse direction while in the longitudinal axis (the direction of transport) electrons are taken to behave like free particles. As a consequence, a continuum of energy levels is available to be occupied by particles. Assuming only one band in the wire and under the effective mass approximation, the transmission coefficient $T_{nw}(\epsilon)$ is simply given by

$$T_{nw}(\epsilon) = 2 \cdot \sum_N \theta(\epsilon - E_{0,N}) \quad (9.9)$$

where $N = \{n_y, n_z\}$ is the composite index of transverse quantum numbers, $\theta(\epsilon)$ is the Heaviside function and $E_{0,N}$ is the bottom energy value of each band depending on the transverse dimensions of the wire according to the formula

$$E_{0,N} = E_0 + \frac{\hbar^2 \pi^2}{2m^* L^2} (n_y^2 + n_z^2) \propto \frac{\hbar^2}{m^* L^2} \quad (9.10)$$

To derive expression (9.9), coupling among different bands has been ignored and no elastic nor inelastic scattering impurities are considered. The factor of 2 accounts for the electron spin.

9.6 Self-consistent field

The model adopted in this study has a pivotal quantity in the transmission coefficient of the structure $T^{(n)}(\epsilon)$ as computed via eq. (9.6). As already mentioned, besides its dependence on the geometrical parameters of the blocks, the transmission coefficient also depends on the applied voltage V . In particular, the application of voltage between the contacts of the system determines a shift of their chemical potentials and a consequent modification of the amount of carriers allowed to enter the system contributing to current. The average charge density consequently varies together with the repulsive electrostatic interaction exerted on new coming electrons. The ultimate effect of this self-interaction can be subsumed in a shift of the peaks in the density of states of each block and thus in the corresponding transmission coefficient. We take into account this phenomenon by rigidly shifting the energy levels of peaks or steps (for QDs and QW's respectively) by a self-consistent energy potential $U_i, \forall i$

$$U_i(V) = U_0(N_i(V) - N_0) \quad (9.11)$$

where U_0 is the charging energy shift due to a single electron in the structure, N_0 is the charge density in the structure at equilibrium $V = 0$ while $N_i(V)$ is the charge density in the i -block at voltage V . The latter is given by

$$\begin{aligned} N_i(V) = & \int_{-\infty}^{+\infty} \frac{d\epsilon}{2\pi} T_i^{(n)}(\epsilon - U(V)) \times \\ & \times [\Gamma_{i,L} f_L(\epsilon - \mu_L) + \Gamma_{i,R} f_R(\epsilon - \mu_R)] \end{aligned} \quad (9.12)$$

The value of $U_i(V)$ is then computed from the self-consistent solution of equations (9.11) and (9.12).

Chapter 10

Model Validation and Results

10.1 Validation

The model discussed in the previous chapter represents an attempt to describe electron transport in a random sequence of silicon nanocrystals and nanowires. Within it, the interactions among charges in the different blocks and the effect of the applied voltage are considered through the self-consistent field procedure of section 9.6. To estimate the correctness of this model we shall compare the results to a quantum calculation based on non-equilibrium Green function technique (NEGF). NEGF approach represents the most used technique for treating ballistic transport problems in nanodevices, efficiently coupling Schrodinger and Poisson equations. In particular, we will exploit the QUANTUM tool implemented in the physics-based simulator TCAD Atlas [127].

In the software, the single-particle Schrodinger equation with an effective Hamiltonian is solved along the structure under the Effective Mass Approximation (EMA). Values of the effective masses adopted are those of bulk silicon (longitudinal mass of $0.190m_0$ in unprimed subbands, $0.916m_0$ in primed subbands). The effective potential profile adopted in the Schrodinger problem is, instead, given by a superposition of the wells and barriers due to the material interfaces and of the electrostatic Poisson potential caused by the charge density in the structure.

Current is then calculated in the Landauer-Buttiker formalism starting from the Green's function and the corresponding transmission spectrum.

Before proceeding with the comparison, some considerations on the validity of the results from the mentioned NEGF method are in order. The effective single-particle potential here adopted represents a mean-field treatment of interactions among carriers in nanodevices. In fact, this numerical method is known to poorly describe quantum correlation effects in the system and presents disadvantages analogous to those of the largely investigated Density Functional Theory (DFT) [136].

Similarly, our model, endowed with the self-consistent field method, is not able to provide a sufficiently accurate description of quantum correlations in the system. Notwithstanding, our interest in this work is mainly devoted to long sequences of quantum dots and nanowires, whose geometrical parameters can not be exactly controlled experimentally. Hence, we adopt here a statistical treatment of the problem. Averaging over all the variable parameters in the structure, it is actually expected that quantum correlations should disappear, consequently assessing the validity of the results coming from the current analysis.

10.2 Results and Discussion

In this section we compare the results from our method with the quantum simulations from TCAD. Our attention is limited to sequences of a few quantum nanocrystals and nanowires, the only structures which can be analysed and simulated with the mentioned tool. For longer structures, consisting of more than 4 nanocrystals and 2 nanowires, it is not possible to obtain valuable results from the simulator given the increasing complexity of the structure and the computational limits of the tool.

Hence, we prove the validity of the model showing that excellent accuracy can be reached with a proper choice of the numerical parameters in the model. These sets of parameters will be then exploited in the following to derive information on transport in longer structures for which no validating technique is available.

The structures for which we present results are made of one single nanocrystal, two nanocrystals, and two nanocrystals separated by a long section of silicon nanowire. Besides demonstrating the accuracy of the model, the analysis of these simple cases will offer the chance to discuss the effects of geometrical parameters on electron transport in these systems.

10.2.1 Single Nanocrystal

Fig.10.1 shows the current flowing in a single silicon cubic nanocrystal with varying applied voltage. Different curves correspond to different dimensions of the quantum dot (sides in the range $[2,5]nm$ are considered) while the distance of the dot from the left and right contacts is kept at $1.5nm$. This distance is sufficiently high to guarantee weak coupling between the dot and the contacts, or equivalently stated $\Gamma_{L/R}/\Delta E \ll 1$, where ΔE is the energy difference between the lowest consecutive energy levels of the dot. The latter condition implies a discrete nature of the transmission spectrum of the dot, where no overlapping occurs among different energy levels due to coupling.

In the figure, the data extracted from TCAD (points) and our model (solid lines)

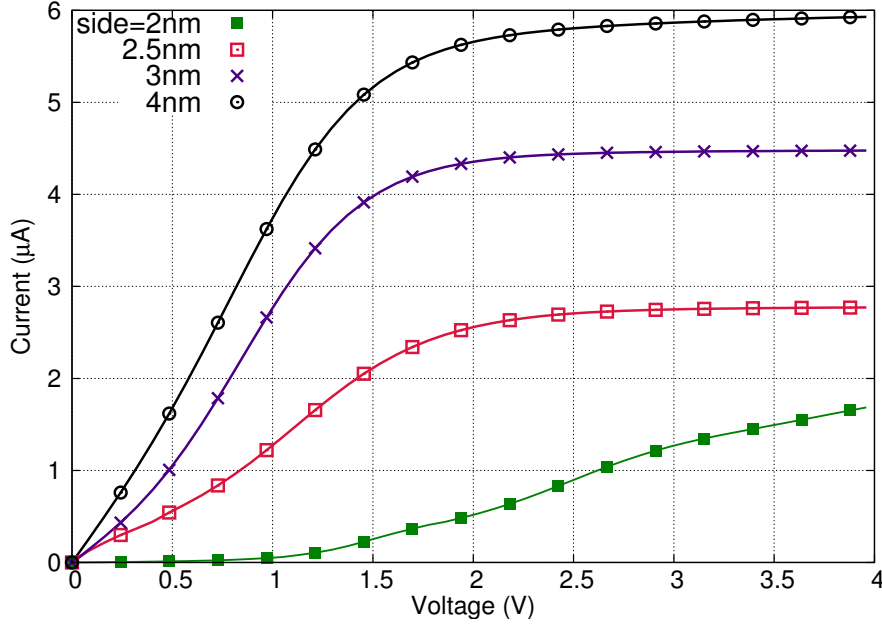


Figure 10.1. Current-Voltage characteristics of cubic silicon nanocrystals for different sizes. Contacts are ideal carrier reservoirs distancing $1.5nm$ from the dot. Points - TCAD Atlas simulation; solid lines - our Model. Model parameters used: $U_0 = 0.01eV$, $\Gamma_{L/R} \in [10^{-4}, 10^{-3}]eV$.

are compared revealing excellent agreement. The parameters adopted in the model to get the results are: $U_0 = 0.01eV$, $\Gamma_{L/R} \in [10^{-4}, 10^{-3}]eV$.

From the I-V curves, it is immediate to note that increasing the size of the nanocrystal results in an increase of the flowing current. The reason of this behaviour can be two-fold. On one side, an increase of the side of the nanocrystal is responsible for a weaker confinement inside the dot; consequently a narrower distribution of energy levels in the energy range relevant for conduction at a specific value of applied voltage is found. This effect is simply described in eq. (9.7). The transmission spectrum eventually contains more peaks which correspond to more energy states available in the system. Therefore, an increase of current is found.

On the other side, increasing the size of the dot, the surface interaction between the dot and the contacts is increased, the Γ 's consequently increase determining higher current in the dot (eq. 9.1). In our case, the analysis of the transmission spectrum of the dots of fig.10.1 reveals that in the conduction energy range considered, the contact coupling effect is the main cause of the current increase. At this point another consideration is worthy to be made. The current in the dots tends to plateau at a given value of applied voltage, whose value is lower for larger dots. The meaning of this resides in the fact that a fixed number of energy levels

entering the bias window contribute to current. Once they have been occupied, current does not increase further. However, an infinity of energy levels is available in quantum dots at higher energies, which will eventually enter the energy range of conduction for higher applied voltages. As a consequence, an increase of current is expected increasing the bias voltage, consistently with the stronger electrostatic interaction.

10.2.2 Sequence of two Nanocrystals

We present now the values of current for two adjacent silicon nanocrystals having different size. In particular, fig.10.2 shows the current characteristics of the series of two nanocrystals, the first of which has a fixed side of $2nm$ while the other's dimension is varied. The distance among the dots and the ideal contacts is $1.5nm$ while the inter-dot distance is $1nm$. Solid lines correspond to the model data while points represent data from TCAD simulations: good agreement among them is evident.

The maximum current in the figure is obtained for equally sized nanocrystals; on the contrary, a gradual decrease occurs when a mismatch in the dimensions is present. A difference of fractions of nanometer in the side of the nanocrystals is actually responsible for a modification in the density of states and in the corresponding transmission spectrum. According to eq.(9.7), the energy levels of different dots generally do not coincide; consequently coherent electrons occupying a certain level in one dot fall outside the allowed energy levels of the other. This amounts to saying that they are most probably reflected back to the first dot (the resulting transmission coefficient is relatively small) and their contribution to current is largely reduced. This phenomenon represents, indeed, a strong limiting factor for current in such structures. A counteracting role is played, however, by the broadening of the energy levels in the density of states (and in the transmission spectrum) due to contact and inter-dot interaction. This permits a partial overlapping of the energy levels and a greater flow of electrons in the structure. Nonetheless, current strongly reduces when a mismatch in the dimensions of the dots is present. In fig.10.3 the transmission spectra at equilibrium for whole structures of fig.10.2 are depicted. The transmission spectra are characterized by peaks in the energy intervals of the energy levels of the individual dots. The amplitude of the peaks, however, decreases when increasing the side mismatch of the dots since energy levels overlapping is gradually reduced.

10.2.3 Nanocrystal + Nanowire + Nanocrystal

The presence of geometrical mismatch between dots in a sequence has been proved to be of pivotal importance for conduction in the heterogeneous systems considered in our work. In particular, in the last section, we have shown how the missing

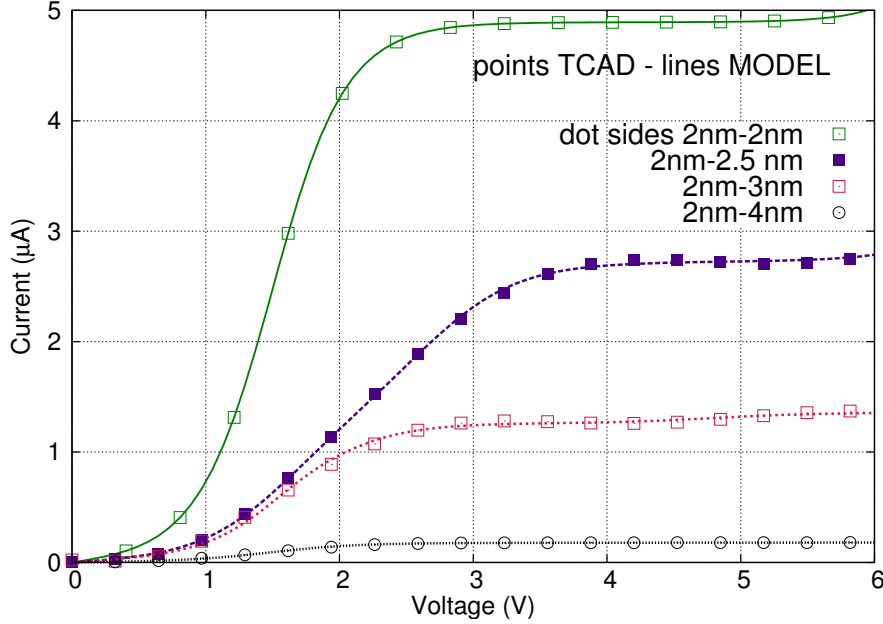


Figure 10.2. Current-Voltage curves of sequences of two nanocrystals for varying dimensions. First dot side $2nm$, Second dot side: $2nm, 2.5nm, 3nm, 4nm$. Contacts are ideal carrier reservoirs distancing $1.5nm$ from the dot. Interdot-distance $1nm$. Points - TCAD Atlas simulation; solid lines - our Model. Model parameters used: $U_0 = 0.01eV$, $\Gamma_{L/R} \in [10^{-4}, 10^{-3}]eV$.

alignment among energy levels in the various blocks determines a lowering in the overall transmission coefficient dramatically reducing the probability of electrons to cross the structure. We now consider a simple structure in which also a section of silicon nanowire plays a role: we focus our attention to a sequence of dots with different size connected through a nanowire (see fig. 10.4).

In fig.10.5 the I-V characteristics of some systems are shown. The sides of the dots are kept fixed and equal $2nm$ and $3nm$ respectively. The side of the wire section is instead varied between $2nm$ and $6nm$. The distance between the dots and the ideal contacts is $1nm$ while the dot-wire separation gaps are $1.5nm$ long. In the plot, points correspond to results from TCAD, lines represent data from our model where $U_0 = 0.01eV$ while the coupling parameters Γ 's are chosen of the order of $10^{-3}eV$. The agreement of the values is easily assessed.

From the figure, generally higher values of current are found for increasing wire section. Moreover, the applied voltage in correspondence of which an almost constant value of current is obtained reduces with the side of the wire. This behaviour can be understood in terms of the transmission coefficient. From formula (9.10), the energies for which a step increase in the transmission spectrum occurs vary proportionally with $1/L^2$, and thus they get smaller for larger sections. Differently

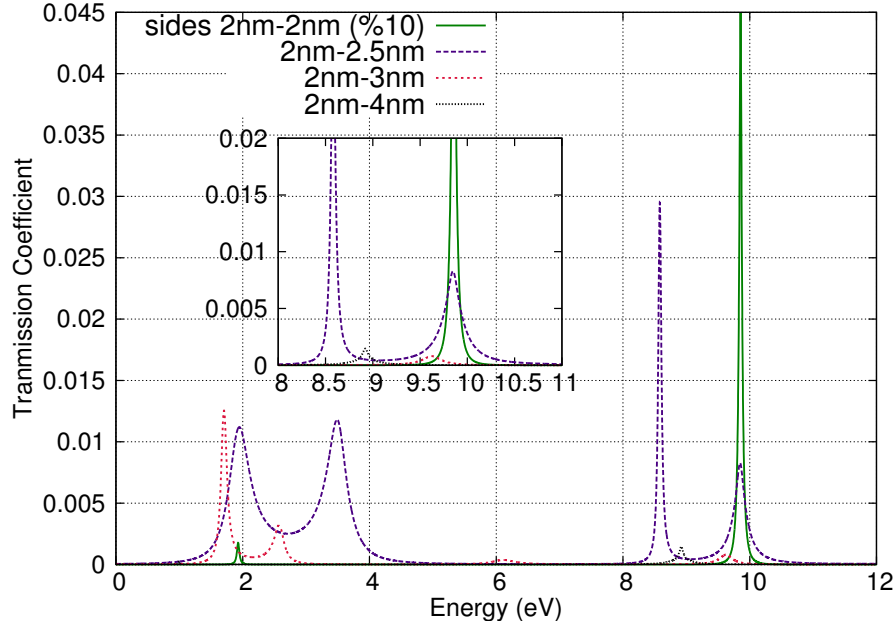


Figure 10.3. Transmission spectrum of the structures of fig.10.2 for $V = 0$: First dot side $2nm$, Second dot side: $2nm, 2.5nm, 3nm, 4nm$. Contacts are ideal carrier reservoirs distancing $1.5nm$ from the dot. Interdot-distance $1nm$. The data are results from our Model. Model parameters used: $U_0 = 0.01eV$, $\Gamma_{L/R} \in [10^{-4}, 10^{-3}]eV$. The green curve is shown after a division by a factor of ten for plotting ease.



Figure 10.4. Scheme of a structure of SiNanocrystal + NW + Nanocrystal

stated, the wire transmission spectrum assumes non-zero values for smaller energy values. As a consequence, electrons entering the wire (from the first dot) with a certain energy can cross the wire without being reflected back; current naturally increases. This effect adds to the increase of current due to the intensified interaction, accounted by the coupling factors Γ 's, between the dots and the wire. The transmission spectra of the four systems are depicted in fig. where it is evident that,

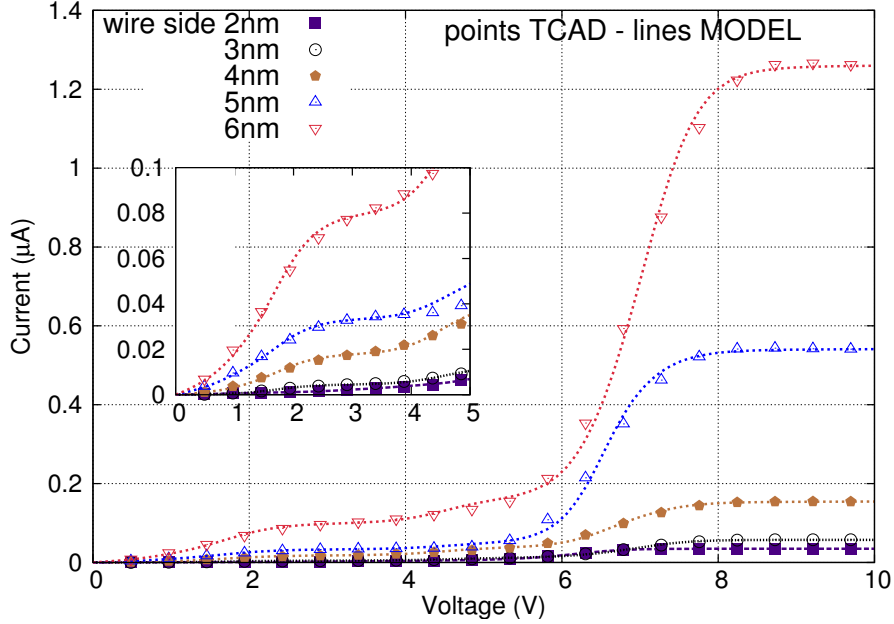


Figure 10.5. Current-Voltage characteristics of structures with two dots connected through a nanowire. First dot side $2nm$, Second dot side: $3nm$, Transverse side of the wire: $2nm, 3nm, 4nm, 5nm, 6nm$. Contacts are ideal carrier reservoirs distancing $1nm$ from the dot. Interdot-distance $1.5nm$. The data are results from our Model. Model parameters: $U_0 = 0.01eV$, $\Gamma_{L/R} \in [10^{-4}, 10^{-3}]eV$. The green curve is shown after a division by a factor of ten for plotting ease.

for increasing wire section, the resulting transmission coefficient in the structure contains peaks at lower energy values.

10.3 Further Analysis

In this section we propose a systematic analysis of electron transport in arbitrarily long sequences of quantum dots and wires. The results will be discussed in terms of transmission spectrum, conductance and current averaged over a considerable number of different geometrical configurations of the structure. In particular, exploiting the useful numerical parameters derived in the simulation process described above, we will show the effect on transport properties due to: A) the porosity, here defined as the ratio of the number of quantum dots (0D) over the total number of blocks in the structure; B) the overall number of blocks constituting the sequence; C) the geometrical parameters of the individual blocks, specifically the average side of the quantum dots and the coupling parameters among them.

All the relevant quantities have been derived through an averaging procedure over many structure configurations in which the position of the dots (and thus of the

wires), their side and coupling parameters have been randomly chosen according to uniform and gaussian probability distributions, respectively.

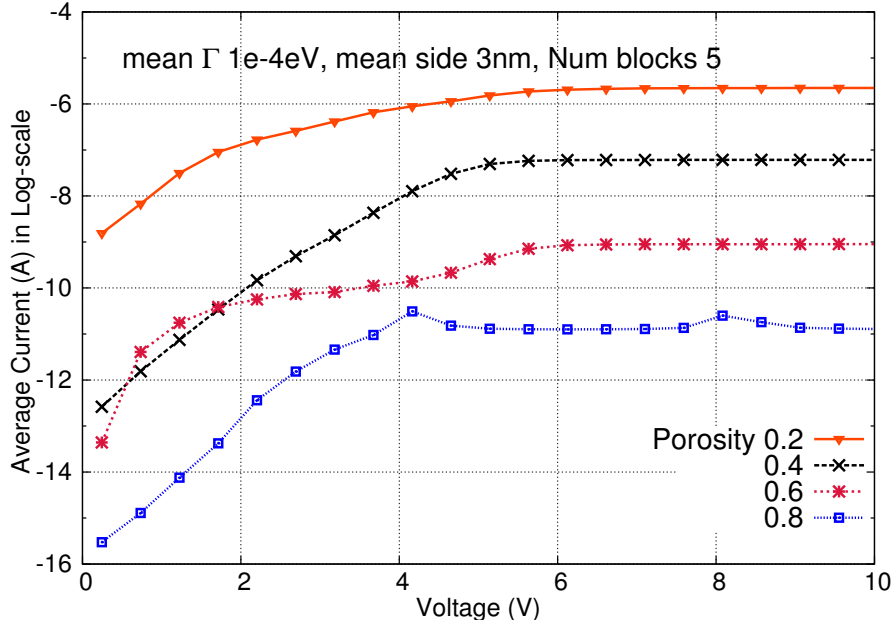


Figure 10.6. Average Current-Voltage characteristics of structures composed of 5 blocks. Different curves are shown in logarithmic scale for different values of porosity (number of dots/ total number of blocks). Average is performed over more than 100 configurations with dot and wire mean side $3nm$ and mean coupling parameters $\Gamma = 10^{-4}eV$. $U_0 = 0.01eV$

10.3.1 Porosity

Given the intrinsic geometrical and electrical differences among quantum dots and one-dimensional wires, the average transport properties of a long sequence of 0D and 1D blocks is expected to largely depend on the relative number of 0D structures with respect to the number of 1D components. In particular, the generally smaller density of state of quantum dots represents one major cause of reduction in conductance and current in the structure. This substantiates our definition of a parameter called *porosity* defined as the ratio between the number of quantum dots and quantum wires in the sequence.

$$Porosity = \frac{\# \text{ nanocrystals}}{\# \text{ totalblocks}} \quad (10.1)$$

The choice of the name stems from the irregular morphology of porous silicon nanowires where crystalline islands (called pores) are embedded in an amorphous

silicon-oxide network lacking of lattice regularity. We will adopt porosity as a fundamental property of the overall block sequence.

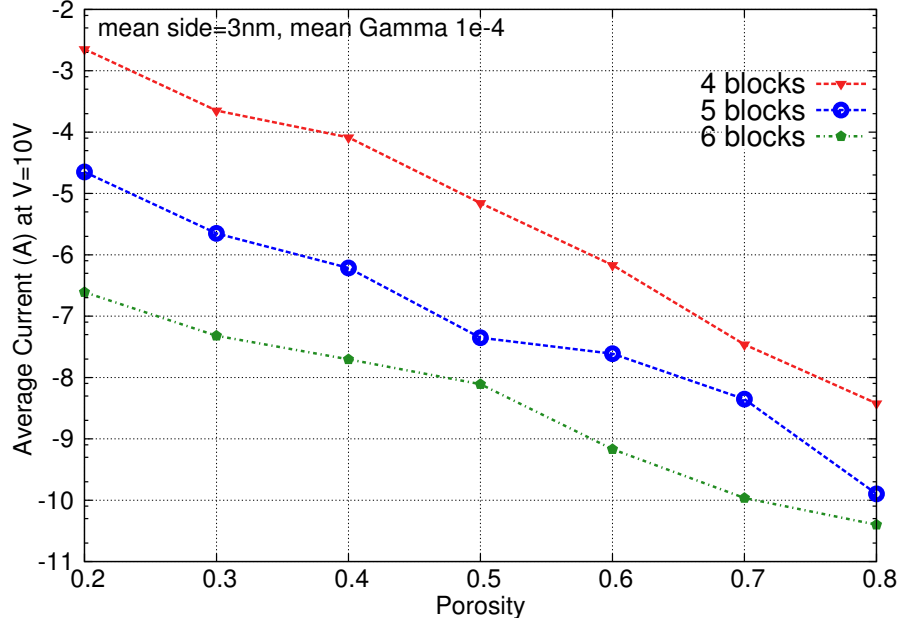


Figure 10.7. Average current wrt porosity at $V=10V$ of structures composed of 5 blocks. Different curves are shown in logarithmic scale for different values of porosity (number of dots/ total number of blocks). Averaging is performed over more than 100 configurations with dot and wire mean side $3nm$ and mean coupling parameters $\Gamma = 10^{-4}eV$. $U_0 = 0.01eV$.

In fig. 10.6 the average current-voltage characteristics are shown for different structures composed of five blocks for different values of porosity, that is of number of dots. The averaging has been performed over a large sample of possible configurations (more than 100) with wire and dot mean side of $3nm$ and coupling parameters Γ 's in the range $[10^{-4}, 10^{-3}]eV$. The behaviour of current with voltage is similar to the one obtained in the previous sections for single nanocrystals, highlighting the determining role played by the dots in the transport process. Moreover, the logarithmic scale of the picture reveals that increasing the porosity of the sequence, a reduction of current of some orders of magnitude is obtained. A better view of this effect is given in fig. 10.7 in which the average current at $V=10V$ is plotted against porosity. An almost exponential reduction of current is found (the current scale is logarithmic).

We expect that increasing the number of dots in sequences with a fixed number of blocks determines a large reduction of the density of states available for conduction

(continuous density bands are substituted by peaks) and a consequently lower current should flow. This is effectively confirmed by the smaller transmission spectrum of the device of fig. 10.8 where the average transmission at $V=10V$ is shown in an energy window relevant for conduction. The evident effect of an increase of porosity is a decrease of transmission in the structure.

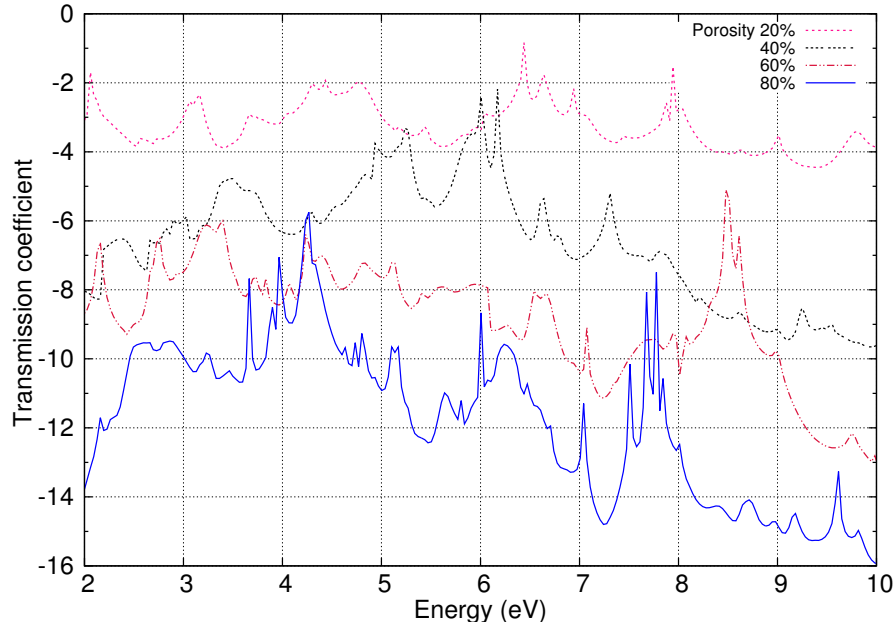


Figure 10.8. Average transmission spectrum (in logarithmic scale) at $V=10V$ of structures composed of 5 blocks. Different curves are shown for different values of porosity (number of dots/ total number of blocks). Averaging is performed over more than 100 configurations with dot and wire mean side $3nm$ and mean coupling parameters $\Gamma = 10^{-4}eV$. $U_0 = 0.01eV$.

10.3.2 Number of Blocks

We now discuss the effects of the number of blocks in a structure. Fig. 10.9 shows the average current-voltage characteristics of structures with different number of components and fixed porosity of 0.5. The mean wire/dot side is $3nm$ and the mean coupling parameter $\Gamma = 1e - 4eV$. As it can be seen, increasing the number of components, a smaller current flow is obtained. This is a direct consequence of the larger number of dots (at constant porosity), whose small density of states drastically hinders electron flow. When, on the contrary, quantum wires are inserted into the structure and the porosity is varied, a weaker decrease of current is found thanks to the wider energy support of their density of states. Differently from the dots' case, the 1D DOS provides more viable energy channels allowing a larger number

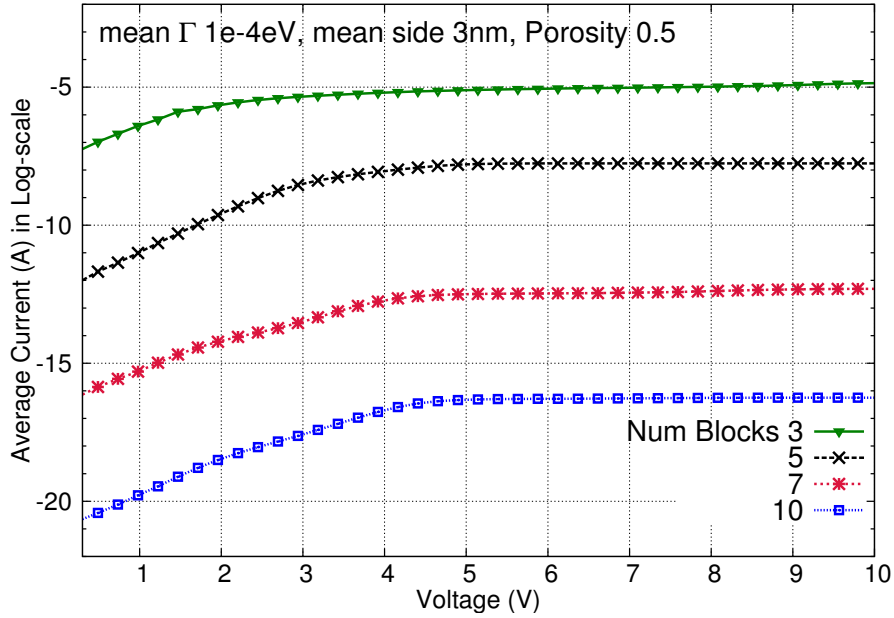


Figure 10.9. Average current - voltage characteristics (in logarithmic scale) of structures with different number of blocks. Porosity is kept fixed at 0.5. Averaging is performed over more than 100 configurations with dot and wire mean side $3nm$ and mean coupling parameters $\Gamma = 10^{-4}eV$. $U_0 = 0.01eV$.

of electrons to cross the structure. This can be seen from figure 10.10 showing the average current at $V=10V$ for different number of blocks and porosity. When dots are added to the structure, with a consequent increase of the number of blocks and porosity, a considerable decrease of current is found. On the contrary, if wires are inserted into the sequence, thus increasing the number of blocks and reducing the porosity of the structure, a smaller modification of current is devised.

10.3.3 Geometrical Parameters

This last section is devoted to the impact of the geometrical parameters of the 1D-0D sequence on the transport properties. In particular, the mean side of the cross-section of the quantum crystals and quantum wires is varied, thus obtaining different strengths of potential confinement inside the blocks. Analogously, we analyse the effect of changing the mean coupling parameters among the blocks, physically corresponding to modifying their relative inter-distances.

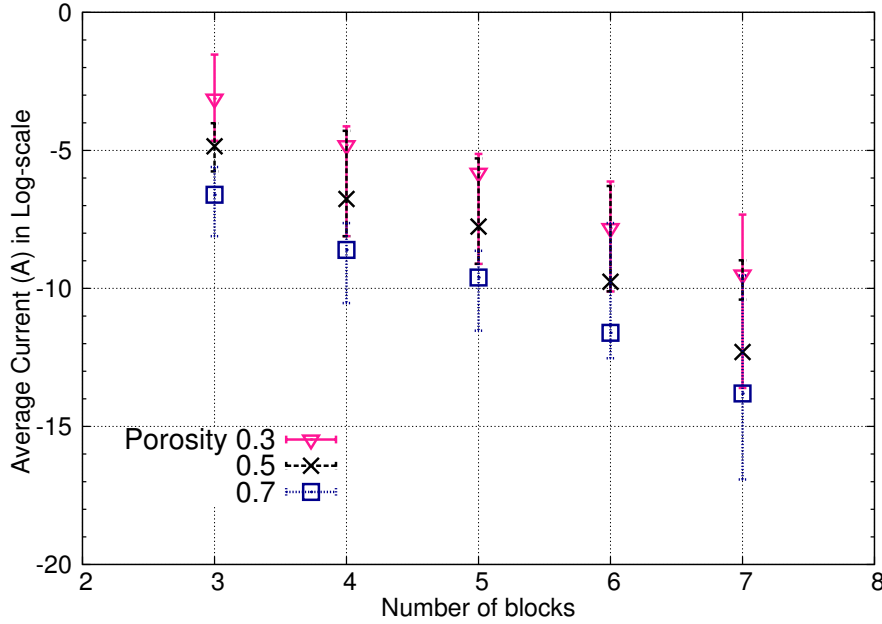


Figure 10.10. Average current with errorbars (in logarithmic scale) at $V=10V$ of structures with varying number of blocks. Different curves are shown for different values of porosity (number of dots/ total number of blocks). Averaging is performed over more than 100 configurations with dot and wire mean side $3nm$ and mean coupling parameters $\Gamma = 10^{-4}eV$. $U_0 = 0.01eV$.

Block Side

A modification of the cross-section dimension of a quantum dot or a quantum wire leads to a widening or shrinking of the potential confinement inside the block with a consequent change in the position of the energy levels/bands in its transmission coefficient (formulas 9.7 and 9.10). A similar effect is expected to occur in longer structures composed of several dots and wires when modifying the blocks' dimensions. Fig.10.11 shows the average transmission spectrum (averaged over more than 100 structure configurations) for different values of the side of dots and wires. Each structure is made of six blocks, whose sides are randomly chosen according to a gaussian distribution with different mean value (the standard deviation has been chosen to be $1nm$). Our expectations are confirmed by the gradual shift towards higher energies of the transmission spectra for smaller values of the side. Moreover, for sufficiently high energies the differences among the different transmission spectra of fig.10.11 drastically reduce (the plot is in log-scale), due to the general increase of the density of states of the blocks with energy.

The modification of the transmission spectrum stemming from a variation in the dimensions of the blocks engenders perceivable effects also on the conductance of

the whole structure. In fig.10.12 the average conductance of the same structures of fig.10.11 is depicted. Smaller sides determine a lower conductance due to a smaller density of states in the low-energy spectrum. On the contrary, increasing the dimensions, the conductance is seen to dramatically increase. Besides, the positions of the maximum of conductance of fig.10.12 shift to lower energies for larger sides, thus assessing the strong influence exerted on the transport properties in a long sequence by the dimensions of its individual components.

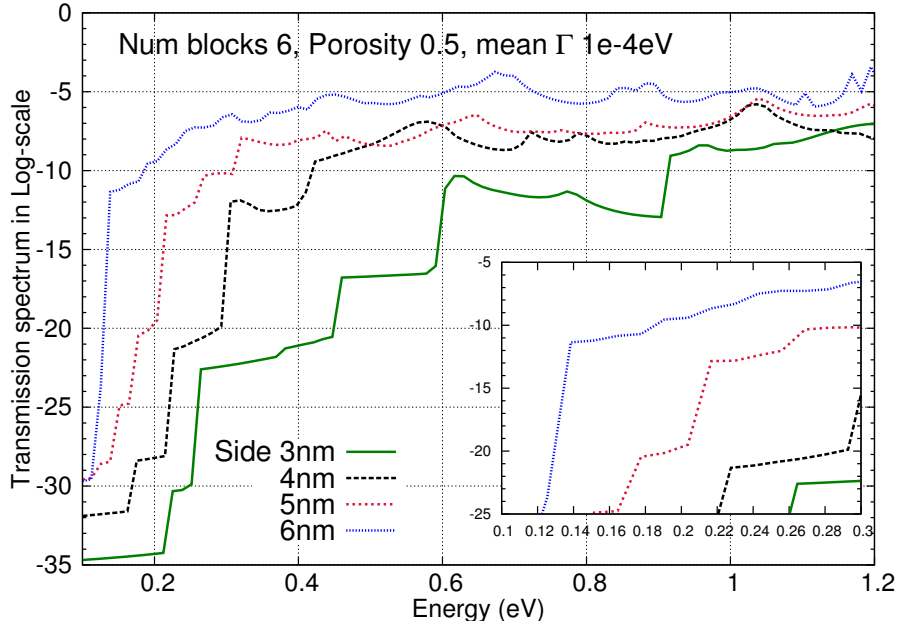


Figure 10.11. Average transmission spectra (in logarithmic scale) of structures with varying mean block side. Averaging is performed over more than 100 configurations with mean coupling parameters $\Gamma = 10^{-4}eV$. $U_0 = 0.01eV$.

Coupling Parameters

The distance among the blocks plays a fundamental role in the transport properties of the structure. In the model adopted in this work, this parameter is taken into account through the values of Γ 's entering in the transmission spectrum and current relations (expressions 9.8 and 9.9 above). In particular, making two dots closer to each other determines a larger probability for an electron to cross the structure in a finite time and consequently determines a wider uncertainty in the energy levels of the system (cit. Datta). The widening of the energy peaks is ultimately responsible for a greater overlap among energy levels of adjacent blocks and a larger density of states for the overall system is found. The conductance of the system grows as well as Fig. 10.13 confirms. In it the average conductance (over a sample of

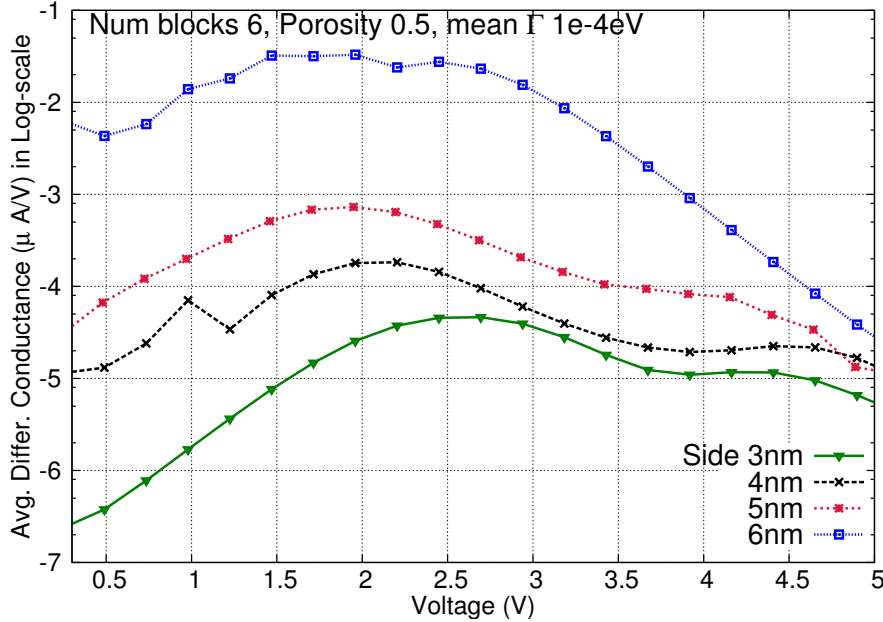


Figure 10.12. Average differential conductance of structures of structures with varying mean block side. Averaging is performed over more than 100 configurations with mean coupling parameters $\Gamma = 10^{-4}eV$. $U_0 = 0.01eV$.

more than 100 structures) is shown. The individual sequences count six blocks with mean side of $3nm$ while their right and left coupling parameters are chosen randomly from a gaussian probability distribution with standard deviation $10^{-4}eV$ and variable mean value in the range $[10^{-4}, 10^{-3}]eV$. This interval of parameters Γ corresponds to inter-block distances in the interval $[1, 4]nm$ as the results of the simulation process of section 10.2 showed. Moreover, all the curves show a maximum in the same energy range, due to the presence of numerous peaks in that portion of energy spectrum, having the structures the same average side dimension.

10.4 Conclusion

Recent advances in fabrication processes have allowed the embedding of low-dimensional structures (quantum dots and wires) in the same device giving birth to new device families structures with interesting electrical properties. However, the control on the accuracy of the geometrical parameters of their components is usually poor, thus making it difficult to fully understand the underlying mechanism of transport. Hence, in the last chapters we presented a model to study electron transport properties in 1D random structures composed by a sequence of quantum dots and wires. Based on the transfer matrix formalism, it fully accounts for the coherent nature of

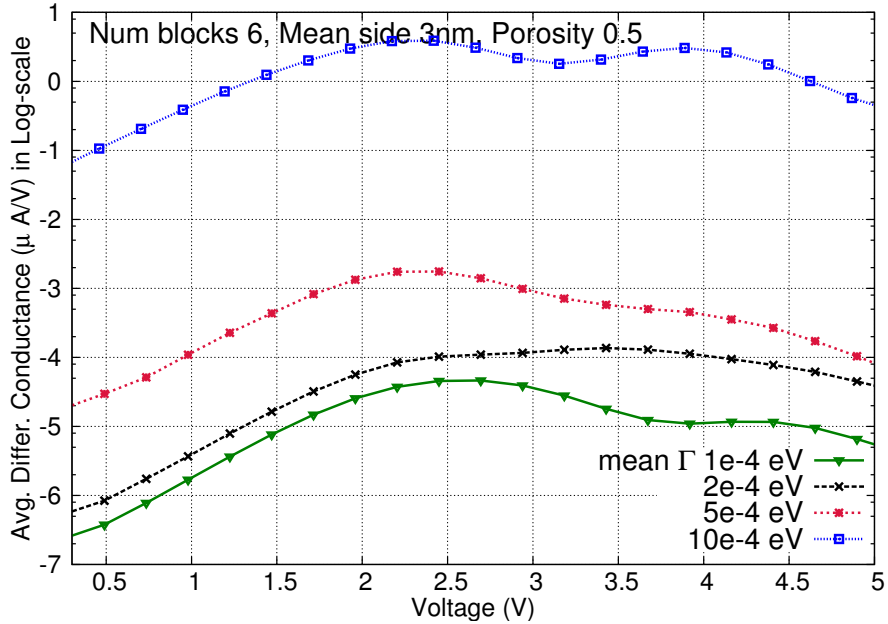


Figure 10.13. Average differential conductance of structures (six blocks) with varying mean coupling parameters. Averaging is performed over more than 100 configurations with mean side $3nm$; $U_0 = 0.01eV$.

transport and proves to be scalable with the dimensions of the device. Its validity has been demonstrated through a comparison procedure with the results of a NEGF tool in a quantum simulator obtaining excellent agreement.

We then exploited the envisioned technique to systematically analyse the electron transport properties of porous silicon nanowires, described as successions of silicon nanocrystals (dots) and nanowires with random geometrical parameters. A statistical study has been performed by varying general features of the structure: the number of constituting blocks, the porosity of the structure, the mean side of the blocks and the coupling parameters among them.

In particular, we demonstrated how increasing the number of quantum dots in a fixed-length device, hence for larger porosity, the transmission spectrum and consequently the current reduce exponentially due to the reduced density of states available in the silicon nanocrystals. A similar exponential decay in current has been obtained for larger structures: the level of porosity determines here the decay rate with the number of blocks. Finally, we proved how a modification in the mean side of the components block causes a change in the transmission spectrum and conductance. As expected, an increase in the average dimensions of the blocks, lowers the bottom band in the transmission coefficient consequently engendering an increase in conductance. Increases of a few order of magnitude are found for sides $1nm$ wider. Also, the coupling parameters have been demonstrated to play a pivotal role in the

structure here investigated. Increasing the coupling strength, which corresponds to smaller distances among the blocks, facilitates conduction with increases of some orders of magnitude in the overall conductance.

SINWs for COMPUTATION

**Multiple Independent-Gate
Transistors:**
Modelling & Simulation

SINWs for SENSING

Porous Silicon NWs:
Fabrication & Modelling

Surface Interaction:
Ab-initio & Macroscopic
simulations

Chapter 11

Ab-initio simulations

11.1 Introduction

This chapter marks the beginning of the last part of this thesis work devoted to the study of the effects on silicon nanowires conduction due to the interaction with a surface material. In the preceding pages we highlighted the relevance of silicon nanowires in sensing applications. In particular, Porous Silicon Nanowires, thanks to their high surface- to-volume ratio, were investigated deeply from a technological viewpoint and the subsequent modelling problem was tackled. However, there is still a fundamental problem to be analysed in order to fully understand the working principles of SINWs as sensors: how the adsorption of molecules modifies the electron transport properties and how these changes can be exploited for chemical species detection. This problem is indeed not new. Several studies have been conducted to analyse structural and electronic properties of SiNWs theoretically or from ab-initio calculations [62, 179]. Their goal was, on one side, to determine the band structure of pristine nanowires; from this, the band-gap has been numerically derived for different diameters and growing directions [180]. On the other side, studies can be found in literature analysing the effects of random dopants and impurities bonded on the wire surface. The corresponding transmission and conductance are computed [182, 183]. Results showed an increase of the energy-gap for smaller diameters due to quantum effects. In addition, they highlighted the possibility of tuning the bandgap attaching gas molecules, like Hydrogen, OH and NH_2 groups, on the surface of the silicon wire [182, 181, 180].

These results are the outcome of the study of wires with a cross section counting a very limited number of atomic layers and, consequently, with diameters smaller than 2 nm. In this range of geometrical dimensions, ab-initio simulations represent the most accurate tools to get information from first principles physics. However, such atomistic approaches become soon unaffordable for larger dimensions, when

the number of atoms in the system exceeds a few hundred units. The limitations of their applicability simply reside in the huge computational cost in terms of time and memory employed [180].

As a consequence, the employment of semiconducting nanowires in electronics and sensing applications with diameters larger than 2 nm poses the study of electron transport in these devices under the attention of both theoreticians and engineers. Although it is expected that quantum confinement effects and interaction with surface materials affect conduction in larger structures as well, in the authors knowledge no systematic study has been presented yet in the literature. Information on the properties of transmission and conductivity in silicon nanowires with diameters larger than a few nanometers would invaluablely help understanding the theoretical foundations of their transport properties. In addition, the analysis of the effects of many impurities interacting on the surface of the wires would allow an eventual assessment of their performance in real gas sensing applications orienting the subsequent design flow.

In this chapter we will present the main results of the analysis of the electronic structure of silicon surface conducted via Siesta DFT package at *Institut de Ciència de Materials de Barcelona (ICMAB-CSIC)* to get an insight on the unmissable features of the adsorption properties of silicon nanowires. The systems we analysed through ab-initio approach are definitely small (they have less than 150 atoms) but were sufficient to derive some general and fruitful information to be exported on simulations of much larger size.

The next chapter will complete the analysis started here: the useful information uncovered will be practically exploited in a thorough analysis of the currently used silicon nanowires' conduction in presence of a surface interacting layer.

11.2 Methods

We perform first-principles electronic structure calculation within density-functional theory (DFT), as implemented in the Siesta package [194]. An overview of DFT method is presented in the appendix. We use norm-conserving pseudopotentials for the core electrons and an optimized single- ζ basis set plus polarization functions [195] for the valence electrons. The exchange-correlation energy is calculated within the spin polarized generalized gradient approximation (GGA) in the parametrization of Perdew-Burke-Ernzerhof [196].

We model the SiNW/meso-PSi surfaces with a Si(111) 3×3 surface. We use a 4×4 supercell of the surface unit cell in slab geometry, sampling the Brillouin zone with a grid of 4×4 of k-points within the Monkhorst-Pack algorithm [197].

The bottom dangling bonds are passivated with hydrogen atoms. All the structures discussed have been relaxed until the all the forces on the atoms were lower than

0.04 eV/Å.

The surface unit cell is made of more than 100 atoms, the right number of atoms depending on the proper passivation (if present) of the upper dangling bonds. We performed calculations on

- Surface passivated with Hydrogen
- Pristine surface, with upper silicon atoms not passivated
- Upper surface Hydrogen-passivated with a dangling bond saturated with a SO₂ molecule
- Upper surface Hydrogen-passivated with a dangling bond saturated with a NO₂ molecule

For the cases mentioned, we relaxed the structures, calculated the electronic structure and, eventually the projected density of states. The results will be presented in the next section together with a discussion on the different data found.

11.3 Results

11.3.1 Hydrogen-passivated Surface

We start presenting the results of a Pristine Silicon surface whose surface dangling bonds have been filled with Hydrogen-atoms. The importance of passivated surfaces and consequently passivated nanowires resides in the fact that they are more predictable because they are always semiconducting. On the contrary non-passivated nanowires have been shown to change dramatically their properties depending on the dimensions of the wire, their orientation, ... For this reason, passivated NWs are expected to play an important role in the next generation of electronic devices. Yet, the surface has a relevant role that merits some considerations.

Fig. 11.1 shows the unit cell of passivated surface we simulated through Siesta DFT package. As it can be seen, all the silicon atoms lying at the bottom and upper surface form bonds with Hydrogen atoms. The band-diagram of this structure is plotted in fig. 11.2. Conduction and valence bands are separated by a direct energy-gap of the order of 1eV and hence a semiconducting behaviour is expected. The calculated energy per atom in the system is $-94.28\text{eV}/\text{atom}$. This value which represents our reference value for the following situations analysed.

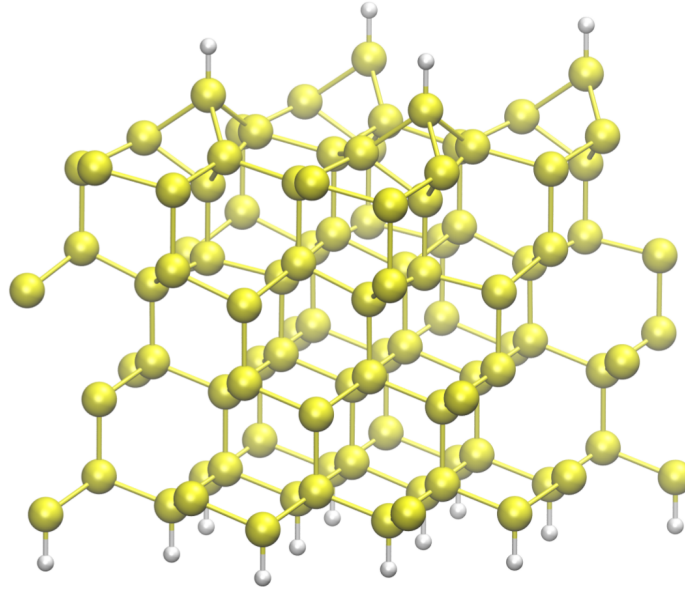


Figure 11.1. Unit cell of the H-passivated silicon surface. Yellow - Silicon atoms, White - Hydrogen atoms

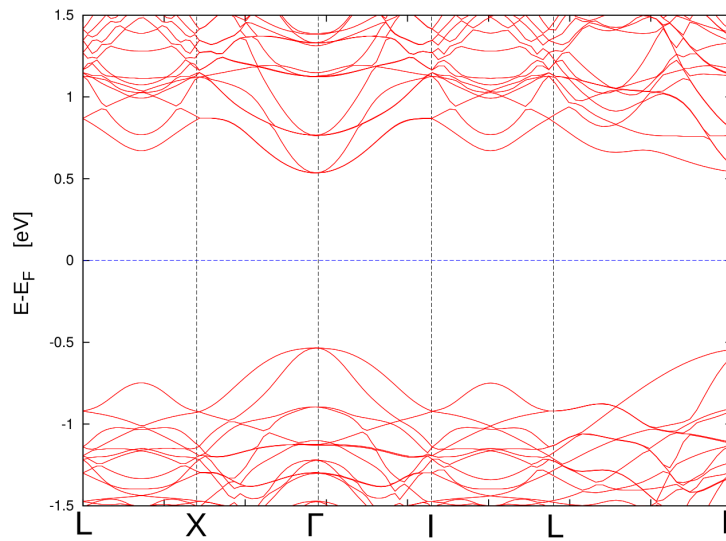


Figure 11.2. Band-diagram of the H-passivated silicon surface. Direct band-gap of 1eV is found. The blue dotted line represents the Fermi Energy.

11.3.2 Non-passivated surface

Nanowires with non-passivated surface turned out to have a limited relevance, at least to date, because experimentally grown SiNWs are always passivated. However, the study of bare unpassivated wires is still interesting for two reasons: a) it leads to the conclusion that passivation is essential to obtain nanowires with predictable and easy to control electrical properties and b) it sheds a light on some atomic-scale mechanisms of fundamental interest. The atomic relaxation of the surface led to a value of total energy per atom of -93.89eV , a value smaller compared with the H-passivated case, thus revealing a less stable configuration of the wire in absence of passivating Hydrogen.

The band-diagram of this structure is depicted in fig. 11.3 conduction and valence bands can be easily identified with a direct band-gap of about 1eV . Moreover, two energy levels are present in the band-gap (the blue dotted line corresponds to the Fermi Energy). The lowest of them lies below E_F and it is actually populated at the thermodynamical equilibrium. On the contrary, the other one has an energy higher than E_F and is not populated. Another important remark is in order at this point. The calculations we performed take into account the spin-polarization of the electrons in the system. The effects of this can be actually perceived especially in systems with an odd number of electrons. This is the case we are facing. What is found is that the lowest energy level in the band-gap belongs to the density of states of spin-up electrons, the highest belongs to the density of spin-down electrons. More importantly, the arise of spurious energy levels in the band-gap reveals the high chemical reactivity of the non-passivated silicon surface.

11.3.3 H-passivated surface with SO_2 molecules

Fig. 11.4 represents a portion of surface where a substitution of a Hydrogen has been performed with a SO_2 molecule. The corresponding band-diagram is depicted in fig. 11.5 the band-diagram is almost identical to the H-passivated case made exception for two new discrete energy levels falling in the energy-gap. In a very analogous way with respect to the non-passivated wire, the odd number of electrons in the structure leads to a spin-splitting of these spurious energy levels, one of which is occupied in the ground-state configuration of the system, the other is empty.

To better understand the properties of the newly arisen energy levels, we calculate the so-called Projected density of states (PDOS), given by the projection of the DOS onto the localised orbitals of the interesting chemical species. In our case we computed the PDOS on S and O atoms to uncover the spatial distribution of the corresponding energy states. From fig. 11.6 it can be evinced that the energy levels in the band-gap are strongly localised on the SO_2 molecule and consequently do not contribute to current. Another equivalent manner to see the same is to look

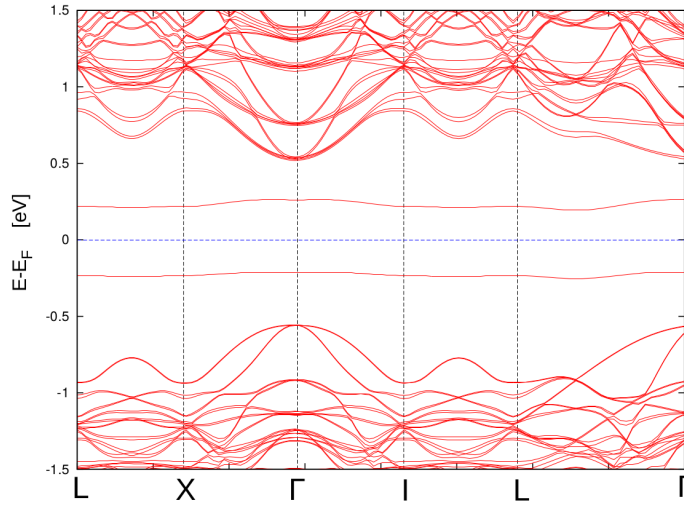


Figure 11.3. Band-diagram of the non-passivated silicon surface. Direct band-gap of 1eV is found with two discrete energy levels in the band-gap. The blue dotted line represents the Fermi Energy.

directly at the eigenfunctions in their spatial representations and see where there is the highest probability of finding the electron. The lowest wavefunction (the other is very similar) is shown in fig.11.7 the image confirms the preceding discussion on the localisation of the spurious energy states on the SO_2 molecule.

Before going over and consider the case of NO_2 molecules, it is important now to remark that the localised nature of the eigenstates inside the band-gap is actually responsible of the formation of a non-zero charge density along the surface of the wire. Its value strongly depends on the type of molecule interacting with surface silicon. The presence of some charge on the SiNWs is of pivotal importance for the following of this thesis work: it actually represents a linking bridge between *ab-initio* calculations (affordable for very small structures) and macroscopic simulations (which are not capable of studying the atomistic character of surface atoms interactions). We will indeed exploit this information to carry more extensive analysis in the next chapter.

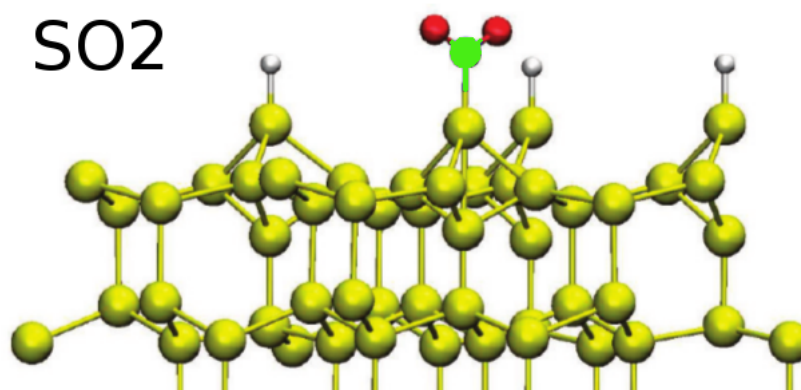


Figure 11.4. Unit cell of the H-passivated silicon surface with SO₂ molecule. Yellow - Silicon atoms, White - Hydrogen atoms, Red - Oxygen, Green - Sulphur.

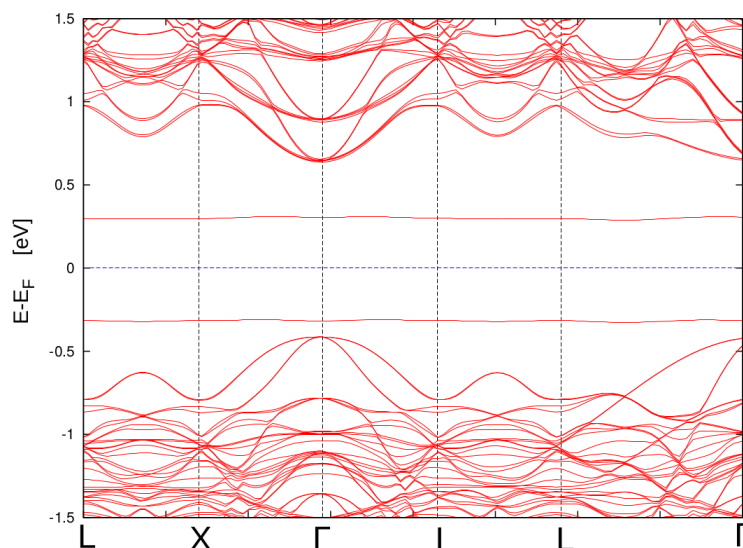


Figure 11.5. Band-diagram of the passivated silicon surface with SO₂ molecule. Direct band-gap of 1 eV is found with two discrete energy levels in the band-gap. The blue dotted line represents the Fermi Energy.

11.3.4 H-passivated surface with NO₂ molecules

From the previous section we understood that the interaction of silicon surface atoms with other molecules can lead to a modification of the band-diagram through the formation of new localised energy levels. Their position in the energy spectrum

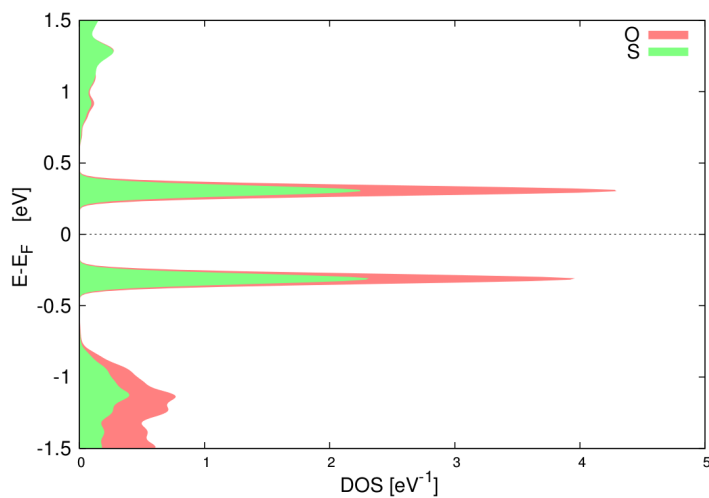


Figure 11.6. PDOS on S and O atoms in the passivated silicon surface with SO_2 molecule. The peaks in the band-gap correspond to the discrete energy levels discussed in the text and reveal the localised nature of the corresponding states.

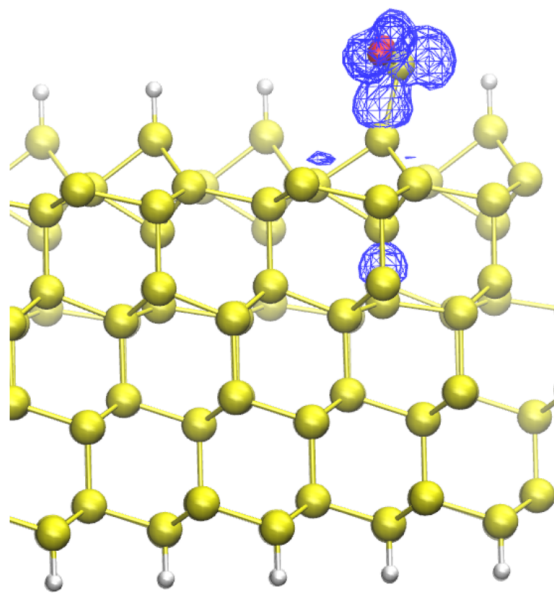


Figure 11.7. Spatial distribution of the wavefunction corresponding to the lowest energy level in the band-gap. In blue the isosurface of the wavefunction modulus.

is a peculiar feature of the molecules considered, as we would like to convey in this section.

The case of silicon surface interacting with NO_2 molecules is now treated. Our interest is again focused on the band-diagram of the structure which is shown in fig. 11.8. What can be immediately noticed is the absence of the energy levels which were engendered in the previous case. In our current situation it seems that the interaction of silicon surface with NO_2 molecules leaves almost unaltered the electronic structure of the system. However, a more careful analysis reveals that there are strong modifications in the band diagram even in this case. Fig. 11.9 shows the partial density of states over Nitrogen and Oxygen atoms as a function of energy. In a strict analogy with the SO_2 case, the presence of NO_2 engenders new energy states whose energy falls in the valence and conduction band. Moreover, they are still localised on the molecule (peaks in the PDOS).

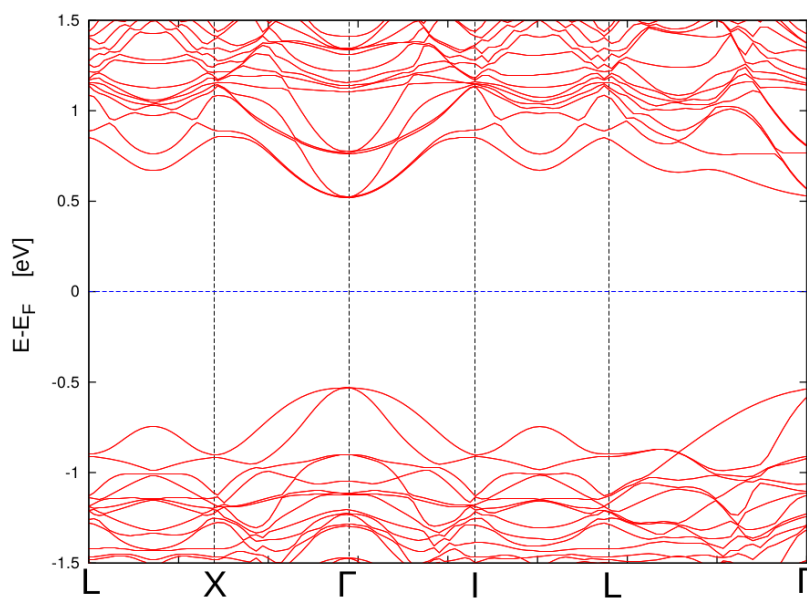


Figure 11.8. Band-diagram of the passivated silicon surface with NO_2 molecule. Direct band-gap of 1eV is found but no discrete energy levels in the band-gap. The blue dotted line represents the Fermi Energy.

11.4 Conclusions

In this chapter we presented the main results of ab-initio calculations we performed on silicon surfaces when some interaction is inserted. In particular, we showed

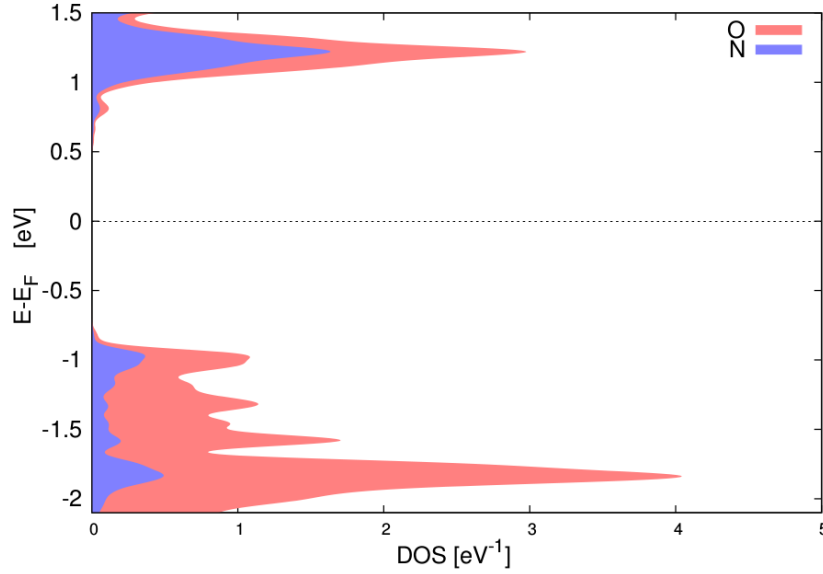


Figure 11.9. PDOS on N and O atoms in the passivated silicon surface with NO_2 molecule. The peaks in the band-gap correspond to the discrete energy levels discussed in the text and reveal the localised nature of the corresponding states.

how interaction with some surface molecule can cause strong modifications in the electronic structure of a wire: new discrete energy levels arise which can fall in the energy-gap, as in the SO_2 case, or not. Their energies varie with the type of molecules and this represents a distinctive sign of a the adsorption of a specific chemical compound.

Moreover, these new energy states are localised on the molecules, as the calculations of PDOS revealed. As a consequence, the population of these states by electrons brings a non-zero charge density on the surface which modifies transport in the wire. This information will be largely exploited in the following chapter in order to analyse the transport in silicon wires with dimensions too large to be simulated via DFT package tools.

Chapter 12

Analysis of Surface Interaction

As already mentioned in the previous chapter, the employment of semiconducting nanowires in electronics and sensing applications with diameters larger than 2 nm poses the study of electron transport in these devices under the attention of both theoreticians and engineers. Information on the properties of transmission and conductivity in silicon nanowires with diameters larger than a few nanometers would invaluablely help understanding the theoretical foundations of their transport properties. In addition, the analysis of the effects of many impurities interacting on the surface of the wires would allow an eventual assessment of their performance in real gas sensing applications orienting the subsequent design flow.

Starting from the main results of the *ab-initio* analysis conducted on silicon surface, we try to systematically analyse the conduction properties of larger wires for which an atomistic approach is not feasible. In particular, in this chapter we propose 1) a thorough analysis of the electronic properties of a silicon nanowire interacting with a surface material with different electrical and geometrical properties. The study has been performed focusing on the impact on transmission spectrum and current. 2) We demonstrate that the properties of the surface material (permittivity, thickness) affect electron transport in the wire changing the confining potential in the channel and the corresponding transmission spectrum. Maximum relative changes in current of 20% and 50% are found for permittivity and thickness respectively. 3) The impact of a surface charge concentration and of a varying density of surface material on the current is examined and discussed. Specifically, we present results confirming relevant modifications of the order of 50% in the resulting current when varying the percentage of channel covering. We conclude analysing 4) the effect on electron transport due to the multiple interaction of silicon nanowires with two different surface materials. We eventually show interesting interdependence effects arising in the transmission spectrum which highlight new peculiar phenomena in silicon nanowires for sensing applications.

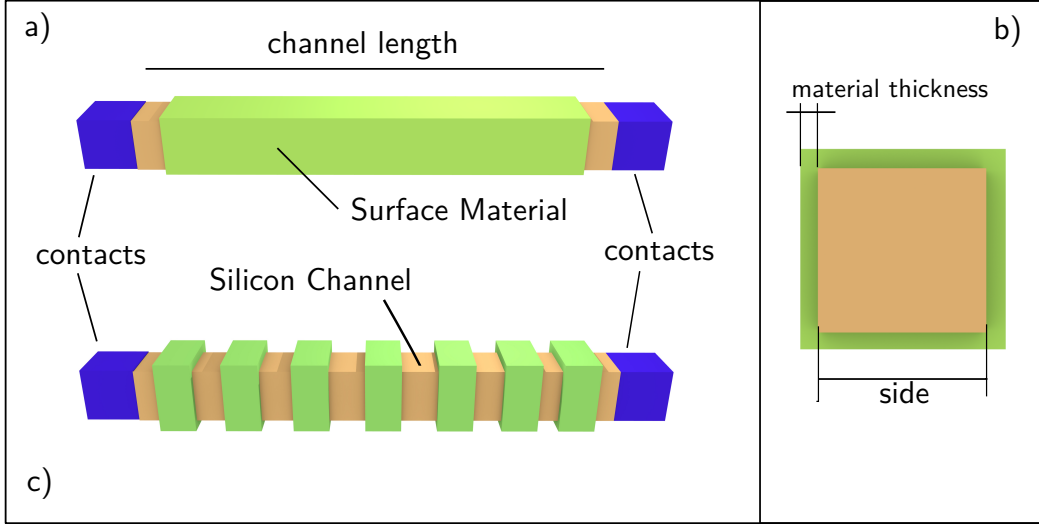


Figure 12.1. a) Scheme of the investigated Silicon Nanowire partially covered with some surface material; b) Cross section of the SiNW.

12.1 Methods

The device we adopted for our systematic analysis of transport properties is a silicon nanowire aligned along $[100]$ direction and characterized by a square cross-section (side = 3nm) with a 15nm length. Fig. 1-a shows schematically the whole structure, while fig.1-b depicts its transverse section. The channel is contacted with two highly doped contacts mimicking ideal carriers reservoirs. In the following sections, the surface of the wire will be fully or partially covered with a layer of a certain material, differing from silicon in its value of dielectric constant. Depending on the permittivity and on the layer thickness (ranging from 1\AA to 5\AA), the impact of quantum confinement is modified, allowing to treat a generic interface material. Moreover, we introduce a surface charge density between the silicon channel and the external layer to model the net charge densities which could arise from chemical bonds with molecules.

Calculations of transmission spectrum, density of states and current are performed via a self-consistent solution of the coupled Schrodinger and Poisson equations [127]. Specifically, Schrodinger equation with an effective Hamiltonian is solved under the assumption of Effective Mass Approximation (EMA). Stated in another way, we assume that the dimensions of the wires are sufficiently long for the EMA to hold. Hence, values of the effective masses adopted are those of bulk silicon (longitudinal mass of $0.190m_0$ in unprimed subbands, $0.916m_0$ in primed subbands).

Calculations of current are instead performed in the Landauer-Buttiker formalism starting from the transmission spectrum previously computed.

12.2 Results

We present now the results of the systematic analysis we performed on the device described above. Parametric study of transmission spectrum and current has been conducted in terms of four parameters: a) charge density at the interface between the channel and the surface layer, b) thickness of the surface layer, c) permittivity of the surface material and d) percentage of the channel covered by the surface material. We conclude describing e) the impact on conduction transport due to the interaction of silicon nanowires with different surface materials.

Interface charge density

The interaction between the silicon channel and the external layer manifests itself microscopically through the formation of molecular bonds among the silicon atoms on the surface and the adjacent compounds attached to the wire. Depending on the molecular species involved, these bonds determine a redistribution of charge in the structure and a generally non-negligible amount of charge is found on the surface of the silicon wire. The inset of fig. 12.2 shows the electron density, derived via *ab-initio* calculations [185], along the surface layer of Hydrogen atoms in a passivated silicon nanowire. A charge density of 3 electron charges per \AA^2 is present in proximity of the Hydrogen atoms (red regions).

The presence of a surface charge density between the channel and external layer alters the confining potential as well. A positive charge density effectively lowers the potential barrier, while a negative one restricts it, thanks to the attractive and repulsive electrostatic forces on the electrons respectively. The effect of charge density can be modelled through an effective modification of the side W:

$$W_{eff} = W + \alpha_\rho \cdot \rho \quad (12.1)$$

where α_ρ is a positive parameter introduced to model the effect while ρ is the surface charge density. Depending on the sign of ρ , an effective increase or decrease of the side is obtained. Assuming then a simple quantum-well behaviour for the confining potential in a transverse section of the wire, the lowest conduction band energy scales as

$$E_C \propto \frac{1}{W_{eff}^2} = \frac{1}{(W + \alpha_\rho \cdot \rho)^2} \quad (12.2)$$

From eq.(2) it emerges how a positive charge density determines a lowering of the conduction band while a negative one causes its raising in energy. Consequently, an

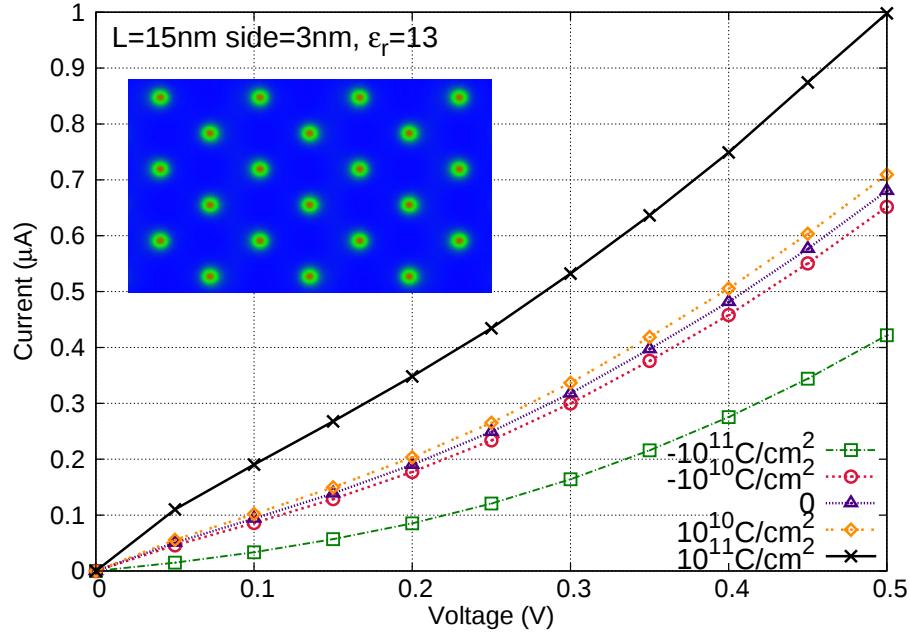


Figure 12.2. Current-voltage curves of a silicon nanowire (side 3nm) for different values of charge density on the surface between the channel and the external layer. In the inset the electron density along the external layer of Hydrogen atoms of a passivated silicon nanowire is shown; red regions denote higher density. Data are extracted using the atomistic simulator VNL ATK [185].

increase and a decrease of current is expected in the two cases, respectively. The confirmation is shown in Fig.2 where the current-voltage characteristic of a silicon nanowire (side 3nm) is depicted.

The confining effect exerted by the surface charge density, moreover, strongly depends on the transverse dimension of the silicon nanowire. For large values of side, the relative change in the confining potential is expected to be smaller with a consequent smaller sensitivity of the current with the charge density.

In this respect, Fig. 12.3 depicts the current-voltage characteristics for a silicon nanowire with a side of 6nm in the same charge density conditions of fig.12.2. A lower relative change in current with density is found with respect to the smallest nanowire. Values of relative change in current are 43% and 14.2% with $\rho = 10^{11} \text{ C/cm}^2$, $V = 0.5 \text{ V}$ for sides of 3nm and 6nm, respectively.

Thickness of the surface layer

When a chemical specie interacts with the surface atoms of a silicon nanowire or a layer of a certain material is deposited on its surface, the conduction properties of

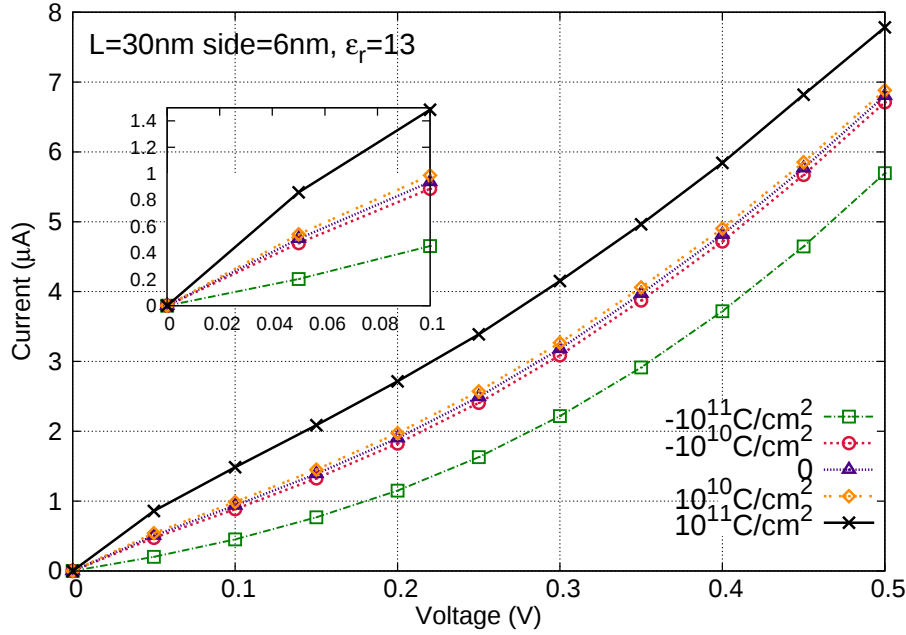


Figure 12.3. Current-voltage characteristics of a silicon nanowire for different surface charge density. Nanowire side 6nm.

the wire are expected to modify. Geometrical parameters of the surface layer are found to play a determinant role in this respect. In particular, the thickness of the material surface can be easily identified as one of them.

Fig.12.4 shows the current of the simulated Silicon Nanowire (length $15nm$, side $3nm$) for different values of thickness of the surface material ($\epsilon_r = 4$). For increasing thickness, a higher current is detected revealing a higher conductivity of the wire. The explanation resides into the weaker confinement effect exerted by a sufficiently thick layer; this effectively widens the quantum well profile in the transverse direction with a consequent lowering of the conduction energy band in the channel. The corresponding transmission spectrum confirms the phenomenon. In Fig.12.5 the transmission spectrum of the wire is displayed for different values of thickness of the layer material ($\epsilon_r = 4$). As expected, a reduction of the minimum energy of the conduction band is found.

Permittivity of the surface material

In this section we analyse the effects of the permittivity of the surface material on the conduction properties of a silicon nanowire. Simulations have been performed on a nanowire with squared section of side $W = 3nm$ and length $15nm$. A surface layer of varying permittivity (ϵ_r ranging from 3 to 15) and thickness 3\AA is juxtaposed on

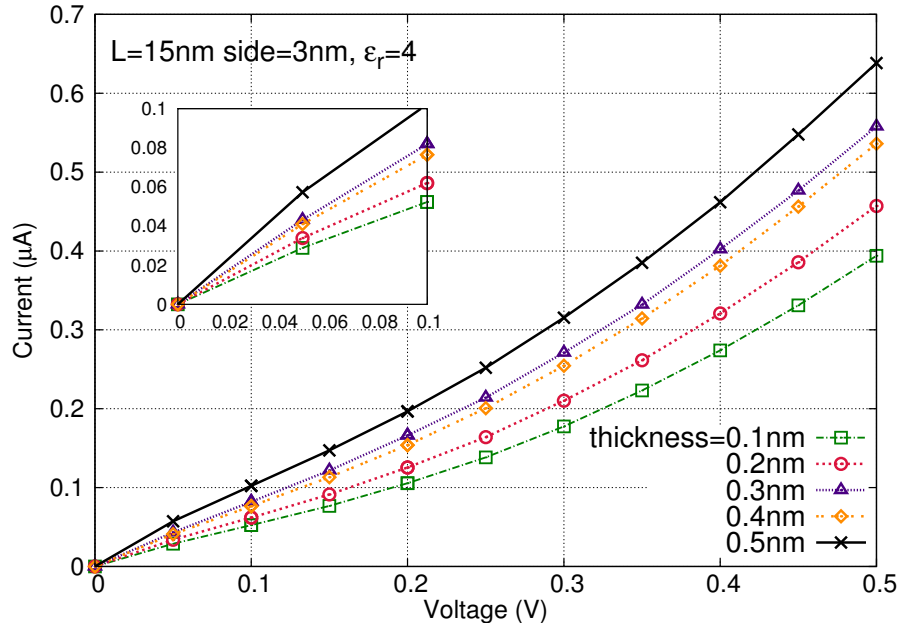


Figure 12.4. Current-voltage characteristics of a silicon nanowire for varying surface layer thickness, $\epsilon_r = 4$

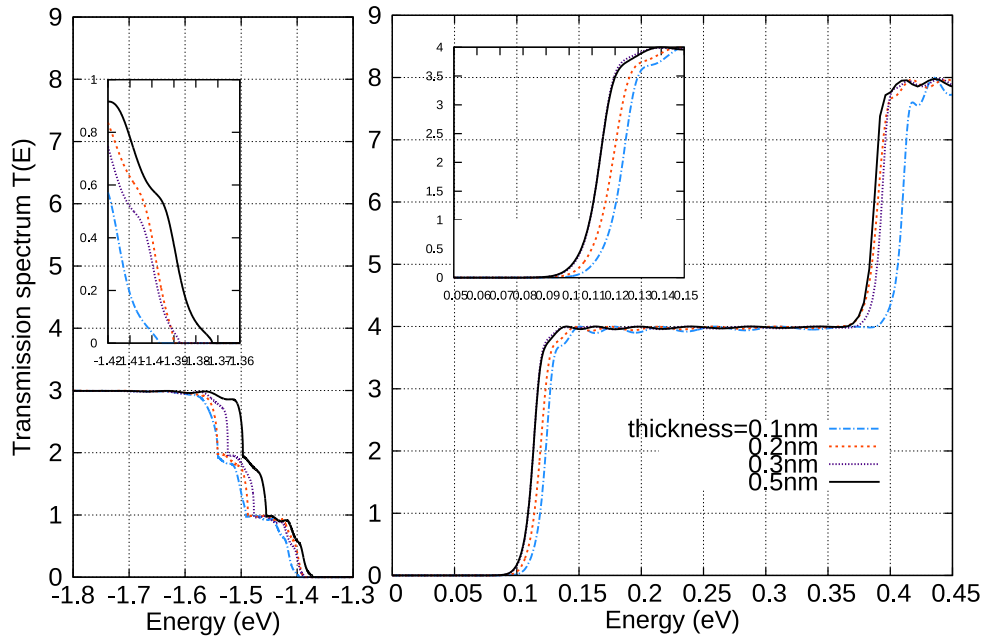


Figure 12.5. Transmission spectrum of a silicon nanowire for varying surface layer thickness, $\epsilon_r = 4$

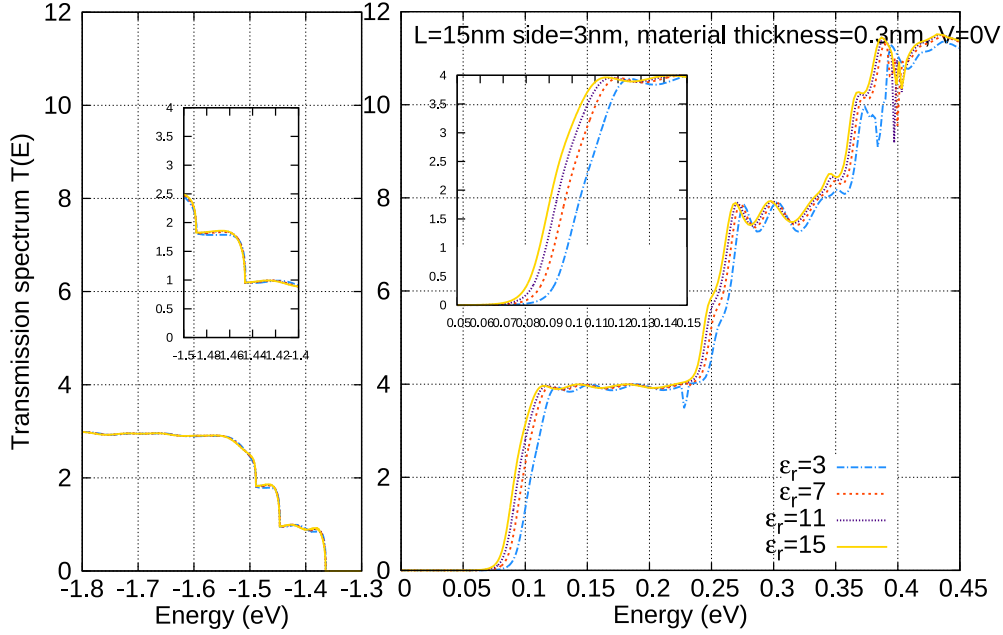


Figure 12.6. Transmission spectra of a silicon nanowire for different permittivities of the surface material (oxide thickness=3Å)

the lateral faces of the wire, whose transmission spectrum at equilibrium is depicted in fig. 12.6.

As it can be easily noticed, an increase in the permittivity of the surface layer provokes a reduction of the energy gap between conduction and valence bands revealing a different capability of the surface material in confining electrons in the channel.

A higher permittivity is, indeed, responsible for a slower variation of potential along a transverse section from its value in vacuum and the lower value in the silicon channel. The spatial region involved in this change of potential is then increased resulting in a wider confining potential. This reasoning is better clarified when looking at the transverse confinement potential along a cross section of the wire for three different values of permittivity (fig.12.7). A symmetry axis normal to the side of the square section has been chosen. Here the almost quantum-well potential is effectively widened by an increase of the permittivity of the surface layer.

In analogy with the previous sections, an analytical expression for the change in the energy difference between conduction and valence bands can be easily derived exploiting fundamental relations of quantum mechanics. Assuming a 2D quantum-well potential in the transverse section of the wire and an effective side of the wire given by

$$W_{eff} = W + \alpha_{\epsilon} \epsilon_r \cdot t \quad (12.3)$$

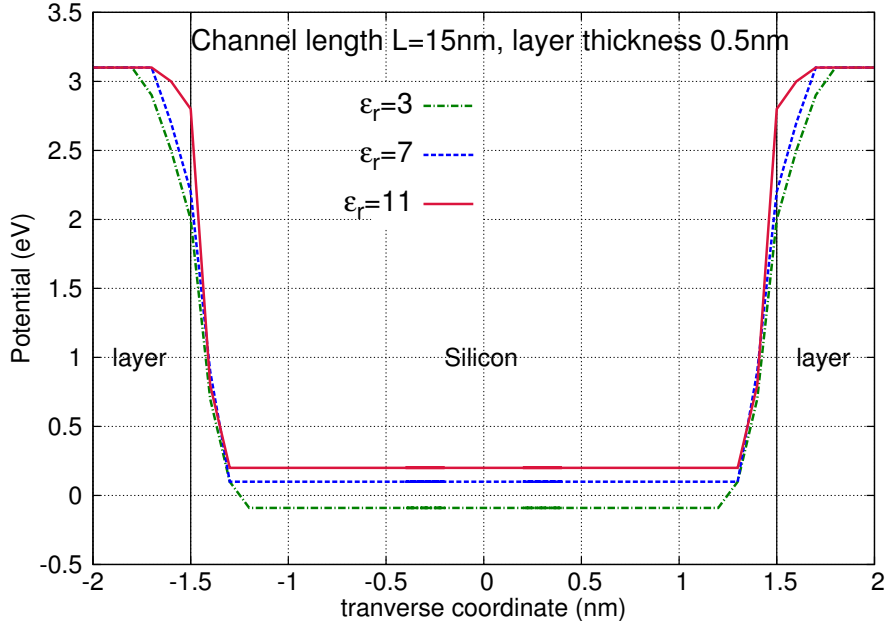


Figure 12.7. Confining potential profiles along an axis on a transverse section of a silicon nanowire (side $3nm$, length $15nm$). A Symmetry axis normal to a side has been chosen. A surface layer of thickness 5\AA covers the wire. Different curves correspond to different values of permittivity ϵ_r .

(α_ϵ is a parameter introduced to model the effect of permittivity on the widening potential, t is the layer thickness), the conduction-valence energy gap calculated with respect to the silicon bulk value ($E_{g,0} = 1.11eV$) is then found to scale as

$$E_g - E_{g,0} \propto \frac{1}{W_{eff}^2} = \frac{1}{(W + \alpha_\epsilon \epsilon_r t)^2} \quad (12.4)$$

The correctness of this behaviour is confirmed by the plot of fig.12.8 where the quantity $E_g - E_{g,0}$ is shown as a function of the side W for different values of ϵ_r . The lines are the fitting curves of eq. 12.4, points represent the simulation output. In fig. 12.9 the current-voltage characteristics are shown for different values of permittivity. In agreement with the preceding discussion, larger current can flow in the channel when increasing the permittivity due to the mentioned reduction of the energy interval between conduction and valence bands.

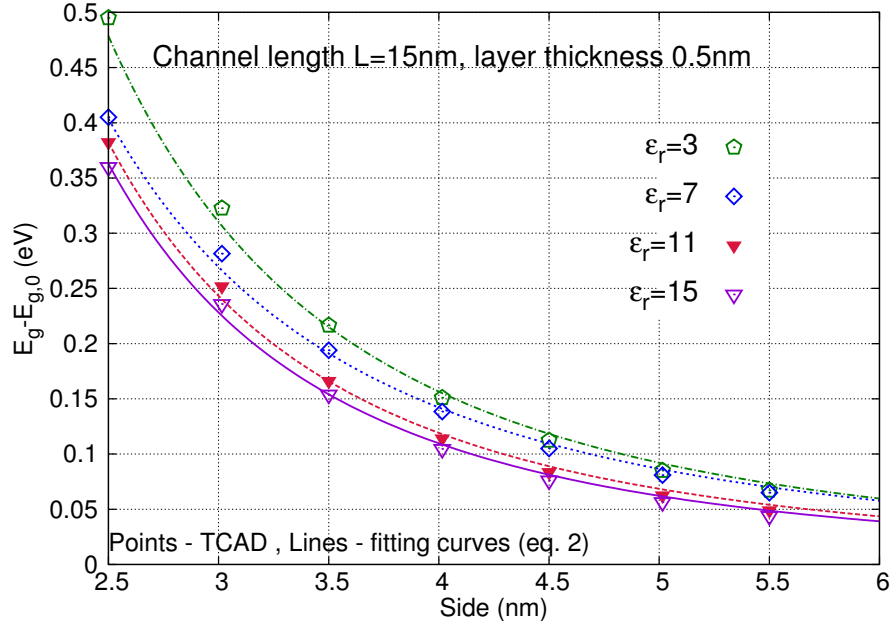


Figure 12.8. Energy difference between the conduction and valence bands vs. nanowire side is shown for different values of permittivity ϵ_r . Energies are shifted of the bulk silicon energy gap $E_{g,0} = 1.11\text{eV}$.

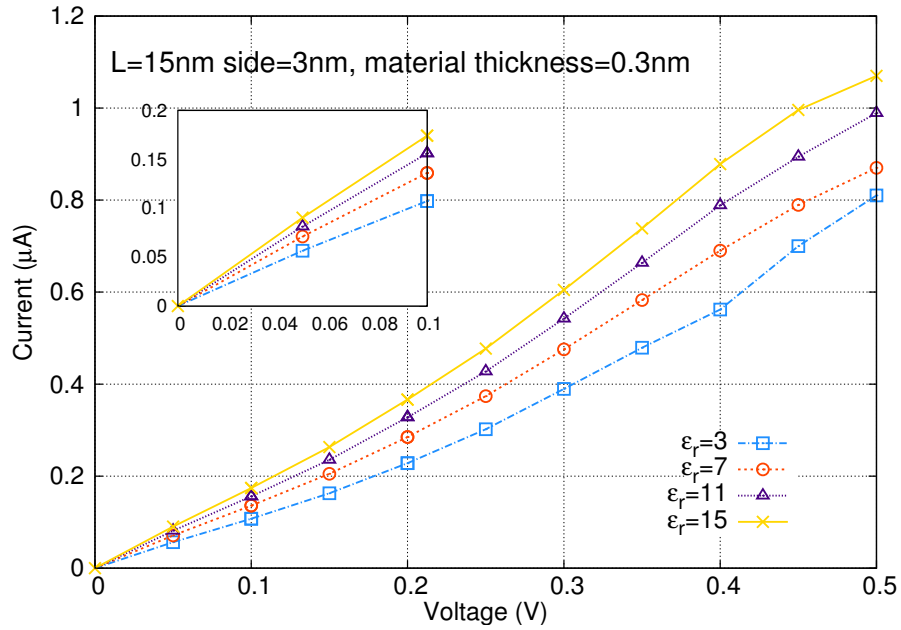


Figure 12.9. Current-voltage characteristics of a silicon nanowire for different values of surface material permittivity (oxide thickness=3Å).

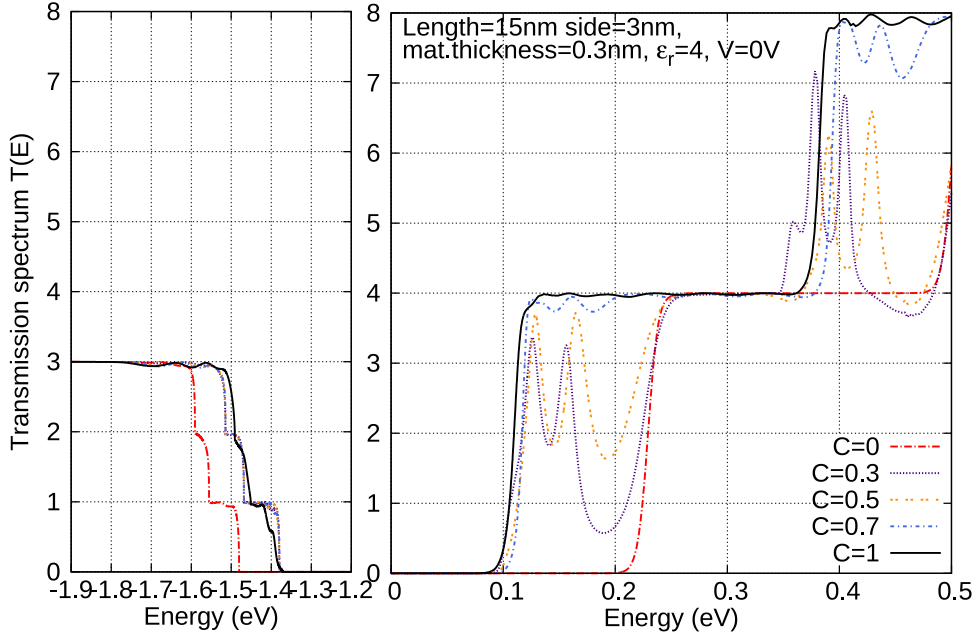


Figure 12.10. Transmission spectrum of a silicon nanowire varying the surface coverage (density). Surface material permittivity $\epsilon_r = 4$.

Percentage of channel covering

The envisioned employment of silicon nanowires in gas sensing applications is based on the already mentioned modifications in the conduction transport properties induced by the interaction of the silicon channel atoms with molecules which chemically attach to the surface of the wire. The amount of molecules interacting with silicon atoms should naturally depend on their abundance in the surrounding space, consequently altering the nanowire transport in a larger or smaller extent. It is worthwhile, then, studying the effects of surface interaction when the wire is only partially covered with an external material.

In this section we report the results of the simulation of a silicon nanowire (side $3nm$, length $15nm$) for varying concentrations of material interacting on the surface. The device under consideration is schematically depicted in fig. 12.1-c, where the percentage of the surface layer is varied modifying the width of the surface coloured stripes.

The transmission spectrum at equilibrium (0V) of the nanowire is shown in fig.12.10 for different values of surface coverage. The extreme cases of completely covered channel ($C = 1$ in the figure) and channel with no surface material ($C = 0$) present a regular profile denoting the existence of conductive bands available. Their step-like behaviour is the fingerprint of transport conduction in a perfect wire with a

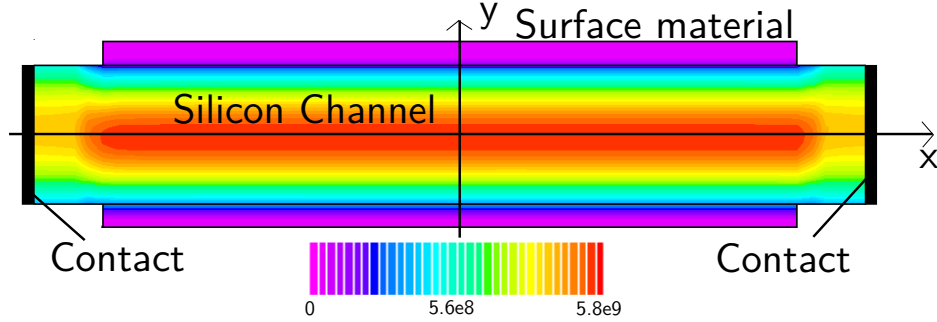


Figure 12.11. Squared modulus of the eigenfunction $|\Psi_E(x,y)|$ [cm^{-3}] corresponding to the new energy level $E = 0.12\text{eV}$ arisen in the transmission spectrum of a silicon nanowire interacting with a surface material (thickness 5\AA , $\epsilon_r = 4$, channel covering 30%); the function is shown on a section of the device (side 3nm , length 15nm).

translational invariance along the transport direction and strongly confining potential in the transverse section. The values of energy corresponding to jumps in the transmission are the eigenvalues of the hamiltonian in the transverse plane.

In both cases, the energy difference between the conduction and valence bands (the Fermi level corresponds to 0eV) is the energy-gap, which is higher for the covered channel, revealing a weakening of the confinement effect as consequence of the interface layer.

When increasing the surface density starting from the pristine wire, the transmission spectrum modifies with the formation of peaks corresponding to new energy levels below the minimum conduction-band energy. These new states are not related to existing 1D band states but derive from the channel interaction with the surface material. They effectively contribute to current in the wire as it can be inferred by looking at the spatial distribution of the energy eigenfunction corresponding to the newly arisen energy level (see fig.12.11). The wavefunction is spread in the channel signifying a not small probability of transmission from one contact to the other of the system.

The amplitude of the peaks in the spectrum changes with continuity in order to recover the extremal spectra of $C = 0$ and $C = 1$ surface coverages. Hence, the peak amplitude and width reveal a dependence on the percentage of surface covering. The position in the energy spectrum of the new levels, instead, is almost fixed by the extreme configurations of zero and maximum surface coverage.

The variations in the peak amplitude and width with respect to surface coverage, then, represent key factors in the use of silicon nanowire as gas sensors, since they largely determine the sensitivity of the sensor for varying concentration of the chemical species to be detected. More precisely, the larger the surface coverage, the higher

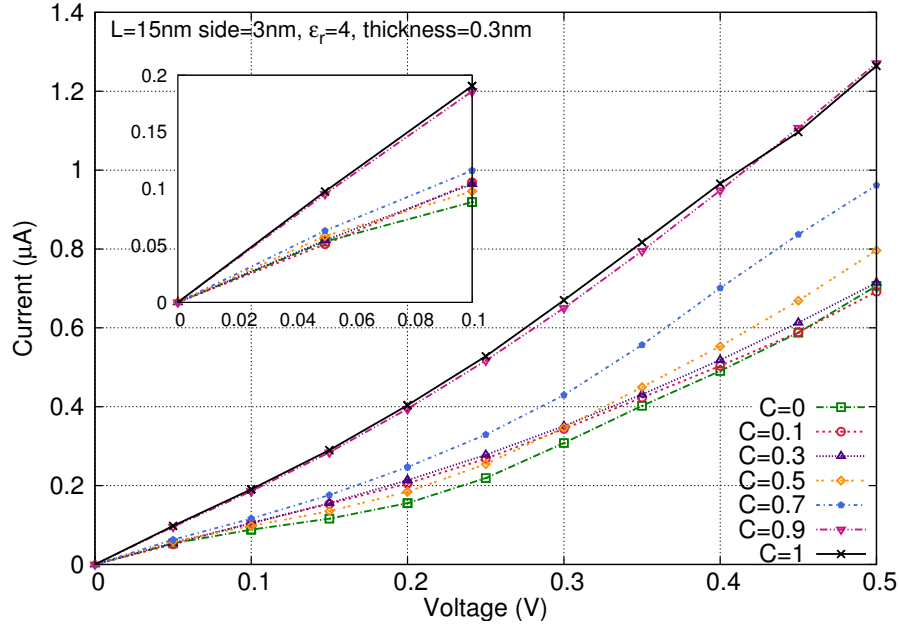


Figure 12.12. Current-Voltage characteristics for a Si-NW with side 3nm for different values of surface covering C .

and wider the peak. Current and, more frequently, differential conductance are consequently modified. Current-voltage characteristics of the device for different values of channel covering are shown in fig.12.12. A monotonic increase of current is detected with the percentage of channel covering due to the availability of wider and more conductive channels in the wire at lower values of energies.

Multiple Layer Interaction

This section is devoted to the discussion of simulation results obtained when simulating a silicon nanowire whose surface is partially covered by two different kinds of layer materials. This particular configuration reproduces the situation of silicon-based sensors whose surface chemically interacts with different chemical species which unavoidably attach the sensor surface [180, 181]. Silicon atoms are, indeed, prone to build bonds with several molecules which determine a modification of the transport properties of the sensor [182].

Hence, a problem of multiple interaction with different chemical species arises and a careful analysis is required on how transport in the silicon nanowire is affected. In this work we simulated the behaviour of a silicon nanowire (section side 3nm, length=15nm) whose surface is partially covered with two different layer materials.

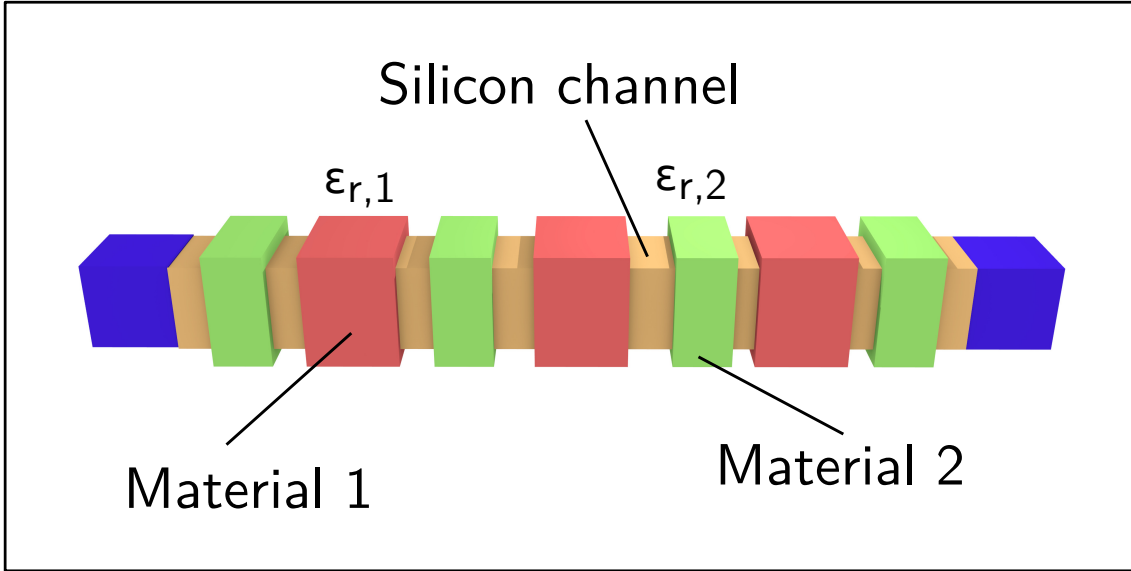


Figure 12.13. Structure of Si-NW whose surface is partially covered by two different material layers. In our analysis, they are 5\AA thick and differ only for their value of permittivity: $\epsilon_{r,1} \neq \epsilon_{r,2}$.

The structure is schematically depicted in fig.12.13. As in the previous section, surface coverages of the two materials is changed by varying the widths of the coloured stripes. The external materials adopted here only differ in their value of permittivity with thickness 5\AA . This choice is motivated by the preceding discussion from which it could be inferred that any modification of the surface layer properties (permittivity, charge density, thickness) could be reduced to an effective modification of the section dimensions of the wire. In particular, the surface materials have $\epsilon_{r,1} = 8$ and $\epsilon_{r,2} = 4$ respectively. The choice $\epsilon_{r,1} > \epsilon_{r,2}$ is by no means a loss of generality and still allows to uncover the effects that the disparity between the layers could engender. In accordance with the previous analysis, this inequality determines a modification of the effective side of the nanowire such that $W_{eff,1} > W_{eff,2}$, where $W_{eff,i}, i = 1,2$ are the effective sides.

Fig. 12.14 and 12.15 show the resulting transmission spectra for two different cases, respectively: a) the surface coverage of material 1 (C_1) is kept fixed while the coverage of material 2 (C_2) is varied; and b) C_2 is fixed while C_1 is varied. We will analyse them separately.

C_1 fixed, C_2 variable Fig. 12.14 shows the transmission spectrum for $C_1 = 0.3$ (percentage of surface covering 30%). In analogy with the preceding section, the interaction with surface materials determines the formation of spurious energy levels

in addition to the perfect-wire step-like transmission. In particular, for low values of C_2 two independent peaks are evident whose mean energy value is highlighted by the red vertical lines. The lowest peak is generated by the wire interaction with material 1 whose larger $W_{eff,2}$ tends to lower the conduction energy levels. A confirmation of this comes from the relatively small variation of the peak amplitude with increasing C_2 .

On the contrary, Material 2 (with smaller $W_{eff,2}$) is mainly responsible for the second peak, whose amplitude reveals a stronger dependence with the value of C_2 . Increasing C_2 , the amplitude grows consequently. In the limit case $C_2 = 0.6$, this second peak has eventually widened resulting in a step-like transmission spectrum with lower bottom energy.

C_1 variable, C_2 fixed When C_1 is changed ($C_2 = 0.3$), it is still possible to identify the presence of two peaks in the transmission spectrum (vertical lines in fig.12.15). In particular, the lower energy peak is now growing in amplitude after an increase of C_1 , which is the consequence of a widening portion of the silicon wire characterised by a non negligible low-energy density of states. Nevertheless, the amplitude of the second peak increases in amplitude with C_1 as well: this reveals the greater sensitivity of the interaction SiNW-Material2 with respect to the concentration of Material 1 when compared to the previous case. The increase of C_1 , indeed, opens conductive channels in the silicon wire favouring electron transport at lower energies. The second peak in the transmission spectrum is consequently strengthened by this effect and contributes more effectively to conduction. The limiting case with $C_1 = 0.6$ is, once again, characterized by a step-like transmission spectrum where the second peak, and thus the influence of the presence of Material 2, has been overtaken by the effects of Material 1, with larger effective side and higher coverage percentage.

The effects of multiple layer interaction in the transmission spectrum of SiNWs have naturally an impact on the current-voltage characteristics of the devices. Fig.12.16 shows the I-V curves of a silicon nanowire (side $3nm$, length $15nm$) when C_2 is fixed and equal to 0.6 while C_1 is varied from $C = 0$ (only Material 2 is deposited on the wire surface) and $C = 0.4$. The amount of surface covered by Material 2 ($\epsilon_{r,2} = 4$) determines a relevant variation of the conductivity of the wire, which increases proportionally with the fraction of surface covered by Material 1 ($\epsilon_{r,1} = 8$). This effect stems from the discussed formation of peaks in the transmission spectrum and their gradual amplitude enhancement. The causes of the latter reside in 1) the increase of C_1 and 2) the accentuated effect of one peak on the other with a consequently greater sensitivity of the nanowire to surface interaction with Material 1.

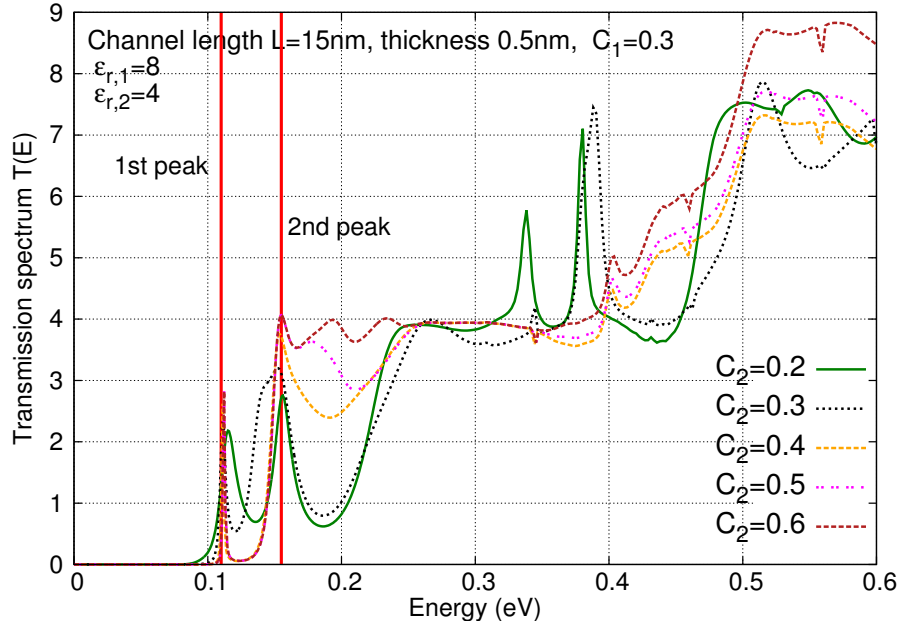


Figure 12.14. Transmission spectrum of a SiNW (length $15nm$, side $3nm$) interacting with two surface material layers (thickness 5\AA) with permittivity $\epsilon_{r,1} = 8$ and $\epsilon_{r,2} = 4$ respectively. In the figure, the percentage of channel covered by Material 1 is fixed, $C_1 = 0.3$, C_2 is variable.

12.3 Conclusions

In this chapter, we analysed the effects of a surface material layer on the transport properties of a silicon nanowire. Through a systematic simulative study the impact of the external layer properties (thickness, permittivity and the presence of a charge density at the interface) has been discussed in terms of confining potential inside the channel and current. A thicker surface layer affects the conduction increasing the current; the reasons have been found in a widening of the quantum confining potential and the corresponding lowering of conduction bands energies. A similar widening of the potential confining profile origins when increasing the layer permittivity. Hence, a higher current is obtained. Also the effects of a surface charge density have been found to stem from a modification of the transverse confinement strength in the channel. In particular, a charge density weakens the electron confinement if positive, it reinforces it if negative. Higher and lower currents are consequently found in the two cases, respectively.

In the second part of the chapter we presented the analysis of the impact of the amount of surface coverage on nanowires conduction as well as a discussion on how the interaction with two external materials modifies electron transport in these devices. In particular, a variation in the surface coverage has been found to determine

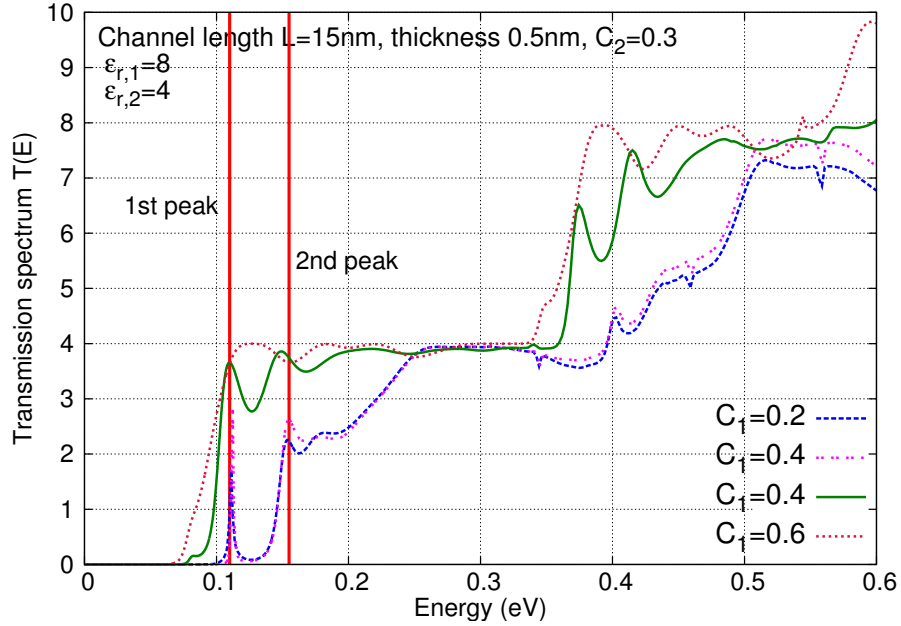


Figure 12.15. Transmission spectrum of a SiNW (length $15nm$, side $3nm$) interacting with two surface material layers (thickness 5\AA) with permittivity $\epsilon_{r,1} = 8$ and $\epsilon_{r,2} = 4$ respectively. The percentage of channel covered by Material 1 is a parameter while $C_2 = 0.3$ is kept fixed.

the formation of new energy conduction channels in the transmission spectrum, whose amplitude and width increase proportionally with the surface covering. Laying below the conduction bands, they are consequently responsible for a higher current with respect to the pristine wire.

In the case of multiple interaction layers, spurious low-energy peaks can be still devised which generally determine an increase of conductivity. Their energy and amplitude have been found to depend strongly on the properties of the materials. Interestingly, particular surface material properties have been shown to engender an interdependence relationship among the peaks, and consequently in the current.

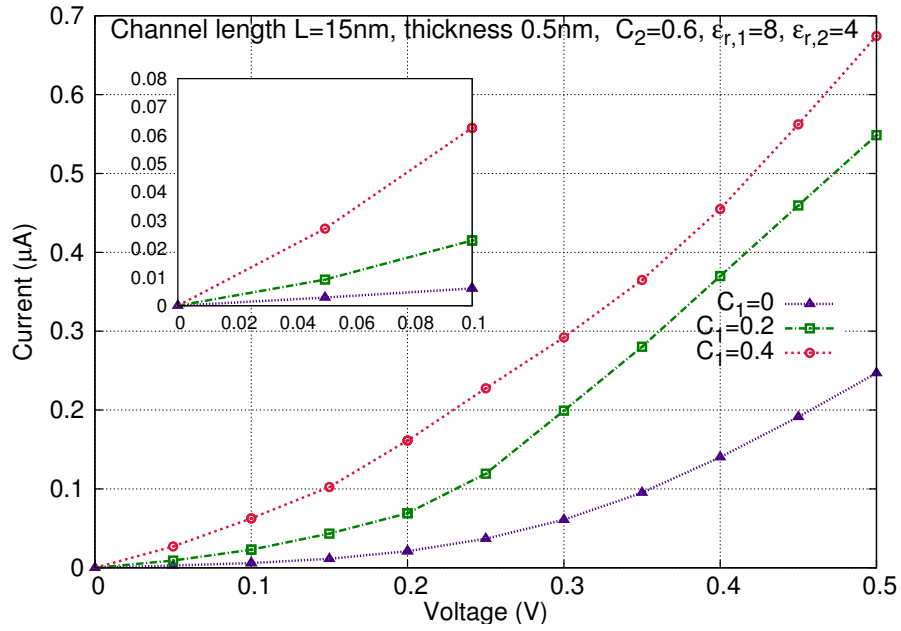


Figure 12.16. Current-Voltage characteristics of a SiNW (length 15nm , side 3nm) interacting with two surface material layers (thickness 5\AA) with permittivity $\epsilon_{r,1} = 8$ and $\epsilon_{r,2} = 4$ respectively. The percentage of channel covered by Material 1 is a parameter while $C_2 = 0.6$ is kept fixed.

Chapter 13

Conclusions

In this thesis work we presented the main results of our research activity on modelling and simulation of Silicon-Based devices. Two main topics were covered in major details: silicon nanowires used for computational logic and for bio-chemical sensing.

In particular, we devised a compact numerical model for Multiple-Independent Gate Transistors which has been proved to be computationally efficient and accurate. Numerical validation with physics-based software was performed.

In the field of bio-chemical sensing, our research activity has been focused on Porous Silicon, a very particular material characterised by a complex microscopic morphology made of crystalline regions immersed in a amorphous network. Thanks to its large surface-to-volume ratio and chemical reactivity at room temperature it is suitable for sensing. In the last three years we developed two numerical models for PS nanowires with different validity regimes both including a careful description of quantum effects (quantum potential confinement and coherent transport).

The last part of the work was devoted to the study of the effects of surface interaction on the conduction properties of silicon nanowires. Starting from an atomistic approach based on Density Functional Theory, we analysed systems of nanowires with diameters larger than 2 nm when molecules and dielectric materials are deposited on the surface. Interesting phenomena have been found which shed new light on silicon nanowires for bio-chemical sensing.

Appendix A

Density Functional Theory

A.1 A brief DFT survey

The first theoretical foundation of *Density Functional Theory (DFT)* was introduced in 1964 by Hohenberg and Kohn in a famous paper [65] that was worth the Nobel Prize for Chemistry to Kohn in 1998. They demonstrated that all the electronic properties of the system in its non-degenerate ground-state (GS) configuration can be completely described by its electron density $n(r)$; moreover, the total energy and the potentials can be described as functionals of $n(r)$ only.

One year later, in 1965, moving from the HK theorem, Kohn and Sham provided a *self-consistent* scheme in order to map the interacting many-body problem into a set of non-interacting single particle equation reformulating the mean-field method into a variational principle. The milestones of DFT can therefore be considered the Hohenberg-Kohn theorem and the Kohn-Sham equations.

A.1.1 The Hohenberg-Kohn theorem

The Hohenberg-Kohn (HK) theorem succeeded to demonstrate that the properties linked to the electronic structure of a system in its fundamental non-degenerate ground-state are completely and univocally described by its electronic ground-state. The theorem asserts that:

"The ground-state density $n(r)$ of a bound system of interacting electrons in some external potential $v(r)$ determines this potential uniquely" where "uniquely" means "up to an additive constant" (defined in the Hohenberg-Kohn paper) and in the case of degenerate ground-state, the lemma refers to any ground-state density $n(r)$. Taking into account a N-electron system interacting in presence of an external potential V_{ext} , the Hamiltonian results

$$\hat{H} = \hat{T} + \hat{V}_{ext} + \hat{W} \quad (\text{A.1})$$

a sum of kinetic term

$$\hat{T} = -\frac{1}{2} \sum_i^N \nabla_i^2 \quad (\text{A.2})$$

an electron-electron interaction Coulomb potential term

$$\hat{W} = \frac{1}{2} \sum_{i \neq j} v_{ij}(|\mathbf{r}_i - \mathbf{r}_j|) \quad (\text{A.3})$$

and a term representing the interaction with the external potential $V_{ext}(\mathbf{r})$

$$\hat{V}_{ext} = \sum_i^N v_{ext}(\mathbf{r}_i) \quad (\text{A.4})$$

the ground-state many-body wavefunction can be defined as $\varphi(\mathbf{r}_1 \cdots \mathbf{r}_N)$ and the ground-state electronic density is

$$n(\mathbf{r}_1) = N \int \varphi^*(\mathbf{r}_1 \cdots \mathbf{r}_N) \varphi(\mathbf{r}_1 \cdots \mathbf{r}_N) d\mathbf{r}_2 \cdots d\mathbf{r}_N \quad (\text{A.5})$$

The HK theorem asserts that φ and V_{ext} are univocally determined by the electronic density $n(\mathbf{r})$ only and they are called unique functional of the electronic charge density. From the eigenvalues equation

$$\hat{H} |\varphi(r)\rangle = E_{GS} |\varphi(r)\rangle \quad (\text{A.6})$$

$$(\hat{T} + \hat{V} + \hat{W}) |\varphi(\mathbf{r})\rangle = E_{GS} |\varphi(\mathbf{r})\rangle \quad (\text{A.7})$$

although T and W are univocally specified through the HK theorem, on the other hand, the potential v , supposed in the original paper [65] to be local, bounded and spin-independent, can be considered to be an element of the \mathbf{V} ensemble containing all the external potentials generating a ground-state for the system. Each v can be related to a ground-state wavefunction φ_{GS} to which a unique electronic charge density $n_{GS}(\mathbf{r})$ corresponds:

$$n_{GS}(\mathbf{r}) = \langle \varphi_{GS} | \hat{n}(\mathbf{r}) | \varphi_{GS} \rangle \quad (\text{A.8})$$

All the densities that satisfy this relation belong to the ensemble \mathbf{N} and are called v -representable because they are ground-state electronic densities of the hamiltonian \hat{H} obtained from different $v_{ext} = \int v(\mathbf{r}) n(\mathbf{r}) d\mathbf{r} \in \mathbf{V}$. It is possible to construct a map between a set of external potential $v(\mathbf{r})$ and the corresponding ground-state densities $n(\mathbf{r})$

$$\mathcal{G} : v(\mathbf{r}) \rightarrow |\varphi(\mathbf{r})\rangle \quad (\text{A.9})$$

and since the HK theorem shows that \mathcal{G} is surjective and injective, thus biunivocal and invertible:

$$\mathcal{G}^{-1} : n(\mathbf{r}) \rightarrow v(\mathbf{r}) + c \quad (\text{A.10})$$

the ground-state density could be considered the basic variable in the electronic problem. The application \mathcal{G} is surjective for construction but to prove that it is also injective one can show that two different systems subjected to two external potentials differing only for a constant, $v(\mathbf{r}) \neq v'(\mathbf{r}) + c$, they cannot have the same electronic density for the ground-state, $n(\mathbf{r}) = n'(\mathbf{r})$ leads to an absurdum. This implies that the ground-state expectation value for any physical observable is a unique functional of the ground-state electron density $n(\mathbf{r})$:

$$\langle \varphi[n] | \hat{O} | \varphi[n] \rangle = O[n] \quad (\text{A.11})$$

In particular, according to these findings, we can define the total energy of the N-electron system as the expectation value calculated on the ground state wavefunction $|\varphi\rangle$:

$$E[n(\mathbf{r})] = \langle \varphi[n] | \hat{H} | \varphi[n] \rangle \quad (\text{A.12})$$

and defining the universal functional $F_{HK}[n]$:

$$F_{HK}[n] = \langle \varphi[n] | (\hat{T} + \hat{W}) | \varphi[n] \rangle \quad (\text{A.13})$$

the total energy becomes

$$E_v[n(\mathbf{r})] = \int v(\mathbf{r})n(\mathbf{r})d\mathbf{r} + F_{HK}[n] \quad (\text{A.14})$$

It is worth pointing out that $F_{HK}[n]$ is a universal functional because it does not depend on the external potential and it is the same density functional for atoms, molecules and solids since in all cases \hat{W} is the Coulomb repulsion between the electrons and \hat{T} , the kinetic energy.

The second part of the HK theorem establishes that through a reformulation of the *Rayleigh-Ritz variational principle* in terms of the electron density $n(\mathbf{r})$ it is possible to minimize the $E_v[n]$ functional in the class of regular functions $n(\mathbf{r})$ satisfying the condition $\int n(\mathbf{r})d\mathbf{r} = N$ for the exact ground-state density. The minimization process leads to

$$E = \min_{\tilde{n}(\mathbf{r})} E_v[\tilde{n}] = \min_{\tilde{n}(\mathbf{r})} \left\{ \int v(\mathbf{r})\tilde{n}(\mathbf{r})d\mathbf{r} + F[\tilde{n}] \right\} \quad (\text{A.15})$$

where $\tilde{n}\mathbf{r}$ refers to all functions of the v -representable class mentioned before. The minimum is attained when $\tilde{n}\mathbf{r}$ coincides with the $n(\mathbf{r})$ ground-state density for a non-degenerate case; for a degenerate case, instead, $\tilde{n}(\mathbf{r})$ is only one of the ground-state

densities. the constraint on the number of particles (that ensures the conservation) is resumed with

$$\frac{\delta E[n(\mathbf{r})]}{\delta n(\mathbf{r})} = \mu \quad (\text{A.16})$$

where μ represents the chemical potential of the system.

The formidable problem of finding the minimum of $\langle \tilde{\Psi} | H | \tilde{\Psi} \rangle$ with respect to the 3N-dimensional trial function $\tilde{\Psi}$ has been transformed into the seemingly trivial problem of finding the minimum of $E_v[\tilde{n}]$ with respect to the 3-dimensional trial function $\tilde{n}(\mathbf{r})$. However the main difficulty in the determination of the ground-state density is the form of the functional eq. A.13 fixed the external potential $v_{ext}(\mathbf{r})$ the lack of a proper analytical definition of the $F_{HK}[n]$ functional leads straight to the use of approximations of $e_v[\tilde{n}(\mathbf{r})]$ for the calculation of E_{tot} and $n(\mathbf{r})$.

A.1.2 The Kohn-Sham equations

A particularly important strategy to solve the problem of the practical DFT implementations was introduced by Kohn and Sham [66]. They considered an auxiliary system of N non-interacting electrons subjected to an effective potential $v_{eff}^{KS}(\mathbf{r})$ and described by the Hamiltonian

$$\hat{H}^{KS} = \hat{T}^{KS} + \hat{v}_{eff}^{KS} \quad (\text{A.17})$$

by moving from the initial Hartree formulation of the Schrodinger equation for non-interacting electrons in the external potential v_{eff} and from the HK minimal principle. According to the theorem of Hohenberg and Kohn, for a non-interacting N-particle system, the energy is a functional of the density:

$$E_s[n] = T_s[n] + \int v_s(\mathbf{r})n(\mathbf{r})d\mathbf{r} \quad (\text{A.18})$$

The central assertion used in establishing the Kohn-Sham scheme is the following: "for any interacting system, there exists a local single particle potential $v_{ks}(\mathbf{r})$ such that the exact ground-state density $n(\mathbf{r})$ of the interacting systems is equal to the ground-state density of the auxiliary system $\tilde{n}(\mathbf{r})$, i.e. $n(\mathbf{r}) = \tilde{n}(\mathbf{r})$ ".

Minimizing the energy functional for the Kohn-Sham system of N-independent particles, with the constraint on the number of electrons and considering that the density $\tilde{n}(\mathbf{r})$ must be constructed for an independent-particle system (one-single Slater determinant), we obtain a set of equations:

$$\left[-\frac{\hbar^2}{2m} \nabla^2 + v_s(\mathbf{r}) \right] \varphi_i(\mathbf{r}) = \epsilon_i \varphi_i(\mathbf{r}) \quad (\text{A.19})$$

The density has a unique representation in terms of the lowest N single-particle orbitals

$$n(\mathbf{r}) = \tilde{n}(\mathbf{r}) = \sum_{i=1}^N |\varphi_i(\mathbf{r})|^2 \quad (\text{A.20})$$

where the constraint on the density becomes equivalent to the orthonormality of the wavefunctions:

$$\int d\mathbf{r} \varphi_j^*(\mathbf{r}) \varphi_i(\mathbf{r}) = \delta_{ij} \quad (\text{A.21})$$

Once the existence of a potential $v_s(\mathbf{r})$ generating a given interacting density $n(\mathbf{r})$ is assumed, the uniqueness of $v_s(\mathbf{r})$ follows from the Hohenberg-Kohn theorem. Thus the single-particle orbitals are unique functionals of the density: $n(\mathbf{r})$, $\phi_i(\mathbf{r}) = \phi_i([n(\mathbf{r})])$ and the non interacting kinetic energy $T_s[n(\mathbf{r})]$ is a unique functional of $n(\mathbf{r})$ as well.

Starting from the interacting system subject to an external potential $v(\mathbf{r})$ we can rewrite the total energy functional of eq. A.14 splitting $F_{HK}[n]$ as

$$F_{HK}[n] = \frac{1}{2} \int \int d\mathbf{r} d\mathbf{r}' \frac{n(\mathbf{r})n(\mathbf{r}')}{|\mathbf{r} - \mathbf{r}'|} + T_s[n] + E_{xc}[n] \quad (\text{A.22})$$

and obtaining in this way

$$E_v[n] = T_s[n] + \int d\mathbf{r} v(\mathbf{r}) n(\mathbf{r}) + \frac{1}{2} \int \int d\mathbf{r} d\mathbf{r}' \frac{n(\mathbf{r})n(\mathbf{r}')}{|\mathbf{r} - \mathbf{r}'|} + E_{xc}[n] \quad (\text{A.23})$$

where we have inserted three terms in $F_{HK}[n]$ such as:

- the Hartree energy term $\frac{1}{2} \int \int d\mathbf{r} d\mathbf{r}' \frac{n(\mathbf{r})n(\mathbf{r}')}{|\mathbf{r} - \mathbf{r}'|}$ describing interaction among electrons
- the kinetic energy T_s of the non-interacting system
- the term $E_{xc}[n]$ called exchange-correlation energy and unfortunately still unknown, defined as

$$E_{xc}[n] = F_{HK}[n] - \frac{1}{2} \int \int d\mathbf{r} d\mathbf{r}' \frac{n(\mathbf{r})n(\mathbf{r}')}{|\mathbf{r} - \mathbf{r}'|} - T_s[n] \quad (\text{A.24})$$

but from eq. A.13 we can see that E_{xc} consists of a potential and a kinetic part

$$E_{xc}[n] = \left(W[n] - \frac{1}{2} \int \int d\mathbf{r} d\mathbf{r}' \frac{n(\mathbf{r})n(\mathbf{r}')}{|\mathbf{r} - \mathbf{r}'|} \right) + (T[n] - T_s[n]) \quad (\text{A.25})$$

The Hohenberg and Kohn variational principle ensures that $E_v[n]$ is stationary for small variations of $\delta n(\mathbf{r})$ around the minimum density $n(\mathbf{r})$:

$$\delta E_v[n] = E[n + \delta n] - E[n] = 0 \quad (\text{A.26})$$

$$\int \delta \tilde{n}(\mathbf{r}) \left\{ v(\mathbf{r}) + \frac{\delta T_s[\tilde{n}]}{\delta \tilde{n}(\mathbf{r})} + \frac{1}{2} \int d\mathbf{r}' \frac{\tilde{n}(\mathbf{r})}{|\mathbf{r} - \mathbf{r}'|} + \frac{\delta E_{xc}[\tilde{n}]}{\delta \tilde{n}(\mathbf{r})} - \mu \right\}_{\tilde{n}=n} d\mathbf{r} = 0 \quad (\text{A.27})$$

After applying the Euler-Lagrange equations and introducing an exchange-correlation potential v_{xc} defined as

$$v_{xc}(\mathbf{r}) = \frac{\delta E_{xc}[n]}{\delta n(\mathbf{r})} \quad (\text{A.28})$$

and an effective potential

$$v_{eff}^{KS}(\mathbf{r}) = v(\mathbf{r}) + \frac{1}{2} \int \frac{n(\mathbf{r})}{|\mathbf{r} - \mathbf{r}'|} d\mathbf{r}' + v_{xc}(\mathbf{r}) \quad (\text{A.29})$$

one finally gets the so-called *self-consistent Kohn-Sham (KS) equations*:

$$\left\{ -\frac{1}{2} \nabla^2 + v_{eff}^{KS}(\mathbf{r}) - \epsilon_i^{KS} \right\} \varphi_i^{KS} = 0 \quad (\text{A.30})$$

where the ϵ_i^{KS} and φ_i^{KS} are the Kohn-Sham eigenvalues and eigenvectors respectively. It can be observed that since

$$\begin{aligned} \sum_i^N \epsilon_i &= \sum_i \langle \varphi_i | -\frac{1}{2} \nabla^2 + v_{eff}(\mathbf{r}) | \varphi_i \rangle = T_s[n(\mathbf{r})] + \int v_{eff} n(\mathbf{r}) d\mathbf{r} = \\ &= T_s + \int v(\mathbf{r}) n(\mathbf{r}) d\mathbf{r} + \frac{1}{2} \int \int \frac{n(\mathbf{r}) n(\mathbf{r}')}{|\mathbf{r} - \mathbf{r}'|} d\mathbf{r} d\mathbf{r}' + \int v_{xc} n(\mathbf{r}) d\mathbf{r} \end{aligned}$$

and

$$E_v[n] = T_s + \int v(\mathbf{r}) n(\mathbf{r}) d\mathbf{r} + \frac{1}{2} \int \int \frac{n(\mathbf{r}) n(\mathbf{r}')}{|\mathbf{r} - \mathbf{r}'|} d\mathbf{r} d\mathbf{r}' + E_{xc}[n] \quad (\text{A.31})$$

then the *total energy* of the interacting system can be expressed as

$$\begin{aligned} E_{tot} &= T_s[n] + \int v_{ext}(\mathbf{r}) n(\mathbf{r}) d\mathbf{r} + \frac{1}{2} \int \int \frac{n(\mathbf{r}) n(\mathbf{r}')}{|\mathbf{r} - \mathbf{r}'|} d\mathbf{r} d\mathbf{r}' + E_{xc}[n] = \\ &= \sum_i^N \epsilon_i - \frac{1}{2} \int \int \frac{n(\mathbf{r}) n(\mathbf{r}')}{|\mathbf{r} - \mathbf{r}'|} d\mathbf{r} d\mathbf{r}' + E_{xc}[n] - \int v_{xc}(\mathbf{r}) n(\mathbf{r}) d\mathbf{r} \end{aligned}$$

If one neglects the E_{xc} and the v_{xc} terms altogether, the KS equations reduce to the self-consistent Hartree equations. The same must hold also for the non-interacting systems and we can write

$$0 = \delta E_s[n] = E_s[n + \delta n] - E_s[n] = \delta T_s + \int d\mathbf{r} \delta n(\mathbf{r}) v^{KS}(\mathbf{r}) \quad (\text{A.32})$$

This leads to the final expression as seen above

$$v_{eff}^{KS} = v_{ext}(\mathbf{r}) + \int d\mathbf{r}' \frac{n(\mathbf{r}')}{|\mathbf{r} - \mathbf{r}'|} + v_{xc}(\mathbf{r}) \quad (\text{A.33})$$

The Kohn-Sham formalism relies on the link between an actual N electrons system and a fictitious non-interacting counterpart through the potential $v_{xc}(\mathbf{r})$. Hence, $v_{xc}(\mathbf{r})$ contains essential information about many-body correlations which Many-Body Perturbation Theory describes [68,69] in terms on non local dynamical terms. It may be realized that the mapping between ground-state densities and Kohn-Sham potentials $v^{KS}[n](\mathbf{r})$ depends on $n(\mathbf{r})$ in a very peculiar and sensitive way. In fact the actual functional relation between $n(\mathbf{r})$ and $v_{xc}(\mathbf{r})$ is highly non-analytical: small or even infinitesimal changes in the density may induce substantial variations in the xc potential. It is highly non local, i.e. changes in the density at a given point \mathbf{r} may induce substantial variations of the xc potential at a point \mathbf{r}' .

The KS equation can be regarded as the exact formalization of the Hartree scheme: with the exact E_{xc} and v_{xc} all the many-body effects are completely taken into account by principle, and the main effort of DFT lies in the practical usefulness of ground-state when the good approximation for the xc functional is found. Hence it is necessary to find a good approximation for the exchange-correlation energy E_{xc} . Once a good approximation for E_{xc} is obtained, the Kohn-Sham equations must be solved self-consistently and then it is possible to get the ground-state density of the interacting system and its total energy.

A.1.3 The Form of E_{xc}

Since there is no exact analytical expression for the E_{xc} functional, the total energy calculation require some approximations for it. In the next section we will focus the attention on three of these approximations: the Local Density Approximation (LDA), the Local Spin Density Approximation and the Generalized Gradient Approximation.

The Local Density Approximation According to this approximation, the xc functional is defined as a *local function* of the density of a homogeneous electron gas:

$$E_{xc} = \int d\mathbf{r} \epsilon_{xc}^{hom}(n(\mathbf{r})) \quad (\text{A.34})$$

where ϵ_{xc} is the *exchange-correlation energy per electron* of the homogeneous and uniform electron gas. Taking into account an interacting *homogeneous* electron gas, we can say that the exchange-correlation energy per electron is in this case a

function of the density and not a functional since the density is constant for this kind of system: thus $\epsilon_{xc}[n(\mathbf{r})] \leftarrow \epsilon_{xc}(n(\mathbf{r}))$ and multiplying for the number of electrons we get $E_{xc}[n] = N\epsilon(n(\mathbf{r}))$. In the local Density Approximation, the *inhomogeneous* electron gas is handled in the same way: the exchange-correlation energy is the sum of the contribution of each portion of the *non-uniform* gas as it was local uniform. Thus the exchange-correlation potential becomes

$$v_{xc}^{LDA}(\mathbf{r}) = \frac{\partial E_{xc}[n]}{\partial n(\mathbf{r})} = \frac{\partial \int \epsilon_{xc}(n(\mathbf{r})) d\mathbf{r}}{\partial n(\mathbf{r})} = \epsilon_{xc}(n(\mathbf{r})) + n(\mathbf{r}) \left(\frac{\partial \epsilon_{xc}}{\partial n} \right)_{n(\mathbf{r})} = \mu_{xc}(n(\mathbf{r})) \quad (\text{A.35})$$

where $\mu_{xc}(n(\mathbf{r}))$ is the exchange-correlation contribution to the chemical potential for a uniform system. The approximation is said to be *local* because $\epsilon_{xc}(\mathbf{r})$ depends from the local value of the density $n(\mathbf{r})$ in the \mathbf{r} position only. The LDA works well for systems with a *slowly varying density* and has proven very successful for calculation of ground-state properties. The lattice constants are predicted within $\approx 1\%$, while the cohesive energy is quite generally overestimated, as a result usually attributed to the predicted under bindings atoms within LDA. On the other hand the LDA fails in the estimation of the fundamental energy gap of semiconductors and insulators.

Spin Density Approximation One improvement with respect to the LDA can be achieved with the implementation of polarization in spin, in the so-called *Local Spin Density Approximation (LSDA)*, in particular for systems that are subjected to an external magnetic field or are polarized or where the relativistic effects are important. The main motivation is due to the fact that the exchange-correlation hole is very different for the electrons with parallel and anti-parallel spins, and that LSD probably gives a better and correct description of the spherically averaged exchange-correlation hole. In this approximation, the density is now *spin-polarized* with two contributions: $n^\uparrow(\mathbf{r})$ and $n^\downarrow(\mathbf{r})$. Considering an N -electrons Hamiltonian coupled with the magnetic field $\vec{B}(\mathbf{r})$ and the spin $\hat{\mathbf{s}}$

$$\hat{H} = \hat{T} + \hat{V}_{ee} + \sum_i v(\mathbf{r}_i) - 2\mu \sum_i \vec{B}(\mathbf{r}_i) \hat{\mathbf{s}} \quad (\text{A.36})$$

the density can be defined now as

$$n_\sigma(\mathbf{r}) = \sum_\alpha f_{\alpha\sigma} |\phi_{\alpha\sigma}(\mathbf{r})|^2 \quad (\text{A.37})$$

with $f_{\alpha\sigma}$ occupation number between 0 and 1 and the energy like functionals of the spin polarized densities $n^\uparrow(\mathbf{r})$ and $n^\downarrow(\mathbf{r})$ as:

$$\tilde{E} = T[n^\uparrow, n^\downarrow] + U[n] + E_{xc}[n^\uparrow, n^\downarrow] + \int d\mathbf{r} v(\mathbf{r}) n(\mathbf{r}) - 2\mu \int d\mathbf{r} \vec{B}(\mathbf{r}) \sum_\sigma \sigma n_\sigma(\mathbf{r}) \quad (\text{A.38})$$

and minimizing the above functional with respect to the density $n_\sigma(\mathbf{r})$ through the application of a generalized Hohenberg-Kohn variational principle it is possible to obtain a set of Kohn-Sham like equations for the spin polarization

$$\left\{ -\frac{1}{2}\nabla^2 + v_{eff}^\sigma(\mathbf{r}) \right\} \phi_{\alpha\sigma} = \epsilon_i^\sigma \phi_{\alpha\sigma} \quad (\text{A.39})$$

with an effective potential

$$V_{eff}^\sigma(\mathbf{r}) = v_{ext}(\mathbf{r}) + \frac{1}{2} \int \frac{n(\mathbf{r}')}{|\mathbf{r} - \mathbf{r}'|} d\mathbf{r}' + V_{xc}^\sigma(\mathbf{r}) \quad (\text{A.40})$$

where the exchange-correlation potential is

$$V_{xc}^\sigma([n^\uparrow, n^\downarrow]; \mathbf{r}) = \frac{\delta}{\delta n_\sigma(\mathbf{r})} E_{xc}[n^\uparrow, n^\downarrow] \quad (\text{A.41})$$

and the direct Coulomb potential is

$$u([n]; \mathbf{r}) = \frac{\delta}{\delta n(\mathbf{r})} U[n] = \int d\mathbf{r}' \frac{n(\mathbf{r}')}{|\mathbf{r} - \mathbf{r}'|} \quad (\text{A.42})$$

Spin density functional calculation would yield exact results if the exact E_{xc} were known and used; in the local spin density approximation one recovers

$$E_{xc}^{LSD}[n^\uparrow, n^\downarrow] = \int d\mathbf{r} n(\mathbf{r}) \epsilon_{xc}(n^\uparrow(\mathbf{r}), n^\downarrow(\mathbf{r})) \quad (\text{A.43})$$

Gradient Expansion and GGA A natural way to go beyond the LDA is to extend the exchange-correlation functional with terms containing the gradient of the density. Through the inclusions of these gradients, variations and changes in the density can be estimated and measured leading to a possible improvement of the results. *The Gradient Expansion* offers systematic corrections to LSD electron densities that vary slowly over space and might appear to be a natural step beyond LSD. In the original papers of Hohenberg-Kohn and Kohn-Sham [65,66] is already presented a gradient expansion based on the polarizability of the homogeneous electron gas. For densities $n(\mathbf{r})$ varying slowly over space and having weak variations so that $n(\mathbf{r}) = n_0 + \Delta n(\mathbf{r})$, it is possible to expand the density around the point \mathbf{r} taken to be the origin:

$$n(\mathbf{r}) = n + \nabla_i n(\mathbf{r}) \mathbf{r}_i + \frac{1}{2} \sum \nabla_{ij} n(\mathbf{r}) \mathbf{r}_i \mathbf{r}_j + \dots \quad (\text{A.44})$$

substituting this expansion in the expression of E_{xc} it leads after some mathematical manipulation to the *gradient expansion*

$$E_{xc} = E_{xc}^{LDA} + \int G_2(n)(\nabla n)^2 d\mathbf{r} + \int [G_4(n)(\nabla^2 n)^2 + \dots] d\mathbf{r} + \dots \quad (\text{A.45})$$

where $G_2(n)$ is the universal functional appearing in the Kohn-Sham equations defined as $G[n] = E_{xc}[n] + T_s[n]$. The terms of the series above can be resumed as

$$E_{xc}^{(0)} = \int \epsilon(n(\mathbf{r})) n(\mathbf{r}) d\mathbf{r} \quad (LDA) \quad (A.46)$$

$$E_{xc}^{(1)} = \int f^1(n(\mathbf{r}), |\nabla n(\mathbf{r})|) n(\mathbf{r}) d\mathbf{r} \quad (GGA) \quad (A.47)$$

$$E_{xc}^{(2)} = \int f^2(n(\mathbf{r}), |\nabla n(\mathbf{r})|) \nabla^2 n(\mathbf{r}) d\mathbf{r} \quad (A.48)$$

Here the $E_{xc}^{(0)}$ corresponds to the LDA level and requires the independently single-variable calculated function $n(\mathbf{r})$, while $E_{xc}^{(1)}$ is the so-called *Generalized Gradient Approximation* (GGA which requires the independently calculated *function of two variables*, $n(\mathbf{r})$ and $|\nabla n(\mathbf{r})|$).

Appendix B

List of Publications

- A. Antidormi, S. Frache, M. Graziano, P.E. Gaillardon, G. Piccinini, G. De Micheli, "Computationally Efficient Multiple-Independent-Gate Device Model," in *Nanotechnology, IEEE Transactions on*, vol.15, no.1, pp.2-14, Jan. 2016
doi: 10.1109/TNANO.2015.2493543
- A. Pulimeno, M. Graziano, A. Antidormi, R. Wang, A. Zahir and G. Piccinini, Field-coupled nanocomputing, Chapter: "Understanding a Bisferrocene Molecular QCA wire", Lectures Notes in Computer Science, Springer Berlin, 2013
- A. Antidormi, D. Chiabrando, M.G. Graziano, L. Boarino, G. Piccinini, "Methodology Modeling of Ma-E fabricated Porous Silicon Nanowires", *IEEE Prime Conference 2014* (AWARDED with the Silver Leaf)
- A. Antidormi, M.G. Graziano, L. Boarino, G. Piccinini, "Analysis of the Effects of surface interaction on Silicon Nanowires conduction", *IEEE NANO 2015, 15th Conference on Nanotechnology*, Rome, July 27-30 2015, pp. 1-3
- A. Antidormi, G. Turvani, M.G. Graziano, L. Boarino, G. Piccinini, "Impact of Surface Materials on Silicon Nanowires conduction", in *IEEE Transactions of Nanotechnology* (submitted)
- A. Antidormi, M.G. Graziano, L. Boarino, G. Piccinini, "Computational Model for Silicon Nanowires and Nanocrystals arrays", in *IEEE Transactions of Nanotechnology* (submitted)

Bibliography

- [1] T. Mikolajick, A. Heinzig, J. Trommer, S. Pregl, M. Grube, G. Cuniberti, W.M. Weber, Silicon nanowires - a versatile technology platform. *Phys. Status Solidi Rapid Res. Lett.* 7, 793-799 (2013)
- [2] J. Izuan, A. Rashid, J. Abdullah, N.A. Yusof, R. Hajia, The development of silicon nanowire as sensing material and its applications. *J. Nanomater.* 2013, 328093-32119 (2013)
- [3] F. Patolsky, C.M. Lieber, Nanowire nanosensors. *Mater. Today* 8, 20-28 (2005)
- [4] M.D. Kelzenberg, S.W. Boettcher, J.A. Petykiewicz, D.B. Turner-Evans, M.C. Putnam, E.L. Warren, J.M. Spurgeon, R.M. Briggs, N.S. Lewis, H.A. Atwater, Enhanced absorption and carrier collection in Si wire arrays for photovoltaic applications. *Nat. Mater.* 9, 239-244 (2010)
- [5] K.-Q. Peng, X. Wang, L. Li, Y. Hu, S.-T. Lee, Silicon nanowires for advanced energy conversion and storage. *Nano Today* 8, 75-97 (2013)
- [6] C. Mack, The future of semiconductor lithography? Look to flash. *J. Micro/-Nanolith. MEMS MOEMS* 12, 030101 (2013)
- [7] V. Schmidt, J.V. Wittemann, S. Senz, U. Goesele, Silicon nanowires: a review on aspects of their growth and their electrical properties. *Adv. Mater.* 21, 2681-2702 (2009)
- [8] F.-L. Yang, D.-H. Lee, H.-Y. Chen, C.-Y. Chang, S.-D Liu, C.-C. Huang, T.-X. Chung, H.- W. Chen, C.-C. Huang, Y.-H. Liu, C.-C. Wu, C.-C. Chen, S.-C. Chen, Y.-T. Chen, Y.-H. Chen, C.-J. Chen, B.-W. Chan, P.-F. Hsu, J.-H. Shieh, H.-J. Tao, Y.-C. Yeo, Y. Li, J.-W. Lee, P. Chen, M.-S. Liang, C. Hu, 5 nm-Gate nanowire FinFET. *IEEE Symposium VLSI Technology*, pp. 196-197 (2004)
- [9] D. Sacchetto, M.H. Ben-Jamaa, G. De Micheli, Y. Leblebici, Fabrication and characterization of vertically stacked gate-all-around Si nanowire FET arrays. *IEEE Proceedings European Solid State Device Research Conference ESSDERC*, pp. 245-248 (2009)
- [10] C. Pan, Z. Luo, C. Xu, J. Luo, R. Liang, G. Zhu, W. Wu, W. Guo, X. Yan, J. Xu, Z.L. Wang, J. Zhu, Wafer-scale high-throughput ordered arrays of Si and coaxial Si/Si_{1-x}Ge_x wires: fabrication, characterization, and photovoltaic application. *ACS Nano* 5(8), 6629-6636 (2011)

- [11] J. Nakamura, K. Higuchi, K. Maenaka, Vertical Si nanowire with ultra-high-aspect-ratio by combined top-down processing technique. *Microsyst. Tech.* 19, 433-438 (2013)
- [12] J. Goldberger, A.I. Hochbaum, R. Fan, P. Yang, Silicon vertically integrated nanowire field effect transistors. *Nano Lett.* 6, 973-977 (2006)
- [13] R.G. Hobbs, N. Petkov, J.D. Holmes, Semiconductor nanowire fabrication by bottom-up and top-down paradigms. *Chem. Mater.* 24, 1975-1991 (2012)
- [14] M.C.P. Wang, B.D. Gates, Directed assembly of nanowires. *Mater. Today* 12, 34-43 (2009)
- [15] E.M. Freer, O. Grachev, X. Duan, S. Martin, D.P. Stumbo, High-yield self-limiting single- nanowire assembly with dielectrophoresis. *Nat. Nanotechnol.* 5, 525-530 (2010)
- [16] S. Raychaudhuri, S.A. Dayeh, D. Wang, E.T. Yu, Precise semiconductor nanowire placement through dielectrophoresis. *Nano Lett.* 9, 2260-2266 (2009)
- [17] Y. Huang, X. Duan, Q. Wei, C.M. Lieber. Directed assembly of one-dimensional nanostructures into functional networks. *Science* 291, 630-633 (2001)
- [18] Z. Fan, J.C. Ho, Z.A. Jacobson, R. Yerushalmi, R.L. Alley, H. Razavi, A. Javey, Wafer-scale assembly of highly ordered semiconductor nanowire arrays by contact printing. *Nano Lett.* 8, 20-25 (2008)
- [19] S. Pregl, W.M. Weber, D. Nozaki, J. Kunstmann, L. Baraban, J. Opitz, T. Mikolajick, G. Cuniberti, Parallel arrays of Schottky barrier nanowire field effect transistors: nanoscopic effects for macroscopic current output. *Nano Res.* 6, 381-388 (2013)
- [20] D. Whang, S. Jin, Y. Wu, C.M. Lieber, *Nano Lett.* 3, 1255-1259 (2003)
- [21] S. Acharya, A.B. Panda, N. Belman, S. Efrima, Y. Golan, A semiconductor-nanowire assembly of ultrahigh junction density by the Langmuir-Blodgett technique. *Adv. Mater.* 18, 210-213 (2006)
- [22] O. Moutanabbir, D. Isheim, H. Blumtritt, S. Senz, E. Pippel, D.N. Seidman, Colossal injection of catalyst atoms into silicon nanowires. *Nature* 496, 78-82 (2013)
- [23] H. Park, R. Beresford, R. Ha, H.-J. Choi, H. Shin, J. Xu, Evaluation of metal-nanowire electrical contacts by measuring contact end resistance. *Nanotech.* 23, 245201 (2012)
- [24] Y. Cui, Z. Zhong, D. Wang, W.U. Wang, C.M. Lieber, High performance silicon nanowire field effect transistors. *Nano Lett.* 3, 149-152 (2003)
- [25] W.M. Weber, L. Geelhaar, E. Unger, C. ChÅ"ze, F. Kreupl, H. Riechert, P. Lugli, Silicon to nickel-silicide axial nanowire heterostructures for high performance electronics. *Phys. Status Solidi (b)* 244, 4170-4175 (2006)
- [26] A.I. Kingon, J.-P. Maria, S.K. Streiffer, Alternative dielectrics to silicon dioxide for memory and logic devices. *Nature* 406, 1032-1038 (2000)

- [27] A. Heinzig, S. Slesazek, F. Kreupl, T. Mikolajick, W.M. Weber, *Nano Lett.* 12, 119-124 (2012)
- [28] S.T. Chandra, N.B. Balamurugan, Performance analysis of silicon nanowire transistors considering effective oxide thickness of high-k gate dielectric. *J. Semicond.* 35, 044001-1 (2014)
- [29] Y.M. Niquet, A. Lherbier, N.H. Quang, M.V. Fernández-Serra, X. Blase, C. Delerue, Electronic structure of semiconductor nanowires. *Phys. Rev. B* 73, 165319 (2006)
- [30] D.D.D. Ma, C.S. Lee, F.C.K. Au, S.Y. Tong, S.T. Lee, Small-diameter silicon nanowire surfaces. *Science* 299, 1874-1877 (2003)
- [31] K.J. Kuhn, Considerations for ultimate CMOS scaling. *IEEE Trans. Electron Devices* 59, 1813-1828 (2012)
- [32] J. Knoch, M.T. Bjork, H. Riel, H. Schmidt, W. Riess, One-dimensional nanoelectronic devices-towards the quantum capacitance limit. *IEEE Proceedings Device Research Conference*, pp. 173-176 (2008)
- [33] T. Mikolajick, H. Ryssel, Influence of statistical dopant fluctuations on MOS transistors with deep submicron channel lengths. *Microelectron. Eng.* 21, 419-422 (1993)
- [34] T. Mikolajick, V. Haublein, H. Ryssel, The effect of random dopant fluctuations on the minimum channel length of short-channel MOS transistors. *Appl. Phys. A* 64, 555-560 (1997)
- [35] M. Diarra, Y.-M. Niquet, C. Delerue, G. Allan, Ionization energy of donor and acceptor impurities in semiconductor nanowires; importance of dielectric confinement. *Phys. Rev. B* 75, 045301 (2007)
- [36] M.T. Bjork, H. Schmid, J. Knoch, H. Riel, W. Riess, Donor deactivation in silicon nanostructures. *Nat. Nanotech.* 4, 103-107 (2009)
- [37] S.M. Koo, M.D. Edelstein, Q. Li, C.A. Richter, E.M. Vogel, Silicon nanowires as enhancement mode Schottky barrier field effect transistors. *Nanotech.* 16, 1482-1485 (2005)
- [38] J. Knoch, J. Appenzeller, Impact of the channel thickness on the performance of Schottky barrier metal-oxide-semiconductor field-effect transistors. *Appl. Phys. Lett.* 81, 3082 (2002)
- [39] J.-P. Colinge, C.-W. Lee, A. Afzalian, N.D. Akhavan, R. Yan, I. Ferain, P. Razavi, B. O'Neil, A. Blake, M. White, A.-M. Kelleher, B. McCarthy, R. Murphy, Nanowire transistors without junctions. *Nat. Nanotechnol.* 5, 225-229 (2010)
- [40] W. Tang, S.A. Dayeh, S.T. Picraux, J.Y. Huang, K.-N. Tu, Ultrashort channel silicon nanowire transistors with nickel silicide source/drain contacts. *Nano Lett.* 12, 3979-3985 (2012)
- [41] A.M. Ionescu, H. Riel, Tunnel field-effect transistors as energy-efficient electronic switches. *Nature* 479, 329-337 (2011)

- [42] L. Knoll, M. Schmidt, Q.T. Zhao, S. Trellenkamp, A. Schafer, K.K. Bourdelle, S. Mantl, Si tunneling transistors with high on-currents and slopes of 50 mV/dec using segregation doped NiSi₂ tunnel junctions. *Solid-State Electron.* 84, 211-215 (2013)
- [43] L. Knoll, Q.-T. Zhao, A. Nichau, S. Trellenkamp, S. Richter, A. Schafer, D. Esseni, L. Selmi, K.K. Bourdelle, S. Mantl, Inverters with strained Si nanowire complementary tunnel field- effect transistors. *IEEE Electron Device Lett.* 34, 813-815 (2013)
- [44] B. Ghosh, M.W. Akram, Junctionless tunnel field effect transistor. *IEEE Electron Device Lett.* 34, 584-586 (2013)
- [45] M. De Marchi, D. Sacchetto, S. Frache, J. Zhang, P.-E. Gaillardon, Y. Leblebici, G. De Micheli, Polarity control in double-gate, gate-all-around vertically stacked silicon nanowire FETs. *IEEE International Electron Devices Meeting (IEDM)*, pp. 8-4 (2012)
- [46] F. Wessely, T. Krauss, U. Schwalke, CMOS without doping: multi-gate silicon-nanowire field-effect-transistors. *Solid State Electron.* 70, 33-38 (2012)
- [47] M. De Marchi, D. Sacchetto, J. Zhang, S. Frache, P.-E. Gaillardon, Y. Leblebici, G. De Micheli, Top-down fabrication of gate-all-around vertically-stacked silicon nanowire FETs with controllable polarity. *IEEE Trans. Nanotech.* 13, 1029-1038 (2014)
- [48] J. Trommer, A. Heinzig, S. Slesazek, T. Mikolajick, W.M. Weber, Elementary Aspects for circuit implementation of reconfigurable nanowire transistors. *IEEE Electron Device Lett.* 35, 141-143 (2014)
- [49] A. Heinzig, T. Mikolajick, J. Trommer, D. Grimm, W.M. Weber, Dually active silicon nanowire transistors and circuits with equal electron and hole transport. *Nano Lett.* 13, 4176- 4181 (2013)
- [50] L. Tsakalakos, J. Balch, J. Fronheiser, B.A. Korevaar, O. Sulima, J. Rand, Silicon nanowire solar cells. *Appl. Phys. Lett.* 91, 233117 (2007)
- [51] M.D. Kelzenberg, D.B. Turner-Evans, B.M. Kayes, M.A. Filler, M.C. Putnam, N.S. Lewis, H.A. Atwater, Photovoltaic measurements in single-nanowire silicon solar cells. *Nano Lett.* 8, 710-714 (2008)
- [52] B.Z. Tian, T.J. Kempa, C.M. Lieber, Single nanowire photovoltaics. *Chem. Soc. Rev.* 38, 16-24 (2009)
- [53] X. Hua, Y. Zeng, W. Wang, W. Shen, Light absorption mechanism of c-Si/a-Si Half-coaxial nanowire arrays for nanostructured heterojunction photovoltaics. *IEEE Trans. Electron Devices* 61, 4007-4013 (2014)
- [54] T.J. Kempa et al., Semiconductor nanowires: a platform for exploring limits and concepts for nano-enabled solar cells. *Energy Environ. Sci.* 6, 719-733 (2013)
- [55] Y.-J. Lee, Y.-C. Yao, C.-H. Yang, Direct electrical contact of slanted ITO film on axial p-n junction silicon nanowire solar cells. *Opt. Express* 21, A7-A14 (2012)

- [56] W. Gobel, J. Hesse, J.N. Zerne (eds.), Sensors, a Comprehensive Survey, vol. 1. Fundamentals (VCH-Verlag, Weinheim, 1989)
- [57] J.I.A. Rashid, J. Abdullah, N.A. Yusof, R. Hajian, The development of silicon nanowire as sensing material and its applications. *J. Nanomater.* 3, 1-16 (2013)
- [58] P. Bergveld, Development of an ion-sensitive solid-state device for neurophysiological measurements. *IEEE Trans. Biomed. Eng.* 17, 70 (1970)
- [59] Y. Cui, Q. Wei, H. Park, C.M. Lieber, Nanowire nanosensors for highly sensitive and selective detection of biological and chemical species. *Science* 293, 1289-1292 (2001)
- [60] F. Patolsky, G. Zheng, O. Hayden, M. Lakadamyali, X. Zhuang, C.M. Lieber, Electrical detection of single viruses. *Proc. Natl. Acad. Sci. USA* 101, 14017-14022 (2004)
- [61] Q. Qing, Z. Jiang, L. Xu, R. Gao, L. Mai, C.M. Lieber, Free-standing kinked nanowire transistor probes for targeted intracellular recording in three dimensions. *Nat. Nanotech.* 9, 142-147 (2014)
- [62] Rurali, R., and N. Lorente, 2005a, *Phys. Rev. Lett.* 94, 026805
- [63] Ismail-Beigi, S., and T. Arias, 1998, *Phys. Rev. B* 57, 11923.
- [64] Singh, A., V. Kumar, R. Note, and Y. Kawazoe, 2005, *Nano Lett.* 5, 2302.
- [65] Zhao, X., C. M. Wei, L. Yang, and M. Y. Chou, 2004, *Phys. Rev. Lett.* 92, 236805.
- [66] Canham, L. T., 1990, *Appl. Phys. Lett.* 57, 1046.
- [67] Lehmann, V., and U. Gosele, 1991, *Appl. Phys. Lett.* 58, 856.
- [68] Buda, F., J. Kohanoff, and M. Parrinello, 1992, *Phys. Rev. Lett.* 69, 1272.
- [69] J.P. Colinge, *FinFETs and other Multi-Gate Transistors*. New York: Springer, 2007.
- [70] M. De Marchi et al., "Top-Down Fabrication of Gate-All-Around Vertically Stacked Silicon Nanowire FETs With Controllable Polarity," in *IEEE Transactions on Nanotechnology*, vol. 13, no. 6, pp. 1029-1038, Nov. 2014.
- [71] P.-E. Gaillardon, H. Ghasemzadeh, G. De Micheli, "Vertically-Stacked Silicon Nanowire Transistors with Controllable Polarity: A Robustness Study," *14th IEEE Latin American Test Workshop (LATW), Cordoba, Argentina*, 2013.
- [72] D. Sacchetto, S. Xie, V. Savu, M. Zervas and G. De Micheli et al., "Vertically-stacked gate-all-around polysilicon nanowire FETs with sub-micrometer gates patterned by nanostencil lithography," *Microelectronics Engineering*, vol. 98, pp. 355-358, 2012.
- [73] I. O'Connor and et al., "CNTFET modeling and reconfigurable logic-circuit design," *IEEE Trans. on CAS*, vol. 54, pp. 2365-2379, 2007
- [74] M.H. Ben Jamaa, K. Mohanram and G. De Micheli, "Novel library of logic gates with ambipolar CNTFETs: Opportunities for multi-level logic synthesis," *DATE Tech. Dig.*, 2009

- [75] S. Frache, D. Chiabrando, M. Graziano, M. Vacca, L. Boarino and M. Zamboni, "Enabling Design and Simulation of Massive Parallel Nanoarchitectures," *Journal of Parallel and Distributed Computing*, Elsevier, in press.
- [76] S. Frache, M. Graziano and M. Zamboni, "A Flexible Simulation Methodology and Tool for Nanoarray-based Architectures," *Proc. of IEEE International Conference on Computer Design*, Amsterdam, October 2010.
- [77] W. Lu, et al., Semiconductor nanowires, *J. Phys. D: Appl. Phys.* 39 (2006) 387-406
- [78] K.L. Wang, et al., "More than Moore's law: nanofabrics and architectures," in: *Bipolar/BiCMOS Circuits and Technology Meeting*, Sept. 30 2007-Oct. 2 2007, in: *BCTM '07, IEEE*, 2007, pp. 139-143.
- [79] I. Ercan, N.G. Anderson, "Tight-binding implementation of the microcanonical approach to transport in nanoscale conductors: generalization and analysis," *J. Appl. Phys.* 107 (2010) 124318.
- [80] Y. Luo, et al., "Two-dimensional molecular electronics circuits", *Chem. Phys. Chem.* 3 (6) pp. 519-525.
- [81] Y. Huang, et al., "Logic gates and computation from assembled nanowire building blocks", *Science* 294 (2001) 1313-1317.
- [82] Z. Huang, N. Geyer, P. Werner, J. de Boer and U. Gosele, "Metal-assisted chemical etching of silicon: a review", *Adv. Mater.*, vol.23, pp.285-308, Jan. 2011
- [83] J.Chen, P. Dong, D. Di, C. Wang, J. Wang and X. Wu, "Controllable fabrication of 2D colloidal-crystal films with polystyrene nanospheres of various diameters by spin-coating", *Appl. Surf. Sci.*, vol. 270, pp. 6-15, Apr. 2013
- [84] L. Boarino, E. Enrico, N. De Leo, F. Celegato, P. Tiberto, K. Sparnacci and M.Laus, "Macro and quasi-mesoporous silicon by self-assembling and metal-assisted etching," *Phys. Status Solidi*, vol.2008, pp.1403-1406, June 2011.
- [85] X. Li and P. Bohn, "Metal-assisted chemical etching in $\text{HF}/\text{H}_2\text{O}_2$ produces porous silicon", *Appl. Phys. Lett.*, vol.77, n.16, pp. 2572-2574, 2000
- [86] Y. Harada and X. Li, "Catalytic amplification of the soft lithographic patterning of Si. Nonelectrochemical orthogonal fabrication of photoluminescent porous Si pixel arrays", *J. Am. Chem. Soc.*, no.11, pp.8709-8717, 2001.
- [87] C. Chartier, S. Bastide and C. Levi-Clement, "Metal-assisted chemical etching of silicon in $\text{HF} - \text{H}_2\text{O}_2$ ", *Electrochim. Acta*, vol.53, pp.5509-5516, Jul. 2008.
- [88] Gregory X. Zhang, "Modern Aspects of Electrochemistry", Number 39, edited by C. Vayenas et Springer, New York, 2005.
- [89] R. de Picciotto, H. L. Stormer, L. N. Pfeiffer, K. W. Baldwin, and K. W. West. "Four-terminal resistance of a ballistic quantum wire.", *Nature*, 411:51-54, 2001.
- [90] R. Landauer, "Mesoscopic noise: Common sense view". *Physica B*, 227:156-160, 1996.

- [91] B. J. Van Wees, H. Van Houten, C. W. J. Beenakker, J. G. Williamson, L. P. Kouwenhoven, D. Van der Marel, and C. T. Foxen. "Quantized conductance of point contacts in a two-dimensional electron gas." *Phys. Rev. Lett.*, 60:848-850, 1988.
- [92] D. A. Wharam, T. J. Thornton, R. Newbury, M. Pepper, H. Ahmed, J. E. F. Frost, D. G. Hasko, D. C. Peacock, D. A. Ritchie, and G. A. C. Jones, "One-dimensional transport and the quantisation of the ballistic resistance", *J. Phys. C: Solid State Phys.*, 21:L209-L214, 1988.
- [93] M. A. Nielsen and I. L. Chuang. *Quantum Computation and Quantum Information*. Cambridge University Press, 2000.
- [94] V. B. Braginsky, F. Ya Khalili, and K. S. Thorne. *Quantum Measurement*. Cambridge University Press, 1995.
- [95] M. J. Buckingham. *Noise in Electronic Devices and Systems*. John Wiley and Sons, 1983.
- [96] Ya. M. Blanter and M. Buttiker. "Shot noise in mesoscopic conductors". *Phys. Rep.*, 336:1-166, 2000.
- [97] L. S. Levitov and G. B. Lesovik. "Charge distribution in quantum shot noise". *JETP Lett.*, 58:230-235, 1993.
- [98] L. S. Levitov, H. Lee, and G. B. Lesovik. "Electron counting statistics and coherent states of electric current." *J. Math. Phys.*, 37:4845-4866, 1996.
- [99] Yu. V. Nazarov and D. A. Bagrets. "Circuit theory for full counting statistics in multiterminal circuits.", *Phys. Rev. Lett.*, 88:196801, 2002.
- [100] M. Kindermann and Y. V. Nazarov. *Full Counting Statistics in Electric Circuits*, chapter In: *Quantum Noise in Mesoscopic Physics*, page 403. Kluwer, 2002.
- [101] C.A. Moritz, et al., "Latching on the wire and pipelining in nanoscale designs," in: *3rd Non-Silicon Comput. Workshop (NSC-3)*, Munich, Germany, 2004.
- [102] P. Narayanan, et al., "Manufacturing pathway and associated challenges for nanoscale computational systems," in: *9th IEEE Nanotechnology conference, NANO 2009*, July 2009.
- [103] P. Narayanan, J. Kina, P. Panchapakeshan, P. Vijayakumar, S. Kyeong-Sik, M. Rahman, M. Leuchtenburg, I. Koren, C. Chi On, C.A. Moritz, "Nanoscale application specific integrated circuits," in: *2011 IEEE/ACM International Symposium on Nanoscale Architectures, NANOARCH*, 8-9 June 2011, pp. 99-106.
- [104] P. Narayanan, et al., "Image Processing Architecture for Semiconductor Nanowire Fabrics," in: *IEEE Nanotechnology conference, NANO 2008*.
- [105] P. Narayanan, et al., "Comparison of Analog and Digital Nano-Systems: Issues for the Nano-Architect," in: *IEEE International Nanoelectronics Conference, INEC*, 2008.
- [106] J. Sallese, F. Krummenacher, F. Prégaldiny, C. Lallement, A. Roy and C. Enz, "A design oriented charge-based current model for symmetric DG MOSFET and

- its correlation with the EKV formalism," *Solid-State Electron.*, vol. 49, no. 3, pp. 485-489, Mar. 2005.
- [107] B. Diagne, F. Prégaldiny, C. Lallement, J. Sallese and F. Krummenacher, "Explicit compact model for symmetric double-gate MOSFETs including solutions for small-geometry effects," *Solid-State Electron.*, vol. 52, no. 1, pp. 99-106, Jan. 2008.
- [108] F. Lime, B. Iñiguez and O. Moldovan, "A quasi-two-dimensional compact drain-current model for undoped symmetric double-gate MOSFETs including short-channel effects," *IEEE Trans. Electron Devices*, vol. 55, no. 6, pp. 1441-1448, Jun. 2008.
- [109] D. Munteanu, J. Autran, X. Loussier, S. Harrison, R. Cerutti and T. Skotnicki, "Quantum Short-Channel Compact Modelling of Drain-Current in Double-Gate MOSFET," *Solid-State Electron.*, vol. 50, no. 4, pp. 680-686, Apr. 2006.
- [110] O. Moldovan, A. Cerdeira, D. Jiménez, J. P. Raskin, V. Kilchytska, D. Flandre, N. Collaert and B. Iñiguez, "Compact model for highly-doped double-gate SOI MOSFETs targeting baseband analog applications," *Solid-State Electron.*, vol. 51, no. 5, pp. 655-661, May. 2007.
- [111] P. , G. Hu, R. Liu and T. Tang, "Electric potential and threshold voltage models for double-gate Schottky-barrier source-drain MOSFETs," *Microelectronics Journal*, vol. 42, no. 10, pp. 1164-1168, Oct. 2011.
- [112] W. Wang, H. Lu, J. Song, S. Lo and Y. Taur, "Compact modeling of quantum effects in symmetric double-gate MOSFETs," *Microelectronics Journal*, vol. 41, no. 10, pp. 688-692, Oct. 2010.
- [113] B. Iñiguez, A. Lázaro, H. Abd-Elhamid, O. Moldovan, B. Nae, J. Roig and D. Jiménez, "Charge-Based Compact Modeling of Multiple-Gate MOSFETs," *Custom Integrated Circ. Conf (CICC)*, 2007, pp. 49-56.
- [114] B. Iñiguez, T. A. Fjeldly, A. Lázaro, F. Danneville and M. J. Deen, "Compact-Modeling Solutions for Nanoscale Double-Gate and Gate-All-Around MOSFETs," *IEEE Trans. Electron Devices*, vol. 53, no. 9, pp. 2128-2142, Sept. 2006.
- [115] I. O'Connor et al., *IEEE Trans. on Circuits and Systems I*, vol. 54, no. 11, pp. 2365-2379, 2007.
- [116] M. De Marchi, D. Sacchetto, S. Frache, J. Zhang, P.-E. Gaillardon, Y. Leblebici and G. De Micheli, "Polarity Control in Double-Gate, Gate-All-Around Vertically Stacked Silicon Nanowire FETs", *IEDM*, Dec. 2012.
- [117] A. DeHon, "Array-based architecture for FET-based nanoscale electronics," *IEEE Transactions on Nanotechnology*, vol. 92, n. 1, pp. 23-32, Mar. 2003.
- [118] C.A. Moritz, T. Wang, P. Narayanan, M. Leuchtenburg, Y Guo, C. Dezan and M. Bennaser, "Fault-Tolerant Nanoscale Processors on Semiconductor Nanowire Grids," *IEEE Trans. on Circuits and Systems I*, vol. 54, no. 11, pp. 2422-2437, Nov. 2007.

- [119] M. Tang, F. Prégaldiny, C. Lallement and J. Sallese, "Explicit Compact Model for Ultranarrow Body FinFETs," *IEEE Trans. Electron Devices*, vol. 56, no. 7, pp. 1543-1547, Jul. 2009.
- [120] G.D. Smit, A. J. Scholten, G. Curatola, R. van Langevelde, G. Gildenblat and D.B.M. Klaassen, "PSP-based scalable compact FinFET model," *Proc. Nanotech*, 2007, pp. 520-525.
- [121] S.H. Oh, D. Monroe and J.M. Hergenrother, "Analytic Description of Short-Channel Effects in Fully-Depleted Double-Gate and Cylindrical, Surrounding-Gate MOSFETs," *IEEE Electron Device Lett.*, vol. 21, no. 9, pp. 445-447, Sep. 2000.
- [122] S.H. Lin, X. Zhou, G.H. See et al., "A rigorous surface-potential-based I-V model for undoped cylindrical nanowire MOSFETs," *Proc. 7th IEEE Conf. on Nanotechnol.*, 2007, pp. 889-892.
- [123] B. Cousin, M. Reyboz, O. Rozeau, M.A. Jaud, T. Ernst and J. Jomaah, "A unified short-channel compact model for cylindrical surrounding-gate MOSFET," *Solid-State Electron.*, vol. 56, no. 1, pp. 40-46, Feb. 2011.
- [124] N. Chevillon, M. Tang, F. Pregaldiny et al., "FinFET Compact Modeling and Parameter Extraction," *16th IEEE International Conference Mixed Design of Integrated Circuits and Systems (MIXDES'2009)*, Jun 2009, LODZ, Poland. Proc. pp. 55-60
- [125] M. Tang, F. Pregaldiny, C. Lallement and J.M. Sallese, "Quantum compact model for ultra-narrow body FinFET," *10th International Conference on Ultimate Integration of Silicon, ULIS*, 2009, Mar 2009, pp. 293 - 296
- [126] MATLAB, The MathWorks, Inc., Natick, Massachusetts, United States.
- [127] Silvaco Int, ATLAS User's Manual A 2D-3D Numerical Device Simulator - <http://www.silvaco.com>.
- [128] R. Behrish, "Sputtering by Particle Bombardment", *Top. Appl. Phys.*, vol.110, chapt. 4, p.145, 1981
- [129] H.Adachi, *Handbook of Sputtering Technology*, Elsevier, 2012.
- [130] K. Wasa, *Handbook of Sputter Deposition Technology: Fundamentals and Applications for Functional Thin Films, Nano-materials and MEMS*. William Andrew, Incorporated, 2012.
- [131] K. Balasundaram, J.S.Sadhu, J.C.Shin, B.Azeredo, D. Chanda et al., "Porosity Control in metal-assisted chemical etching of degenerately doped silicon nanowires.", *Nanotechnology*, vol.23, p. 304-305, Aug. 2012.
- [132] Iannaccone, G., G. Curatola, and G. Fiori. "Effective Bohm Quantum Potential for device simulation based on drift-diffusion and energy transport." *SISPAD* 2004.
- [133] Meirav, U. and Foxman, E. B. *Semiconductor Science and Technology* 11(3), 255 (1996)

- [134] Tiwari, S., Rana, F., Chan, K., Shi, L., and Hanafi, H. Applied Physics Letters 69(9), 1232-1234 (1996)
- [135] Datta S., Electronic transport in mesoscopic systems, Cambridge University Press, 1995.
- [136] Hohenberg, P., and W. Kohn, 1964, Phys. Rev. 136, B864.
- [137] Lockwood, D. J. Semiconductor and Semimetals, Light Emission in Silicon From Physics to Devices. Academic Press, San Diego. (1998)
- [138] Anping Cao, Ernst J.R. Sudho and Louis C.P.M. de Smet, "Silicon Nanowire-Based Devices for Gas-Phase Sensing", Sensors 2014, 14, 245-271
- [139] A. Liu, "Towards development of chemosensors and biosensors with metal-oxide-based nanowires or nanotubes", Biosens. Bioelectron. 2008, 24, 167-177
- [140] K. J. Thomas, J. T. Nicholls, M. Y. Simmons, M. Pepper, D. R. Mace, and D. A. Ritchie, Phys. Rev. Lett. 77, 135 (1996)
- [141] Haug, R., Hong, J., and Lee, K. Surface Science 263(13), 415 -418 (1992).
- [142] van der Vaart, N. C., Godijn, S. F., Nazarov, Y. V., Harmans, C. J. P. M., Mooij, J. E., Molenkamp, L. W., and Foxon, C. T. Phys. Rev. Lett. 74, 4702-4705 Jun (1995).
- [143] Waugh, F. R., Berry, M. J., Mar, D. J., Westervelt, R. M., Campman, K. L., and Gossard, A. C. Phys. Rev. Lett. 75, 705-708 Jul (1995)
- [144] Tiwari, S., Rana, F., Hanafi, H., Hartstein, A., Crabb, E. F., and Chan, K. Applied Physics Letters 68(10), 1377-1379 (1996).
- [145] Choi, B. H., Hwang, S. W., Kim, I. G., Shin, H. C., Kim, Y., and Kim, E. K. Applied Physics Letters 73(21), 3129-3131 (1998).
- [146] A. Antidormi, D. Chiabrando, M. Graziano, L. Boarino, G. Piccinini, "Methodology modeling of MaE-fabricated Porous Silicon Nanowires", Microelectronics and Electronics (PRIME), 2014 10th Conference on Ph.D. Research in, Grenoble, June 30 2014-July 3 2014 . pp. 1-4
- [147] L Boarino, C Baratto, F Geobaldo, G Amato, E Comini, AM Rossi, G Faglia, "NO₂ monitoring at room temperature by a porous silicon gas sensor", Materials Science and Engineering: B 69, 210-214
- [148] Rurali, R., A. Poissier, and N. Lorente, 2006, Phys. Rev. B 74(16), 165324.
- [149] A. Antidormi, M.G. Graziano; L. Boarino, G. Piccinini, "Analysis of the Effects of surface interaction on Silicon Nanowires conduction". In: IEEE Nano, Rome, July 2015. pp. 1-3
- [150] Barner, J. B. and Ruggiero, S. T. Phys. Rev. Lett. 59, 807-810 Aug (1987)
- [151] Weis, J., Haug, R. J., Klitzing, K. v., and Ploog, K. Phys. Rev. Lett. 71, 4019-4022 Dec (1993)
- [152] Wang, S. D., Sun, Z. Z., Cue, N., Xu, H. Q., and Wang, X. R. Phys. Rev. B 65, 125307 Mar (2002)
- [153] van der Wiel, W. G., Franceschi, S. D., Fujisawa, T., Elzerman, J. M., Tarucha, S., and Kouwen- hoven, L. P. Science 289(5487), 2105-2108 (2000)

- [154] Yeyati, A. L., Martin-Rodero, A., and Flores, F. Phys. Rev. Lett. 71, 2991-2994 Nov (1993)
- [155] Meir, Y. and Wingreen, N. S. Phys. Rev. Lett. 68, 2512-2515 Apr (1992)
- [156] Gurvitz, S. A. Phys. Rev. B 57, 6602-6611 Mar (1998)
- [157] Illera, S., Prades, J. D., Cirera, A., and Cornet, A. EPL (Europhysics Letters) 98(1), 17003 (2012)
- [158] S. Illera, J.D. Prades, A. Cirera, A. Cornet, "A Transfer Hamiltonian model for devices based in quantum dot arrays", Journal of Computational Physics, <http://arxiv.org/abs/1207.5513> ISSN: 0021-9991
- [159] P.A. Mello, N. Kumar, "Quantum Transport in Mesoscopic Systems", Oxford University Press, 2004
- [160] N. Higham, "Computing the Polar Decomposition-with Applications", SIAM J. Sci. and Stat. Comput., 7(4), 1160-1174
- [161] Y. Cui and C. M. Lieber, Science 291, 851, 2001.
- [162] Chung, S.-W., J.-Y. Yu, and J. R. Heath, 2000, Appl. Phys. Lett. 76(15), 2068.
- [163] S. Frache, M. Graziano, M. Zamboni , "A Flexible Simulation Methodology and Tool for Nanoarray-based Architectures", IEEE International Conference on Computer Design, Amsterdam, 3-6 October. pp. 60-67.
- [164] M. Graziano, S. Frache, M. Zamboni, "An Hardware Viewpoint on Biosequence Analysis: What's Next?", ACM JOURNAL ON EMERGING TECHNOLOGIES IN COMPUTING SYSTEMS, vol. 9 n. 4, pp. 1-21.
- [165] Goldberger, J., A. I. Hochbaum, R. Fan, and P. Yang, 2006, Nano Lett. 6(5), 973.
- [166] Y. Cui, Q. Wei, H. Park, and C. M. Lieber, Science 293,1289, 2001.
- [167] S. Sharma, M. Madou, "A new approach to gas sensing with nanotechnology", Phil. Trans. R. Soc. A 2012, 370, 2448-2473.
- [168] R.M. Penner, "Chemical sensing with nanowires" , Annu. Rev. Anal. Chem. 2012, 5, 461-485.
- [169] L.C.P.M. De Smet, D. Ullien, M. Mescher, E.J.R. Sudhölter, "Organic Surface Modification of Silicon Nanowire-Based Sensor Devices", In Nanowires-Implementations and Applications; Hashim, A., Ed.; InTech: Rijeka, Croatia, 2011; pp. 267-288.
- [170] M. S. Gudiksen, L. J. Lauhon, J. Wang, D. C. Smith, and C. M. Lieber, 2002, Nature 415(6872), 617.
- [171] P. J. Pauzauskie, and P. Yang, 2006, Mat. Tod. 9(10), 36.
- [172] M. Mescher, , L.C.P.M. de Smet, E.J.R. Sudholter, J.H. Klootwijk, "Robust fabrication method for silicon nanowire field effect transistors for sensing applications", J. Nanosci. Nanotechnol. 2013, 13, 5649-5653
- [173] T.S.Y. Moh, G. Pandraud, L.C.P.M. de Smet, C.J.M. van Rijn, E.J.R. Sudhölter, P.M. Sarro, "Fabrication of Nanowires for Biosensing Applications",

- In Nanodevices and Nanofabrication-Selected Publications from Symposium of Nanodevices and Nanofabrication in ICMAT2011; Zhang, Q., Milne, W.I., Eds.; Pan Stanford Publishing Pte. Ltd.: Singapore, 2012; pp. 1-40.
- [174] A. Tricoli, M. Righettoni, A. Teleki, "Semiconductor gas sensors: Dry synthesis and application" *Angew. Chem. Int. Ed.* 2010, 49, 7632-7659.
 - [175] E. Stern, J.F. Klemic, D.A. Routenberg, P.N. Wyrembak, D.B. Turner-Evans, A.D. Hamilton, D.A. LaVan et al. "Label-free immunodetection with CMOS-compatible semiconducting nanowires", *Nature* 2007, 445, 519-522.
 - [176] L Boarino, C Baratto, F Geobaldo, G Amato, E Comini, AM Rossi, G Faglia, "NO₂ monitoring at room temperature by a porous silicon gas sensor", *Materials Science and Engineering: B* 69, 210-214
 - [177] A. Antidormi, D. Chiabrando, M. Graziano, L. Boarino, G. Piccinini, "Methodology modeling of MaE-fabricated Porous Silicon Nanowires", *Microelectronics and Electronics (PRIME)*, 2014 10th Conference on Ph.D. Research in, Grenoble, June 30 2014-July 3 2014 . pp. 1-4
 - [178] Rurali, R., A. Poissier, and N. Lorente, 2006, *Phys. Rev. B* 74(16), 165324.
 - [179] Björk, M. T., H. Schmid, J. Knoch, H. Riel, and W. Riess, 2009, *Nature Nanotech.* 4(2), 103.
 - [180] M. Ng, L. Zhou, S. Yang, L.Y. Sim, V. Tan and P. Wu, *Phys. Rev. B* 76, 155435, Oct. 2007.
 - [181] Leu, P. W., B. Shan, and K. Cho, 2006, *Phys. Rev. B* 73(19), 195320.
 - [182] T. Markussen, R. Rurali et al., "Scaling Theory Put into Practice: First-Principles Modeling of Transport in Doped Silicon Nanowires", *Phys. Rev. Lett.* 99, 076803, Aug. 2007.
 - [183] Durgun, E., N. Akman, C. Ataca, and S. Ciraci, 2007a, *Phys. Rev. B* 76(24), 245323.
 - [184] Y. Zheng, C. Rivas, R. Lake, K. Alam et al., "Electronic properties of silicon nanowires", *IEEE Trans. Electron Dev.*, vol.52, n.6, Jun. 2005
 - [185] Atomistix ToolKit version 11.2, QuantumWise A/S (www.quantumwise.com)
 - [186] P. Hohenberg and W. Kohn, "Inhomogeneous Electron Gas", *Phys. Rev.* 136, B864, 1964
 - [187] R.O. Jones and O. Gunnarsson, "The density functional formalism, its applications and prospects", *Rev. Mod. Phys.* 61 , 689, 1989
 - [188] X. Chen, C.K.Y. Wong, C.A. Yuan, G. Zhang, "Nanowire-based gas sensors", *Sens. Actuators B: Chem.* 2013, 177, 178-195.
 - [189] F. Patolsky, C.M. Lieber, "Nanowire nanosensors", *Mater. Today* 2005, 8, 20-28.
 - [190] K. Peng, X. Wang, S. Lee, "Gas sensing properties of single crystalline porous silicon nanowires". *Appl. Phys. Lett.* 2009, 95, 243112.
 - [191] F. Patolsky, G. Zheng, C.M. Lieber, "Nanowire-based biosensors", *Anal. Chem.* 2006, 78, 4260-4269.

- [192] M.Y. Bashouti, K. Sardashti, S.W. Schmitt, M. Pietsch, J. Ristein et al., "Oxide-free hybrid silicon nanowires: From fundamentals to applied nanotechnology". *Prog. Surf. Sci.* 2013, 88, 39-60.
- [193] E. Stern, A. Vacic, M.A. Reed, "Semiconducting nanowire field-effect transistor", *IEEE Trans. Electron. Devices* 2008, 55, 3119-3130.
- [194] Soler, J. M.; Artacho, E.; Gale, J. D.; Garcia, A.; Junquera, J.; Ordejon, P.; Sanchez-Portal, D. *J. Phys.: Condens. Matter* 2002, 14, 2745-2779.
- [195] Anglada, E. M.; Soler, J.; Junquera, J.; Artacho, E. *Phys. Rev. B* 2002, 66, 205101.
- [196] Perdew, J. P.; Burke, K.; Ernzerhof, M. *Phys. Rev. Lett.* 1996, 77, 3865-3868.
- [197] Monkhorst, H. J.; Pack, J. D. *Phys. Rev. B* 1976, 13, 5188-5192